FACULTY
OF MATHEMATICS
AND PHYSICS
Charles University

DOCTORAL THESIS

Diana Naydenkova

Study of plasma in tokamak-type devices with spectroscopic methods

Department of Surface and Plasma Science

Supervisor of the doctoral thesis: RNDr. Jan Stöckel, CSc.

Study programme: Physics
Study branch: F2, Physics of Plasmas and Ionized Media

Prague 2017

I declare that I carried out this doctoral thesis independently, and only with the cited sources, literature and other professional sources.

I understand that my work relates to the rights and obligations under the Act No. 121/2000 Coll., the Copyright Act, as amended, in particular the fact that the Charles University has the right to conclude a license agreement on the use of this work as a school work pursuant to Section 60 paragraph 1 of the Copyright Act.

In…..... date..... signature

I would like to thank to my supervisor, RNDr. Jan Stöckel, CSc. for proposing this subject and for many helpful suggestions. My thanks also to my advisor,
Mgr. Vladimír Weinzettl, PhD for guiding and supporting me over the years. I would also like to thank to all COMPASS tokamak team for patient cooperation in experiments. I would like to thank and dedicate this thesis to my grandparents and to my aunt for giving possibility to get high education. I would like to thank to my faculty for perfect basic received knowledge.

Title: Study of plasma in tokamak-type devices with spectroscopic methods

Author: Diana Naydenkova

Department / Institute: Department of surface and plasma science

Supervisor of the doctoral thesis: RNDr. Jan Stöckel, CSc., Tokamak Department, Institute of Plasma Physics of the Czech Academy of Science

Abstract: In Tokamak department of Institute of Plasma Physics, radiation of high-temperature plasma is investigated using spectroscopic methods in visible, ultraviolet and infrared regions. The radiation gives information regarding tokamak plasma parameters and their changes, which is necessary for future realization of fusion reactor. In the frame of this doctoral thesis the development of spectroscopic diagnostics for observing of plasma radiation and its temporal evolution in COMPASS tokamak was performed. The absolute calibration of developed systems in order to recalculate measured signal to units of radiation was done. The sources of imprecisions of absolute measurements in tokamak conditions are properly discussed in the first part of the dissertation. Plasma radiation in the range 257-1083 nm was measured and interpreted using NIST database and FLYCHK code. Ion density for the most significant impurities was estimated. IDL code for effective ion charge estimation as a ratio of real and hydrogen plasma Bremsstrahlung radiation near 523 nm was developed. Profiles of electron density and temperature measured by Thomson scattering system were used for hydrogen plasma Bremsstrahlung radiation calculations. The example of applying of spectroscopic data for studying of COMPASS plasma heating using neutral beam injections is given in the last part of this work.

Keywords: COMPASS, spectroscopy, calibration, Zeff, NBI

Contents

Introduction

Demand for energy is expected to increase three times till the end of 21st century under the combined pressure of population growth, increased urbanization and expanding access to electricity in developing countries. A new source of energy is urgently needed.

Fusion is a reaction between two or more atomic nuclei which come close enough to form one or more different atomic nuclei. Fusion is potentially attractive way of energy generation because of several advantages. Typical fusion reaction releases nearly four million times more energy than a typical chemical reaction during burning of coal, oil or gas and four times more than fission reaction (at equal mass). Fusion fuels are widely available and nearly inexhaustible. Nuclear fusion reactors produce no high activity, long-lived nuclear waste. A nuclear accident is not possible in a fusion device. If any disturbance occurs, the plasma cools within seconds and the reaction stops. The quantity of fuel present in the vessel at any one time is enough for a few seconds only and there is no risk of a chain reaction. The power output of fusion reactor will be similar to that of a fission reactor. The average cost per kilowatt of electricity is also expected to be similar. Fusion could make a positive contribution to the reducing of CO_2 level.

One of the devices where fusion reaction can be reached is tokamak. Experimental research of tokamak systems started in 1956 in Kurchatov Institute, Moscow by a group of Soviet scientists led by Lev Artsimovich. The group constructed the first doughnut-shaped magnetic confinement device called a tokamak, the most successful being T-3 and its larger version T-4. T-4 was tested in 1968 in Novosibirsk, conducting the first ever quasistationary thermonuclear fusion reaction. From this time the tokamaks became the dominant concept in fusion research, and tokamak devices multiplied across the wold.

The amount of fusion energy which a tokamak is capable to produce correlates directly to the number of fusion reactions taking place in its core. It means in order to get more energy we need bigger plasma. The world record for fusion power is held by the tokamak Joint European Torus (JET). In 1997, JET produced 16 MW of fusion power from a total input power of 24 MW. It means return of energy defined by so called fusion energy gain factor Q was 0.67. Ten times larger device – ITER (International Thermonuclear Experimental Reactor) tokamak is

under construction now. ITER is designed to produce a ten-fold return of energy (Q=10), or 500 MW of fusion power from 50 MW of input power, for long pulses (400-600 s). ITER will not capture the energy it produces as electricity and will be used to study plasmas under conditions similar to those expected in a future power plant and test technologies such as heating, control, diagnostics, cryogenics and remote maintenance in an integrated way.

The main goal of existing tokamaks research programs is steered towards basic challenges of physics and technology linked to the construction and operation of the international experimental reactor ITER and future fusion reactors.

The COMPASS (COMPact ASSembly) tokamak is the smallest tokamak which has ITER-like plasma shape. The principal parameters of COMPASS tokamak are shown in table 1. Volume of its plasmas correspond to one tenth (in the linear scale) of the ITER plasmas. The flexible neutral beam heating system and ability to achieve H-mode allow COMPASS to contribute to ITER-relevant plasma physics studies. High flexibility in tokamak operation and low-cost of experiments make it especially attractive in fusion program. Nowadays, besides COMPASS there are only two tokamaks in Europe with ITER-like configuration which are able to get the High plasma confinement. They are JET and ASDEX-U (Axially Symmetric Divertor Experiment - Upgrade).

Parameters	Values
Major radius R	0.56 m
Minor radius a	0.23 m
Plasma current I_p (max)	400 kA
Magnetic field B_T	0.9 - 2.1 T
Vacuum pressure	$1x10^{-6}$ Pa
Elongation	1.8
Plasma shape	D, SND, elliptical, circular
Pulse length	~ 1 s
Beam heating P_{NBI} 40 keV	2 x 0.4 MW

Table 1. The main parameters of COMPASS tokamak.

The COMPASS tokamak has been designed and operated in 90th in UKAEA (United Kingdom Atomic Energy Authority) in Culham. The COMPASS operation in Great Britain was finished in 2002 due to the start of the MAST (Mega Ampere Spherical Tokamak) tokamak operation. Due to its direct relevance to the ITER project - the facility was offered by the European Commission and UKAEA to the Institute of Plasma Physics of the Czech Academy of Sciences (IPP AV CR v.v.i.) in

Prague in autumn 2004. IPP accepted the offer in July 2005. The COMPASS tokamak arrived to Prague in October 2007. First plasma in the COMPASS tokamak was received in our institute in September 2008. The COMPASS started its official operation in IPP AV CR v.v.i. in Prague in February 2009.

At this moment, COMPASS experiments focus on the physics of the plasma edge and scrape-off layer, plasma-wall interaction, and the physics of disruptions and instabilities. The spectroscopic diagnostics belong to the key diagnostics for these investigations. Therefore, in the frame of COMPASS tokamak operation program the spectroscopic measurements are focused on studying of the behaviour of visible radiation of excited neutral atoms and ions from the plasma periphery, namely hydrogen or the most intensive impurity lines. Also, an Magnetohydrodynamics (MHD) [1] activity can be investigated using such observations. Finally, information on neutral atoms density, impurity inflow, recycling processes [2] and rough estimation of particle confinement can be derived from the spectroscopic measurements.

In the frame of COMPASS tokamak reinstallation and this dissertation work four new optical diagnostics for visible plasma radiation studying were developed. They are:

- set of slow (temporal resolution from 5 ms to total discharge duration) spectroscopic systems with high spectral resolution (0.15 nm, 0.17 nm, 0.04 nm and 0.23 nm) for plasma radiation measurements in the rage 247-1084 nm,
- set of optical systems for fast (temporal resolution 0.5 μs) spectrally resolved measurements of the most intensive spectral lines,
- visible part of multichannel optical system for fast (1 μs) plasma radiation measurements with high spatial resolution (~1 cm),
- high resolved (0.004 nm) spectroscopic system with temporal resolution ~10 ms for plasma rotation measurements. The system allows impurities temperature estimation.

Brief description of all mentioned systems and performed work, which was done by me in the frame of developing of each of them, is given in the first part of the next chapter. The rest of dissertation work is devoted to discussion of development and results received using first two of mentioned systems.

In the first part of this thesis we discuss:

1. the development of spectroscopic systems for COMPASS tokamak
2. the absolute calibration of developed systems
3. the sources of calibration imprecisions
4. the phenomena influencing the precision of measured spectroscopic values.

Some results obtained using developed spectroscopic diagnostic are discussed in the second part of the dissertation. They are:

1. typical measured spectrum and its interpretation
2. effective ion charge estimation and detailed discussion of its precision
3. influence of tokamak plasma heating to spectroscopic values.

1. Development and absolute calibration of the spectroscopic system for COMPASS tokamak

1.1. The initial state

In the end of 2007 tokamak COMPASS was moved from Culham Science Centre to its new location in the Institute of Plasma Physics in Prague (See figure 1.1.1). Besides tokamak itself some of systems used for the COMPASS operation in Culham laboratory were transported to Prague. They are vacuum and gas puffing systems, magnetic diagnostic, microwave interferometer and neutral particle analyser. No optical systems and devices were provided from Culham.

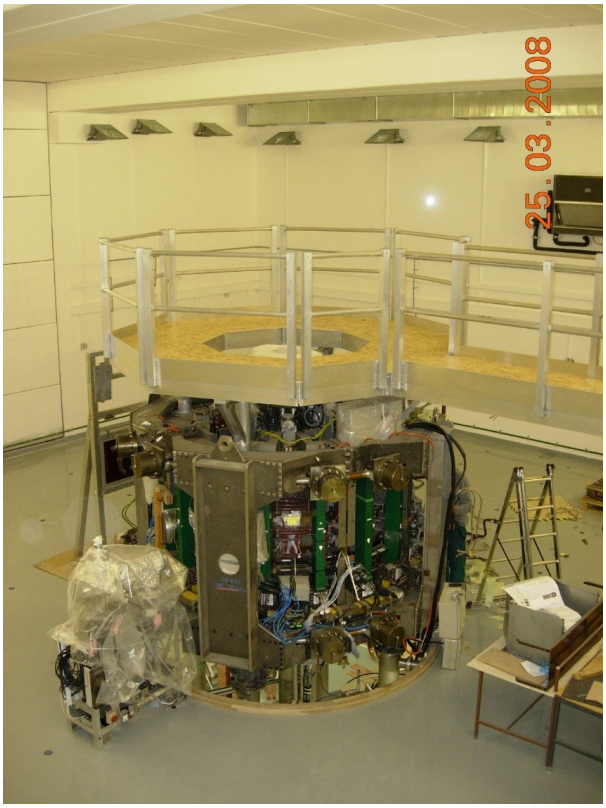

Figure 1.1.1 The COMPASS tokamak after its reinstallation in IPP AV CR v.v.i.

In the frame of COMPASS tokamak reinstallation, a set of new optical diagnostics for tokamak plasma studying was developed. Among them are a Thomson scattering system, two fast cameras, multichannel tomographic system, few different spectrometers and PMT based systems (see figure 1.1.2).

In the frame of my work I was supposed to develop spectroscopic diagnostics and a part of tomographic system used for visible plasma radiation measurement.

Few ports in different cross-sections were planned to be used for spectroscopic measurements at tokamak COMPASS. The ports had to fulfil few requirements. Firstly, position of ports should allow using of shutter. Then they should be easily reachable in order to allow installation of optics.

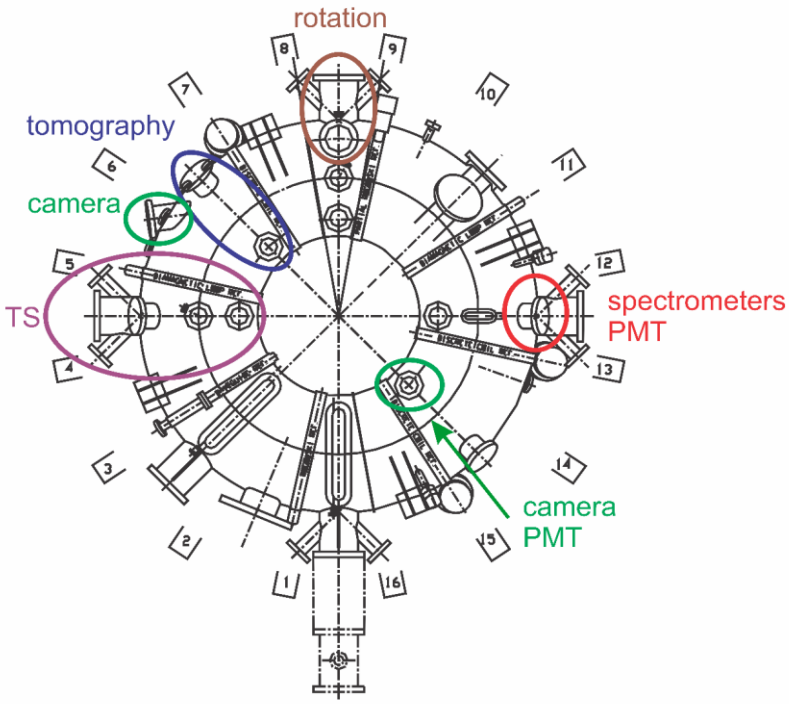

Figure 1.1.2. Schema of optical systems position at COMPASS tokamak.

The upper-angular port at 12/13 tokamak cross-section was decided to be used for spectroscopic measurement allowing simple exchange between diagnostics. The port is used for set of new fast photomultiplier based systems and few new slow but wide-range minispectrometers [3]. Only four channels are available. The development of these systems and results achieved using them are properly described and discussed in this dissertation work.

High resolution two-grating spectrometer based system for plasma rotation measurements was chosen to be spaced in COMPASS tokamak section 8/9 allowing measurements of plasma radiation at SQL from top and from the bottom at the same cross-section and along the same chord. The system measures Doppler shifts of CIII spectral lines next to 465 nm. The system can also measure CIII Doppler broadening of mentioned spectral lines allowing CIII ions temperature estimation. This system plans to use new optics for collimation of plasma radiation and spectrometers which have originally been developed and operated in the ISTTOK tokamak. The plasma

rotation system design was changed few times already. The first design and first results received by me were described in [4]. Mgr. Matěj Tomeš took over this system since year 2013.

The new tomographic system for visible plasma radiation measurement consisting of two parts was chosen to be installed at the poloidal section 6/7 of the COMPASS tokamak. The system is inserted to the same diagnostic ports with fast spectroscopic detectors such as fast AXUV-based bolometers and semiconductor SXR detectors with regard to the presence of the two NBI heating systems in the vacuum vessel and a possibility to realize tomographic reconstructions of the selected radiation ranges. Nowadays the tomographic system is monitoring the integral plasma radiation in a visible spectral range both from the plasma core and from the plasma edge. It allows monitoring of MHD activity of plasma, estimation of recycling processes and particle confinement time. Development of multichannel diagnostic was discussed in few works [5], [6], [7]. Notwithstanding that the development of the system was already finished and first measurements were successfully done, the software allowing estimation of mentioned plasma parameters still should be created in future.

1.2. Diagnostic design

Optical systems in tokamaks can be split into two parts: the tokamak side part and detector side part. They are connected by an optical fibre (see fig. 1.2.1).

On the COMPASS, the first element of the tokamak side is the quartz vacuum window, which represents an interface between the tokamak vessel and the diagnostic system and allows measurements from NUV (near ultraviolet) to NIR (near infrared), covering whole operational range of photomultipliers (PMTs) (important for an easy use of this light channel for other purposes). Depending on the aim of experiment there can be used the lens, which is located inside the diagnostic port just behind the window and collects plasma radiation to optical fibre or simply fibre alone without the lens can be used. 20 m long optical fibre transfers the light to the detection part of the system located in the diagnostic room in order to reduce an influence of X-rays and neutron radiation coming from the tokamak. UV-VIS high OH (fused silica core ∅200 μm and cladding with thickness ~20 μm) or VIS-NIR low OH (fused silica core ∅200 μm and cladding with thickness ~20 μm) were chosen as an optical fibre material for the system. The numerical aperture (NA) of

the fibres is 0.22. Such a value of NA allows compensating of attenuation of measured radiation with the distance from radiation source to the optical fibre input (inverse-square law). We decided to use SMA (SubMiniature version A) fibre connectors [8] ensuring a co-centric connection and an easily repeatable reconnection.

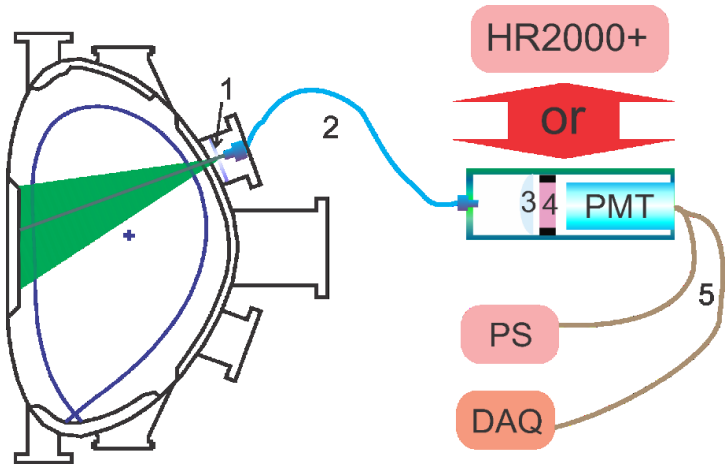

Figure 1.2.1. Scheme of visible diagnostic system. 1 – vacuum window, 2 - optical cable, 3 - collecting lens, 4 – interference filter, 5 – electrical cables, PMT – photomultiplier, DAQ – data acquisition system, PS – power supply, HR2000+ – minispectrometer.

The detector part can be represented by PMT based system or minispectrometer.

A cylindrical tube allowing perfect alignment of all optical components of the detector side part consists of the SMA connector for optical fibre equipment, of the collecting lens spaced at focal distance from the fibre and of the interference filter. The collecting lens from Thorlabs is made from the BK7 glass, has diameter of 50 mm and focal distance around 50 mm. It was chosen for the tube because, from one side, the price of such a lens is 5 times smaller than quartz one and, from other side, the transmittance (around 92%) of such a lens is comparable with quartz one at wavelengths of interest. The interference filter from Andover Corporation, Thorlabs or TOPTEC Centre (department of IPP) with transmittance in the range of interest is located behind the lens. The detector is PMT from HAMAMATSU company of the type R5929 or R374 powered by the high voltage power supply C9525. For us the most important detector parameters are spectral response range, quantum efficiency of the detector at the wavelength of interest, time response, gain and level of dark current. The spectral response range for R5929 is 300-900 nm and for R374 it is

185-850 nm. The quantum efficiency of R374 is higher below 500 nm than R5929 and lower above. Therefore, R374 is used for the measurements below 500 nm and R5929 above. The time response is 15 ns for both detectors. The dark current is 3 nA for R374 and 5 nA for R5929. Data collection system ATCA [9] is used for data collection in the range ±10 V with the temporal resolution of 2 MHz (0.5 μs). The ATCA noise is around 5 mV. Therefore, the time response and noise level of total PMT based system is limited by ATCA temporal resolution and noise.

The lens (located in front of PMT) converts a divergent beam of plasma radiation going from optical fibre to an approximately parallel beam propagating through the interference filter, and further to PMT. Thereby the detection part reaches maximal efficiency. It has axisymmetric alignment and parallel settings of components relatively to optical axis. It allows minimizing effects connected with aberrations.

The spectroscopic diagnostic on the COMPASS tokamak has been composed of four minispectrometers of the HR2000+ type from Ocean Optics. Each of them can be easily mounted to our system instead of one of cylindrical tubes with PMT discussed above. The most of parameters of the devices are pre-set by producer [10], but customer can choose some of them. The most important chosen parameters are spectral resolution and operational range. The resolution was chosen for the visible (460-663 nm), near UV (247-473 nm) red (630-680 nm) and IR (659-1084 nm) spectral ranges, as 0.15 nm, 0.17 nm, 0.04 nm and 0.23 nm, respectively [11], [12]. Only minispectrometer with operational range 630-680 nm allows estimation of ions and atoms temperature in our plasma conditions. Temporal resolution of all used spectrometers depends on the aim of experiments and can be set from 4 ms to 65 s. The signal-to-noise ratio is 250:1. The f-number is f/4. The sensitivity is in the range of 41-75 photons/count depending on the wavelength. The spectrometers use the linear silicon CCD (Charge-coupled device) array Sony ILX511 as a detector. In result the set of our spectrometers covers region roughly from 250 nm (so called near UV) to 1085 nm (the limit of silicon detectors sensitivity approximately).

1.3. Absolute calibration

Absolute sensitivity calibration of any optical system allows to convert units of measurement to units of radiation. The calibration constant for given optical system has meaning of reciprocal value of spectral transmittance combined with

photosensitivity of the spectroscopic system. Therefore, absolute sensitivity calibration is supposed to be done for completion of the spectroscopic system. The sources of temporally stabilized known radiation are used during such a calibration.

There are primary and secondary radiation standards suitable for such a calibration. Blackbody radiators belong to primary standards. The spectral radiance of blackbody is determined by Planck's law and it is a function of temperature and wavelength only. The precision of temperature control determines the uncertainty of the spectral radiance. Fixed points of the International Temperature Scale like melting temperature of gold and platinum are mostly used reference standards.

The absolute sensitivity calibration by means of a synchrotron source is a quite typical method of absolute sensitivity spectroscopic calibration in tokamaks. The calibration for the range of wavelengths out of radiation of a synchrotron source can be done using branching ratios of observed transitions from the same upper level to different lower levels. The absolute value of one of the lines should be determined during the calibration using a synchrotron source. This method was used at JET [13]. The main disadvantage of such a method is that plasma should emit suitable pairs of lines or suitable impurities can be added, moreover absolute value of intensity of one of the lines must be known and lines must be observed in sufficiently broad range of wavelengths. The method gives calibration constant for exact wavelength. The main advantage is possibility of in situ calibration. The accuracy of the calibration is strongly determined by the accuracy of the transition probabilities values.

Calibration lamps belong to secondary radiation standards. Using of calibration lamps of known radiation, for absolute sensitivity calibration of spectroscopic systems at tokamaks is not typical but quite attractive alternative. Using this method, it is possible to get the values of calibration constants for the whole range of interest within a good precision and the results of calibration do not depend on radiation and composition of plasma. In situ calibration is not necessary in this case.

1.3.1 Method

Absolute calibration was done by means of the ORIEL absolutely calibrated source, which consists of the 45 W or 200 W calibrated lamp of known spectral irradiance [14]

$$I_{TAB}\left[\frac{\mu W}{cm^2 \cdot nm}\right] = \frac{1}{10}\left(\lambda^{-5} \cdot e^{A+\frac{B}{\lambda}} \cdot \left(C + \frac{D}{\lambda} + \frac{E}{\lambda^2} + \frac{F}{\lambda^3} + \frac{G}{\lambda^4} + \frac{H}{\lambda^5}\right)\right)$$

where I_{TAB} is tabulated spectral irradiance emitted by the calibration source at wavelength λ through the area of S_{TAB} = 1 cm^2 at r_{TAB} = 50 cm distance measured at lamp current 6.5 A and lamp voltage approx. 32 V. A, B, C, D, E, F, G and H parameters are taken from the calibration protocol and they are individual for each calibration lamp.

The absolute calibration was done as provided by NIST (National Institute of Standards and Technology) calibration standard and a radiometric power supply. These standards require no auxiliary optics to be used. The principal parameters published in the supplier manual are given below in this paragraph. Under normal use, the lamp is simply placed at a 50 cm distance from the input aperture of the optical system, on which the calibrated irradiance is projected. Accurate placement is important; since a source-aperture distance error of 2.5 mm results in a 1% error of calibration. Producer guarantees that inaccuracy of the data caused by the lamp stabilization is maximum 2%. Output of this lamp can also be slightly (up to 5%) polarized. Our calibrated 45 W or 200 W lamps are supposed to be used in the spectral range 250-2400 nm. Usage of a lamp, which produces too high or too low radiation, puts higher demands on the linearity of our detection system [15]. Since a calibrated lamp has only 50 hours guaranteed for a valid calibration and the calibration dramatically varies with a lamp usage, we use one more originally non-calibrated lamp for recalibration on the base of calibrated lamp for our calibration procedures. We check periodically a validity of our recalibration, because of evolution of lamp emission during its lifetime, by comparison with radiation of reference calibrated lamp.

The scheme for absolute calibration of the optical systems for visible plasma radiation measurements on COMPASS tokamak is presented at Figure 1.3.1.

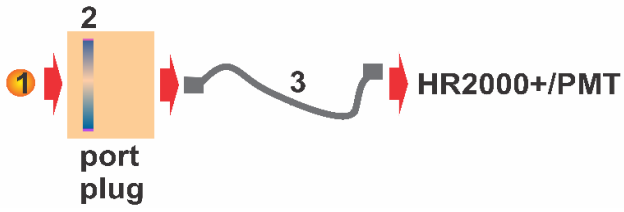

Figure 1.3.1 Scheme of absolute calibration. 1- calibration source, 2 – vacuum window, 3 - optical fibre, HR 2000+ - minispectrometer, PMT – photomultiplier based optical tube.

The calibration source described above was set as an input source for each of the described system at the conditions recommended for calibration by producer. Instead of the 1 cm^2 aperture, the well-defined detection surface of the total system was used for the calibration.

In the case of minispectrometers the calibration procedure allows to recalculate the number of counts N_{MEAS} registered by the spectroscopic system to the power of plasma radiation P_{MEAS_HR2000} in μW measured during the experiment as:

$$P_{MEAS\_HR2000}[\mu W] = PCF_{HR2000}\left[\frac{\mu W}{cnt}\right] \cdot N_{MEAS}[cnt]$$

where PCF_{HR2000} is power calibration factor in μW/cnt. The factor is derived from the laboratory measurements as follows:

$$PCF_{HR2000}\left[\frac{\mu W}{cnt}\right] = \frac{I_{TAB}\left[\frac{\mu W}{cm^2 \cdot nm}\right] \cdot \Delta\lambda[nm] \cdot S_{CAL}[cm^2]}{N_{CAL}[cnt]} \cdot \frac{r_{TAB}^2[cm]}{r_{CAL}^2[cm]} \cdot \frac{P_{CAL}[W]}{P_{TAB}[W]}$$

where Δλ is spectral width of one pixel of the spectrometer, S_{CAL} is the incident area during calibration (i.e. area of the lens or of the hole through the screen) at distance r_{CAL}, N_{CAL} is the measured number of counts in one (spectral) pixel during the calibration. The correction factor of P_{CAL} / P_{TAB} represents a correction of tabulated input power of the calibration source P_{TAB} to measured input power of the source reached during the calibration P_{CAL}.

In the case of PMT based systems the calibration procedure allows recalculating of the signal in volts V_{MEAS} registered by the PMT based system to the power of plasma radiation P_{MEAS_PMT} in μW measured during the experiment as:

$$P_{MEAS\_PMT}[\mu W] = PCF_{PMT}\left[\frac{\mu W}{V}\right] \cdot V_{MEAS}[V]$$

where PCF_{PMT} is power calibration factor in μW/V.

The calibration constant is derived from the laboratory measurements as follows:

$$PCF_{PMT}\left[\frac{\mu W}{V}\right] = \frac{I_{TAB}\left[\frac{\mu W}{cm^2 \cdot nm}\right] \cdot \Delta\lambda[nm] \cdot S_{CAL}[cm^2]}{V_{CAL}[V]} \cdot \frac{r_{TAB}^2[cm]}{r_{CAL}^2[cm]} \cdot \frac{P_{CAL}[W]}{P_{TAB}[W]}$$

where Δλ is operational wavelength range of PMT based system defined by transmittance range of the system or by QE of PMT, S_{CAL} is the incident area during calibration (i.e. area of the lens or of the hole through the screen) at distance r_{CAL},

V_{CAL} is signal measured in volts by oscilloscope Rigol and is corrected to difference between impedance of oscilloscope and regular detection system ATCA. The correction factor of P_{CAL} / P_{TAB} represents a correction of tabulated input power of the calibration source P_{TAB} to measured input power of the source reached during the calibration P_{CAL}.

The PMT gain depends on power supply input voltage. It allows to get good signal to noise ratio of measured signal in very wide range of radiation. Therefore, the calibration constant is measured for the whole operation range of the PMT.

Measured spectral irradiance (also called spectral intensity) SPI_{MEAS} (radiant flux density, i.e. power incident to unit area per unit spectral range) is given as

$$SPI_{MEAS}\left[\frac{\mu W}{cm^2 \cdot nm}\right] = \frac{P_{MEAS}[\mu W]}{\Delta\lambda[nm] \cdot S_{MEAS}[cm^2]}$$

where S_{MEAS} is the incident area during measurement (i.e. area of the lens or of the hole through the screen) and P_{MEAS} is the power of plasma radiation measured during the experiment.

Measured spectral radiance SPR_{MEAS} (power from unit source area emitted into unit solid angle per unit spectral range) is given as

$$SPR_{MEAS}\left[\frac{\mu W}{sr \cdot cm^2 \cdot nm}\right] = \frac{P_{MEAS}[\mu W]}{\frac{S_{MEAS}[cm^2]}{r^2_{MEAS}[cm]} \cdot \Delta\lambda[nm] \cdot S_{SOURCE}[cm^2]}$$

where S_{MEAS} is the incident area during measurement (i.e. area of the lens or of the hole through the screen) at the distance r_{MEAS}, and S_{SOURCE} is the source area (observed area on plasma as a radiation source).

1.3.2 Calibration results and their imprecisions

During calibration procedure one will deal with several constrains, which should be considered to get precise calibration. We will consider each of reasons which cause imprecision of our optical systems calibration constants using the results of our systems calibration. Some of them play significant roles for both minispectrometers and for PMT based systems; others are principal only for one of these systems. The calibration constant for spectrometers is wavelength dependent array. The calibration constant of PMT based system is measured as a function of input voltage of PMT. It is necessary for setting of the PMT based system depending on plasma radiation value.

1.3.2.1 Alignment

Alignment is main reason of error in calibration constant [16]. The axially symmetric optical elements can be used for plasma radiation collection in our case. The system is aligned, if the centre-of-curvature of each optical element is positioned on the optical axis. During our calibration it was used only simple optical equipment: no micrometric equipment and laser was used for placement of components of our calibration system. It was found out that precision of such a calibration for the systems, which include some optics at the entrance, is too low to be discussed. It was one of the reasons why no optics was used in some steps of our calibrations and measurements.

The set from more than one hundred of curves was measured during a few years of tokamak operation for the case of no optics used for calibration of HR2000+ spectrometer in operational range 629.66-680.59 nm. Some of them are presented in Figure 1.3.2.

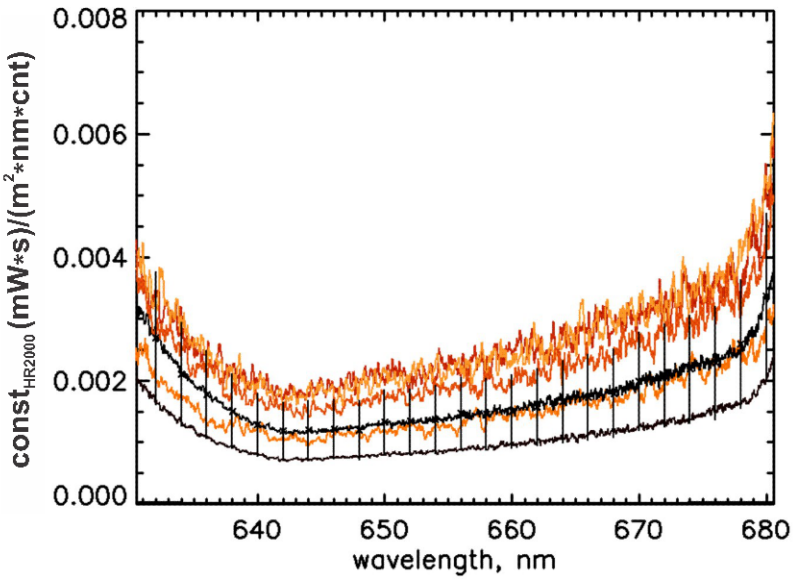

Figure 1.3.2. Spectral dependence of calibration constant of whole system based on minispectrometer HR2000+ within the operational range 629.66-680.59 nm. We present few calibration curves which were received in the repeated measurements using 45W (orange) and 200W (black) calibration lamps for the same conditions.

The results were received using two calibrating lamps 45 W (orange lines) and 200 W (black lines). The distance between the lamp and input to diagnostic system was roughly 50 cm. So as the calibration was done for the same system and in similar conditions, the scattering of the calibration curves at the figure 1.3.2 can be

explained only by precision of alignment between the calibration lamp and the system input. The calibration constant of spectroscopic system is reciprocal value of the product of system transmittance and quantum sensitivity. Therefore, the highest precision of alignment in the figure 1.3.2 has the measurement which is presented by the bottom curve and the lowest precision has the top one.

It is possible to see in figure 1.3.2 that alignment caused just shift of calibration curves relatively to each other for some constant values. It is useful to know the average value of scattering of these curves, because it is proportional to expected calibration imprecision caused by alignment. The set of more than one hundred measurements, which were done using two calibrating lamps 45 W and 200 W, allows us to estimate the value of average scattering of calibration curves caused by alignment imprecision. The value of average scattering can get up to ±30% in case of discussed system. This value is shown in figure 1.3.2 by black colour for one of measured curves. The scattering values were plotted with the gaps of 10 nm for figure clarity. Such a large calibration imprecision caused by alignment shows that both micrometric equipment and laser must be used for proper alignment during calibration; otherwise we can get significant systematic error.

It is possible to see quite good repeatability of the calibration curves which were measured with roughly one year interval for PMT based system for Bremsstrahlung radiation measurements given as a sample of such type of systems in the figure 1.3.3. The calibration precision in low input voltage range, where output voltage is low as well, depends on signal to noise ratio of detecting device used during calibration measurements. Therefore, the imprecision gets to 50% for low input voltage and decreases to less than 10% in linear part of voltage dependence. The measurements are provided in the linear range, so the calibration imprecision because of alignment is less than 10% for PMT based systems. It can be evidence of the fact that the designed PMT based system does not have so high requirements to alignment as minispectrometers and it is not already the main source of imprecision as for the case of minispectrometers.

1.3.2.2. Quantum noise

It is also possible to see in Figure 1.3.2 that calibration curves achieved from measurements using 45 W calibration lamp are noisier than those ones measured with 200 W source. It corresponds to a quantum noise and is proportional to square

root of number of detected counts. Because of it, the 200 W calibration lamp is used in the following calibrations. It is also possible to see that the calibration constant strongly changes at the edges of operational range, because of reduced transmittance of the spectrometer there. The noise level of the linear CCD array (detector of spectrometer) is given by thermal noise. During tests in lab temporal dependence of background noise was measured. Typical linear dependence of background noise on integration time was measured as was predicted in producer manual [15].

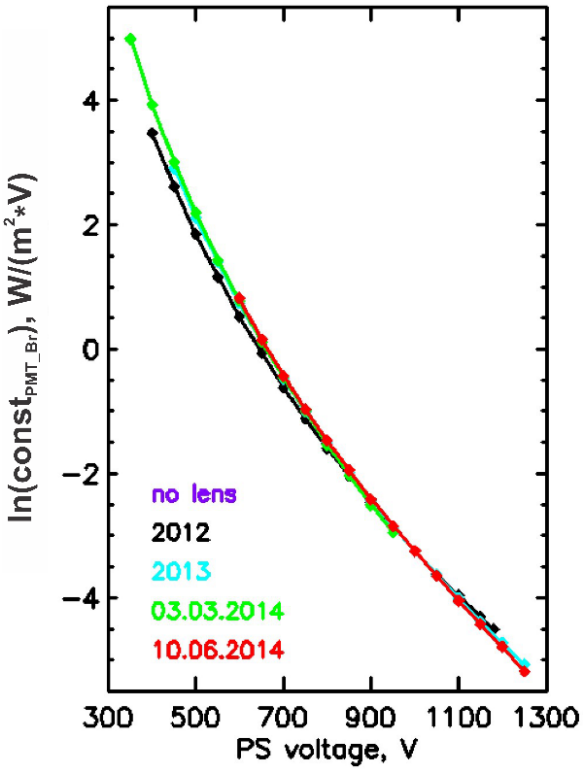

Figure 1.3.3. The logarithmic dependence of calibration constant for PMT based system for Bremsstrahlung radiation measurements on input voltage of PMT power supply.

1.3.2.3. Wavelength dependence of quantum sensitivity

The spectrometer we use has quite wide operational range. It leads to big difference in total system sensitivity for different wavelengths. It is possible to see a big noise at top curve measured by 45 W lamp (figure 1.3.4a) for wavelengths shorter than 480 nm, which is caused by low sensitivity of the spectrometer in this range. Measured data have rather low signal to noise ratio in this range, which causes big imprecision of calibration constant. This is possible to prevent by two ways: the first one is using a stronger source (200 W calibration lamp) allowing good signal to noise ratio even for low sensitivity and different exposition times for measurement of

calibration constant in different parts of the operational range of the spectrometer (figure 1.3.4b).

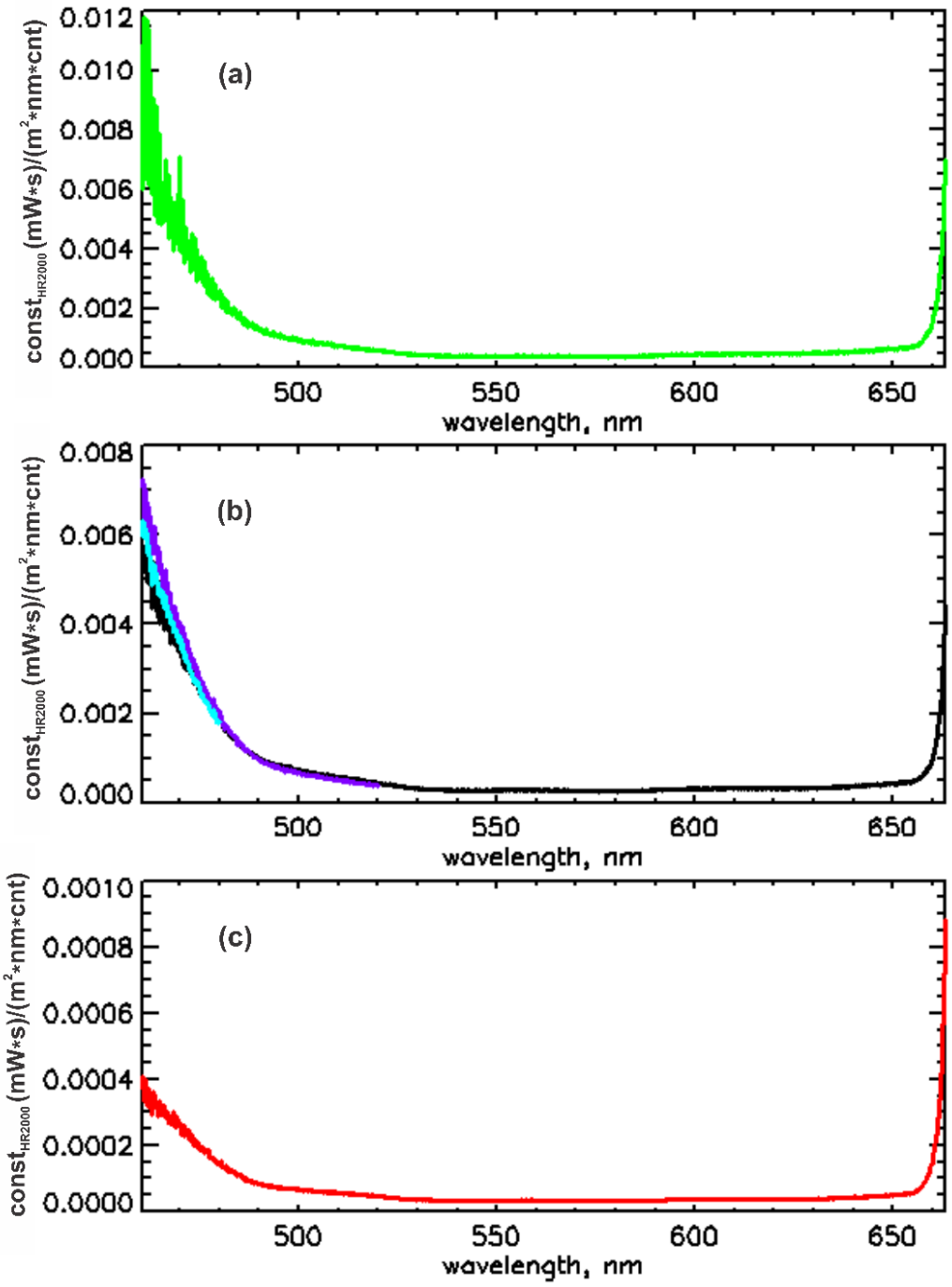

Figure 1.3.4. Demonstration of importance of choosing of calibration source and integration time for precise calibration. Spectral dependence of calibration constants of the whole system. Measurements were done using minispectrometer HR2000+ with operational range 457.83-663.18 nm (visible range). a) measured using 45 W lamp without lens, b) measured using 200 W lamp without collecting lens for several values of the integration time, 0.13 s (black), 0.3 s (violet) and 2 s (blue), c) measured using 45 W lamp using collecting lens.

Resulting calibration curve in this case consists from two parts: one was measured using a longer integration time; the second part was measured with a shorter integration time. The second way to increase signal to noise ratio is to use collecting lens, which increases amplitude of the signal by increasing of light collecting area (figure 1.3.4c). In this case it is crucial to have the fibre well aligned. It is quite difficult to realize this step in practice because of too small fibre diameter. It is also possible to increase measured radiation intensity by decreasing a distance between the source and entrance to the system, but this is objectionable, because it does not allow using the point light source approximation.

1.3.2.4. Wavelength dependence of calibration source irradiance

All calibration lamps have their own colour temperature representing different spectral distribution of their emission. More powerful lamps have typically higher equivalent spectral temperatures, i.e. near UV light more populated. It can become one of the reasons of calibration imprecision. The calibration results for the UV spectrometer are shown in figure 1.3.5.

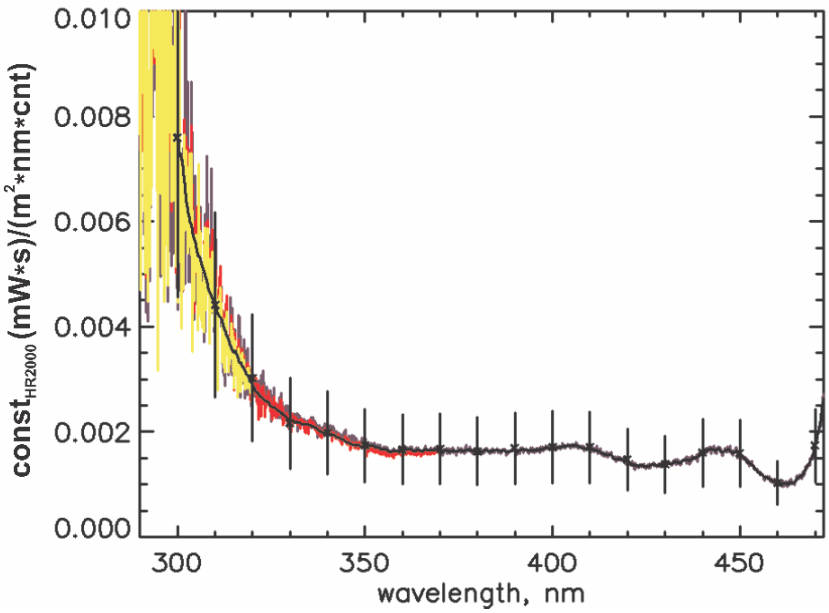

Figure 1.3.5. Spectral dependence of calibration constants of the system based on minispectrometer HR2000+ within the near UV operational range of 247.77-472.29 nm using different integration times: 1 s (violet), 7 s (red) and 40 s (yellow). Resulting calibration constant is black Smoothed curve consists from parts with different integration time in the optimised set up.

The curves were measured using 200 W lamp and different integration times. The 45 W calibration lamp was not efficient in this range at all. Mentioned imprecision in calibration constant starts from wavelengths less than 330 nm because of decreasing of both fibre and spectrometer transmittance; at the same time radiation of 200 W halogen lamp starts to fade rapidly. Increase of integration time does not give any improvement of signal to noise ratio for wavelengths less than 330 nm (see figure 1.3.5). It is not possible to make more precise calibration using the 200 W quartz halogen lamp source for wavelengths shorter than 330 nm. Other source, which is brighter in this range, must be used for less than 330 nm for more precise calibration.

1.3.2.5. Wavelength dependence of transmittance of the system components

One more constraint in our case can be given by improper fibre type choice. Fibres produced from different materials have spectral properties suitable for specified usage conditions, so the fibre marking is very important during producing procedure. Widely accepted way to do it is marking by decrease of optical transmittance of fibre in a narrow wavelength range [17]. Using the fibre in a spectral range of the high attenuation leads to higher detection threshold of spectral lines appearing in this ranges.

The results of absolute sensitivity calibration of the spectroscopic system using near IR minispectrometer for the cases of using both UV/VIS high OH and VIS/NIR low OH are shown in figure 1.3.6.

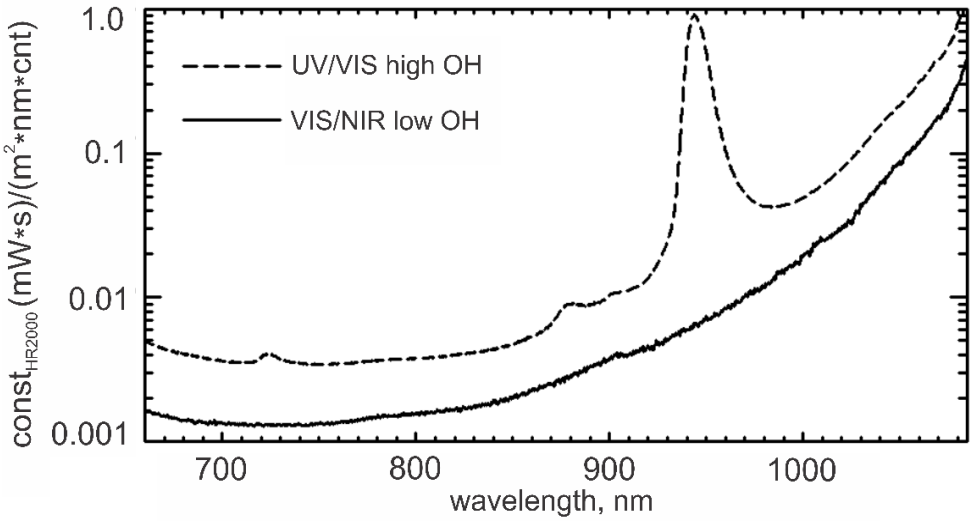

Figure 1.3.6. Absolute sensitivity calibration constant for spectroscopic system using near IR minispectrometer with UV/VIS high OH or VIS/NIR low OH optical fibres.

It is possible to see a strong drop of transmittance connected with UV/VIS high OH fibre marking in the 920-970 nm wavelength range. The strong decrease of sensitivity above 970 nm is connected with both the optical fibre transmittance decrease and with the silicon detector sensitivity decrease. Such behaviour makes the configuration with UV/VIS high OH fiber not suitable for measurements in wavelength range above 920 nm.

Comparison of calibration curves for UV/VIS high OH and VIS/NIR low OH optical fibres shows that sensitivity of two systems is similar for the wavelength range below 920 nm. On the other hand, sensitivity of VIS/NIR fibre is significantly higher above 920 nm. It means the VIS/NIR fibre is more suitable for measurements with this minispectrometer.

1.3.2.6. Finite width of interference filter transmittance range used for PMT based systems

The tokamak spectrum is generally not very rich. There are only few really intensive spectral lines but time to time they are spaced quite close to each other. The interference filters used for our PMT based systems are required to be as narrow as possible but it is not always enough to escape influence of neighbouring intensive spectral lines. The influence of these neighbouring parasitic spectral lines to results measured by PMT based system signal can be significant. Therefore, we should consider this source of imprecision separately for each used PMT based system. We discussed only PMT based system for CIII radiation measurements in this dissertation only because of dissertation volume limit. We will use plasma radiation measured by minispectrometers in the range of interest for our study.

It is typical for tokamaks to study temporal behaviour of sputtered first wall material. One of the most principal wall impurities for the case of our tokamak is carbon. The most intensive carbon spectral line is triplet of CIII spectral lines 464.742, 465.025 and 465.147 nm. For fast measurements of these lines we use the system described above on the base of R374 PMT from Hamamatsu using interference filter with transmittance range 462.5-469 nm produced by TOPTEC Centre (department of IPP).

Each optical component of any optical system has wavelength dependence of optical transmittance. All detectors have wavelength dependent quantum efficiency. Therefore, we will use in our discussion wavelength dependent quantum efficiency

(QE) of total system. This quantity is a product of optical transmittance of each used optical component and quantum efficiency of PMT. It can be presented in per cent. We show it in figure 1.3.7a by red curve. FWHM (Full width at half maximum) of PMT based system for CIII triplet measurements is around 2 nm. The QE is 2.8%, 4.18% and 4.56% for 464.742, 465.025 and 465.147 nm, respectively.

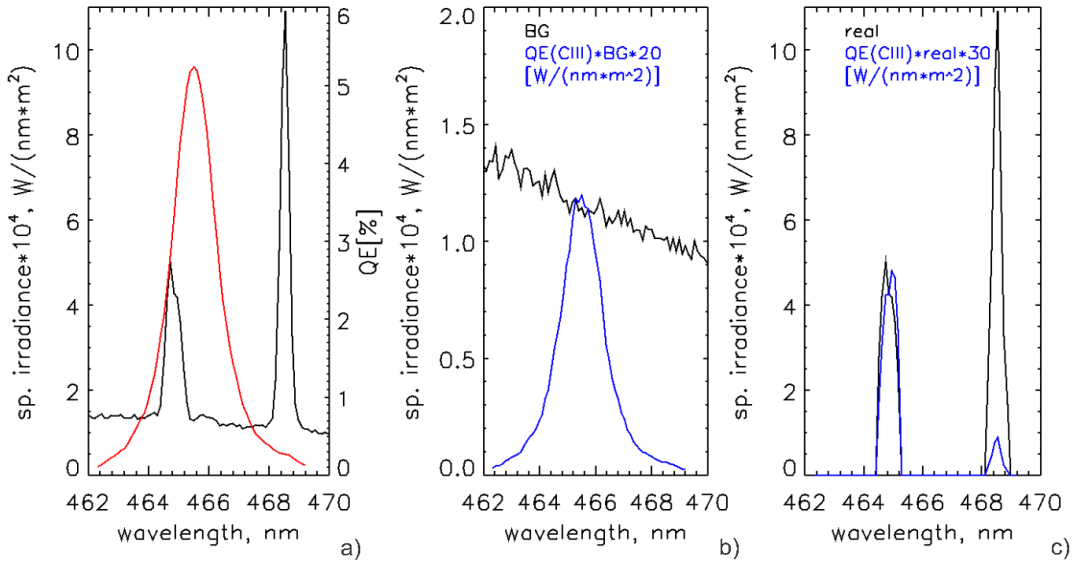

Figure 1.3.7. a) Plasma irradiance in the transmittance range of PMT based system measured using so called VIS spectrometer with temporal integration during the discharge #7202 (black) combined with quantum efficiency (QE) of total PMT based system for CIII triplet measurement (red curve). b) Background of the measured spectra in the range of interest (black) combined with product of QE and the background (blue). c) Plasma irradiance after the noise removing (black) and product of QE and spectral irradiance of plasma in the transmittance range of the PMT based system (blue).

Now we will compare QE of PMT based system for CIII triplet measurements and plasma irradiance measured in the range of interest temporally integrated during discharge #7202 duration at COMPASS tokamak (see figure 1.3.7a). It is possible to see two spectral lines and background given by thermal noise of CCD detector of the spectrometer used for the measurements. The spectral resolution of used spectrometer does not allow to distinguish spectral lines belonging to the CIII triplet and show them as one line next to 465 nm. Second spectral line 468.57 nm belongs to HeII. The QE of our system is 0.27% for this helium spectral line.

The spectral measurements at COMPASS tokamak have limit in irradiance of spectral line that can be measured by our devices in principle. This limit is caused by

two reasons. First one is limited sensitivity of minispectrometer detector (41-75 photons/count) and second one is limited duration of our discharges (300-400 ms). Therefore, the background at the measured spectrum given in figure 1.3.7b can be used as threshold of plasma radiation measurement for each pixel of spectrometer detector. All plasma radiation higher than this value is measured as a spectral line, all values lower than the background value cannot be measured by the spectrometer. It is possible to see that this value is roughly 0.0001-0.00015 W/(nm*m^2) for the spectrometer in the range of interest.

We measured two oxygen spectral lines (464.91 and 465.08 nm) in the operational range of discussed CIII diagnostic using the highly spectrally resolved spectroscopic system used for plasma rotation measurements [4]. These lines belong to transition $2s^22p^2(^3P)3p$ to $2s^22p^2(^3P)3s$. There are few more lines of the same transition in the operation range of PMT based system for CIII measurements: 463.88 nm, 464.18 nm, 466.16 nm, 466.59 nm, 467.37 nm, 467.62 nm and 469.63 nm. They have comparable irradiance according to NIST database; therefore, all of them will play some role in our signal.

The PMT is able to measure separate quantum of light. Therefore, we cannot exclude that it will measure some unexpected radiation immeasurable by the minispectrometer. Let us consider limit value of such probable radiation. We will suppose that the background measured by minispectrometer corresponds to parasitic light, which is present in the whole range of interest. The product of QE of this system and background (figure 1.3.7b blue curve) gives to us information about maximal influence of probable parasitic radiation hidden in background to our measured value. The maximal probable parasitic spectral irradiance will get to $5 \cdot 10^{-6}$ W/(nm*m^2) in the case of discussed system. The wavelength integration of the product of QE and background will lead to maximal total level of possible parasitic irradiance with value $1.27 \cdot 10^{-5}$ W/m^2. It means that precision of CIII content estimation is higher for discharges with higher CIII spectral line intensity (it means higher CIII content).

Now we can compare wavelength dependent plasma irradiance in the range of interest with removed background shown in figure 1.3.7c by black curve and multiplication of wavelength dependent plasma irradiance in the range of interest to QE of the system which represents contribution of each spectral line to resulting signal (figure 1.3.7c blue curve). The helium line is twice more intensive than carbon

in original spectrum. The contribution of HeII calculated on the base of figure 1.3.7c to measured spectrum during discussed discharge #7202 is around 12-13%. Therefore, the precision of CIII line measurements can be quite low in discharges with high He content. It is necessary to make spectral measurements for precise estimation of helium influence to value of CIII measured by PMT based system.

Let's consider temporal evolution of the discussed values to understand in which part of discharge the largest influence of parasitic helium line can be expected. We will discuss properly the result obtained using the PMT based system and minispectrometer for D-shape discharge #10956 as an example. Signals were measured using the neighbouring channels at the same diagnostic port; it allows almost the same plasma volume observation, so that CIII signals measured using two systems should be comparable.

It is possible to see from the minispectrometer measurements shown in Fig 1.3.8a that parasitic helium spectral line irradiance continuously increases during the discharge. This behaviour is typical for helium in all COMPASS tokamak discharges and was explained as influx of helium from the wall materials. It gets there during glow discharge before the working discharge. The intensity of CIII triplet lines at the same figure measured the same way grows during rump up, plasma shaping and positioning phase of discharge and becomes roughly constant during flat top. It is also possible to see that the mentioned spectral lines of HeII and CIII have comparable irradiance during more than half of the discharge.

Product of normalized QE of PMT based system to plasma radiation measured by minispectrometer in the range of PMT based system operation gives value, which should be proportional to the signal measured by PMT. The normalization was done to maximum of the system QE. On one hand the product does not include influence of parasitic spectral lines that can be hidden in the spectrometer's background. Therefore, it can give up to 6% lower value. On the other hand, the product does not include losses of radiation in PMT based system because of alignment between its components. Therefore, value can be higher than measured one. It is possible to see in figure 1.3.8a that the product and the value of CIII measured by PMT based system are comparable. It means that the source of possible disagreements of these two values does not play significant role for the case of this system.

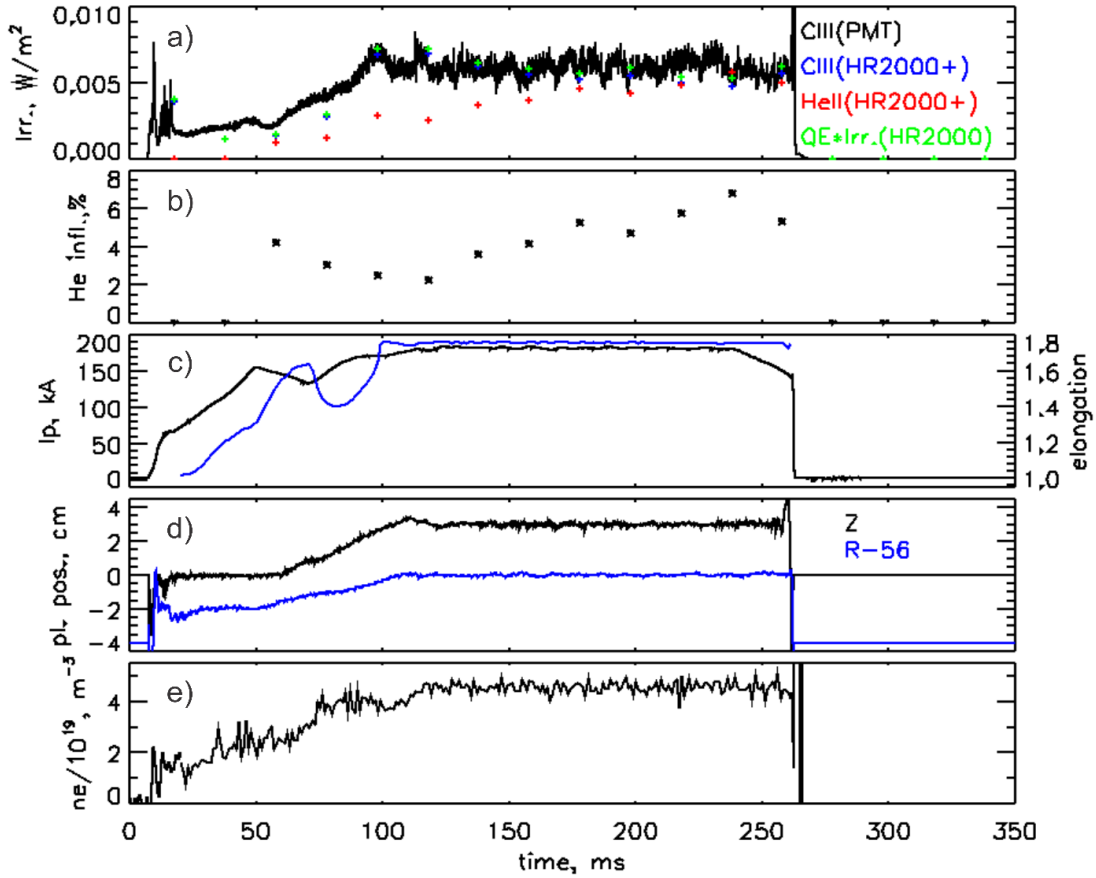

Figure 1.3.8. a) CIII measured by PMT-based system (black), wavelength integrated value of CIII triplet (blue) and HeII (red) spectral lines radiation measured by minispectrometer, product of normalized QE of PMT based system and plasma radiation in the range of interest (green). b) the expected influence of helium parasitic spectral line to resulting CIII signal measured by PMT based system in per cent calculated on the base of spectroscopic measurement. c) plasma current (black) and elongation (blue), d) vertical Z and horizontal R plasma position, e) plasma density.

The influence of HeII parasitic spectral line to resulting CIII signal of PMT based system is shown in figure 1.3.8b. It is possible to see continuous growing of this value during the discharge. The value increases up to 6%.

Based on information given above it is possible to conclude:

1. The influence of parasitic helium line to the CIII signal continuously grows during the discharge and gets to maximal value at the end of the discharge.

2. The influence of parasitic helium radiation to resulting CIII signal is only 4-6% for the case when helium and carbon spectral lines have comparable intensity. The value gets to 13% for the case of twice more intensive helium line than

carbon one. Therefore, the influence of parasitic spectral line becomes significant only in discharges with high helium content.

1.3.2.7. Temporal dependence of vacuum window transmittance

The glow discharge cleaning [18] and boronization [19] techniques are commonly exploited in tokamaks in order to get suitable vacuum conditions for high-temperature discharges. Glow discharges are often used for a removal of atmospheric gases adsorbed on the surface of the vacuum chamber. Additionally, boronization is applied to gather oxygen and other elements at the vessel walls during the discharge. It is reached by covering of the vessel surfaces by thin layer of boron. We use a glow discharge in carborane ($C_2B_{10}H_{12}$) for boronization of the vacuum chamber of our tokamak.

We studied the evolution of emission spectrum during the experimental campaign on the COMPASS tokamak. The evolution of signal was measured by PMT based system for Bremsstrahlung radiation measurement in line free region around 523 nm during experimental campaign as shown in figure 1.3.9.

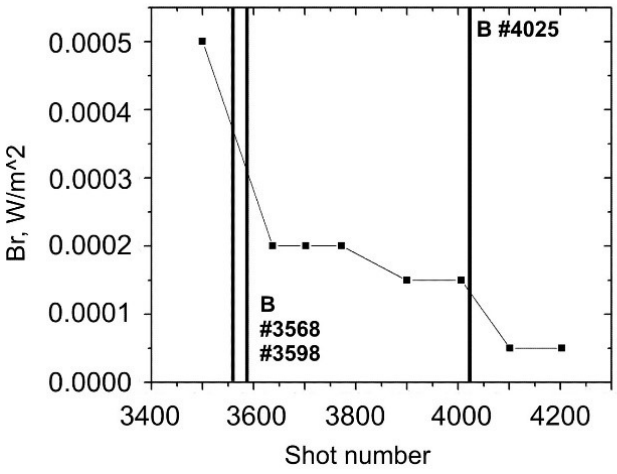

Figure 1.3.9. Evolution of measured Bremsstrahlung radiation over the experimental campaign plotted for discharges with comparable parameters.

Comparison was done for flat top part of discharges with comparable plasma position, shape, electron density and electron temperature. A significant drop of signal 2-3 times after each boronization is observed. From existing measurements, it is also possible to conclude that additional re-deposition of boron, carbon and wall

material take place from discharge to discharge during experimental campaign and leads to farther decreasing of signal.

We observed that spectral lines in range up to 460 nm disappeared till the end of campaign (see figure 1.3.10).

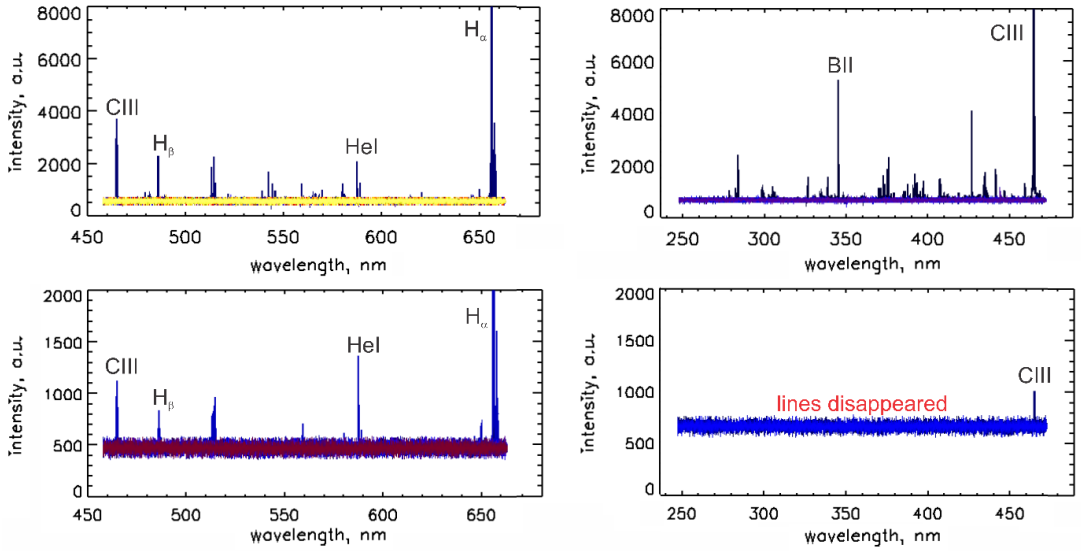

Figure 1.3.10. Spectra measured by the minispectrometer in VIS (left) and near UV (right) ranges at the beginning (top) and at the end (bottom) of the experimental campaign after few boronizations.

We suppose that it is mainly result of boronization and also redeposition of vacuum wall materials and carbon plates during discharges.

After the end of experimental campaign, the vacuum window used for the spectroscopic measurements was removed from the tokamak vessel and changes of its properties were investigated. A layer of the deposited material was found on the window. Then, the spectrally resolved transmittance of the deposited layer and its homogeneity was measured in the laboratory using the white-light source. The results are shown in figure 1.3.11. No dependence of the window transmittance on position over the window was found. Insignificant scattering of measured points at the figure can be explained by improper alignment of the window with semi-reflective film. Decrease of transmittance was caused by a gradual layering of the sputtered first wall material and boronization of tokamak chamber. The window was cleaned by alcohol and HCl and its transmittance was re-measured. To avoid this problem, shutter was designed and installed during next opening of the tokamak vessel to protect spectroscopic windows from sputtered material during glow discharges cleaning and boronization.

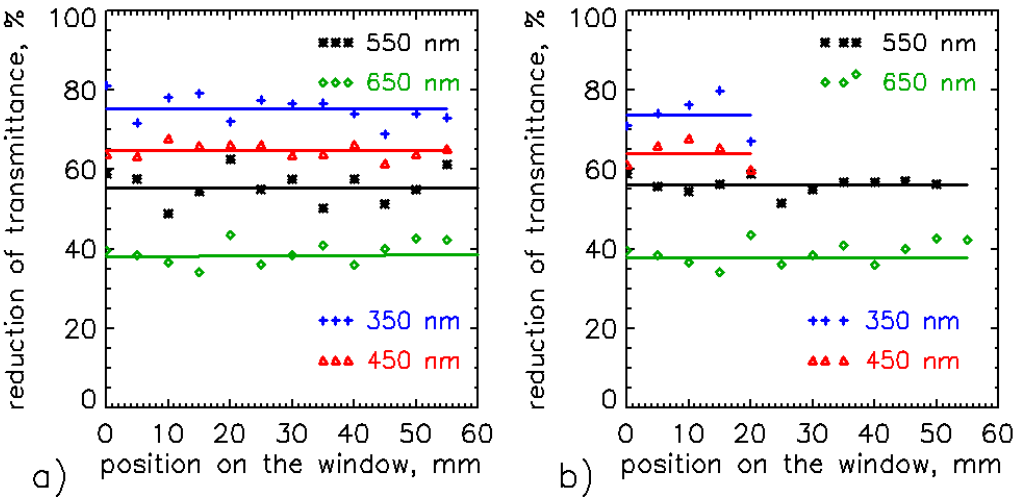

Figure 1.3.11. Spatial profile of the transmittance reduction of the vacuum window measured relatively in a) poloidal and b) toroidal direction on the window. Measurements were done by movement along the window with the step about 5 mm.

Spatially averaged dependence of the window transmittance on wavelength is plotted in Figure 1.3.12.

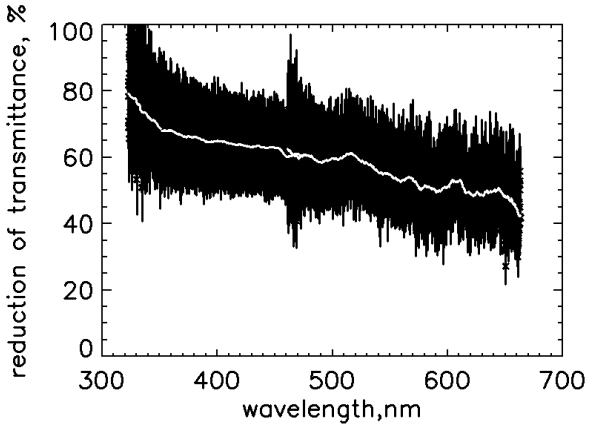

Figure 1.3.12. Spatially averaged reduction of vacuum window transmittance in connection with the deposited layers measured by two minispectrometers in UV and visible spectral range. Accuracy of measurements is indicated by the black curve.

The transmittance decreases more for shorter wavelengths as it was expected from the typical deposited layer thickness well below several tenths of nanometer [20]. Accuracy of the window transmittance measurement is about 20% and it decreases approaching near UV region due to the limited intensity of the used white-light source in this spectral region in combination with a lower transmittance of the deposited layers there, see figure 1.3.13.

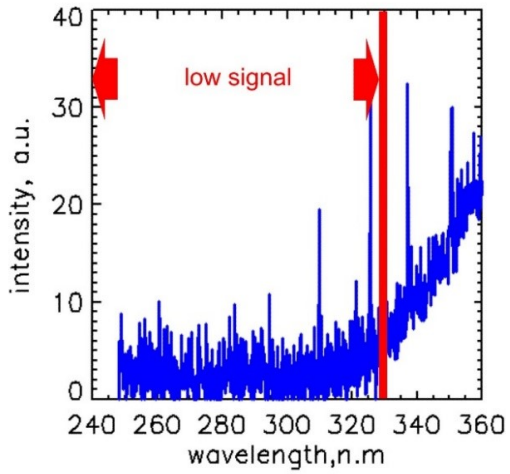

Figure 1.3.13. Limitation of the window transmittance measurement by a low detected signal.

Qualitative analysis of atomic composition of the deposited layers located on the surfaces of shutter of the port plug used for spectroscopic measurements both exposed to boronization and high-temperature plasma, and shielded against boronization but exposed to plasma only was performed by energy-dispersive spectrometry (EDS) [21]. The investigation was performed using the scanning electron microscope EVO MA15 (Carl Zeiss SMT, Germany) for three different locations in both cases. The results of this measurements are presented in table 2. The area exposed to boronization shows significant boron content, and an increase in oxygen and carbon contents. The amount of elements included in the shutter material (Cr, Fe and Ni) decreases for the case of measurements in area exposed to boronization in comparison with clean shutter surface. This is the proof of expected effect of boronization when thin film composed of mainly boron covers all parts of the first wall. However, this method does not provide any information on the thickness of the boron deposit.

	B	C	O	Cr	Fe	Ni
clean1	0.0	5.0	0.7	14.8	68.9	10.6
clean2	0.0	4.9	0.8	15.3	68.7	10.2
clean3	0.0	6.3	0.7	14.9	67.9	10.2
dirty1	36.3	9.4	2.6	8.1	37.6	6.0
dirty2	36.0	8.9	2.4	8.2	38.4	6.0
dirty3	35.8	9.2	2.5	8.1	38.4	6.0

Table 2. Results of qualitative analysis of elemental composition for clean and dirty metallic part of spectroscopic port plug.

Many vacuum windows are expected to be used in different types of optical diagnostics at ITER, such as spectroscopic, Thomson scattering (TS), interferometric etc [22]. The discussed effect of wall material film layering at the window is expected. The decrease of transmittance of the windows during the tokamak operation must be known for correct estimation of received data.

It is clear, however, that a material re-deposition on the spectroscopic window during tokamak discharges cannot be prevented and has to be taken into account in processing of experimental data. It is also clear that all spectroscopic windows have to be cleaned at any opening of the tokamak vessel to atmospheric pressure.

1.3.2.8. Errors caused by data collection and data processing

Noise in spectra can be also increased during data collection by the spectrometer. First source of errors is connected with sensitivity of spectrometer detector, for which the time of integration can be properly selected to achieve reasonably high values of signal to noise ratio (figure 1.3.14a); but anyway it exists minimal measurable level of radiation which corresponds to minimal measurable level in temporally integrated discharges in our case. It is $1.5 \cdot 10^{-4}$ W/(nm*m^2) for the minispectrometer in spectral range 457.83-663.18 nm. All spectral lines, which have lower intensity than this level, cannot be measured by the spectrometers. It means that for absolute sensitivity measurements it is principal to specify power window (the minimal and maximal measured power) to which the discussed spectra correspond. We should also remember that our system has wavelength dependent transmittance. It means that low intensity spectral lines can be missed in regions with low sensitivity (figure 1.3.14b), and at the same moment for the same integration time high intensity lines can get to saturation in the region with high sensitivity. For example, integration over 20 ms of the discharge (see figure 1.3.14d) gives 0.2 W/(nm*m^2) as minimum and 2.71 W/(nm*m^2) as maximum measurable value of spectral irradiance for the spectrometer with operational range 457.83-663.18 nm at wavelength 656.27 nm. It means in our case the H_α spectral line is in saturation.

Additional error can appear during data processing. Incorrect removal of detector noise can cause presence of in reality non-existing spectral lines as well as losing of some plasma spectral lines. In our case noise parameters were calculated from dark frames that were measured by spectrometers after the end of each discharge. Points above a sum of mean noise level value and variance of noise value

were considered as spectral lines. Spectral line level was calculated as a difference between raw signal and mean noise level (figure 1.3.14c).

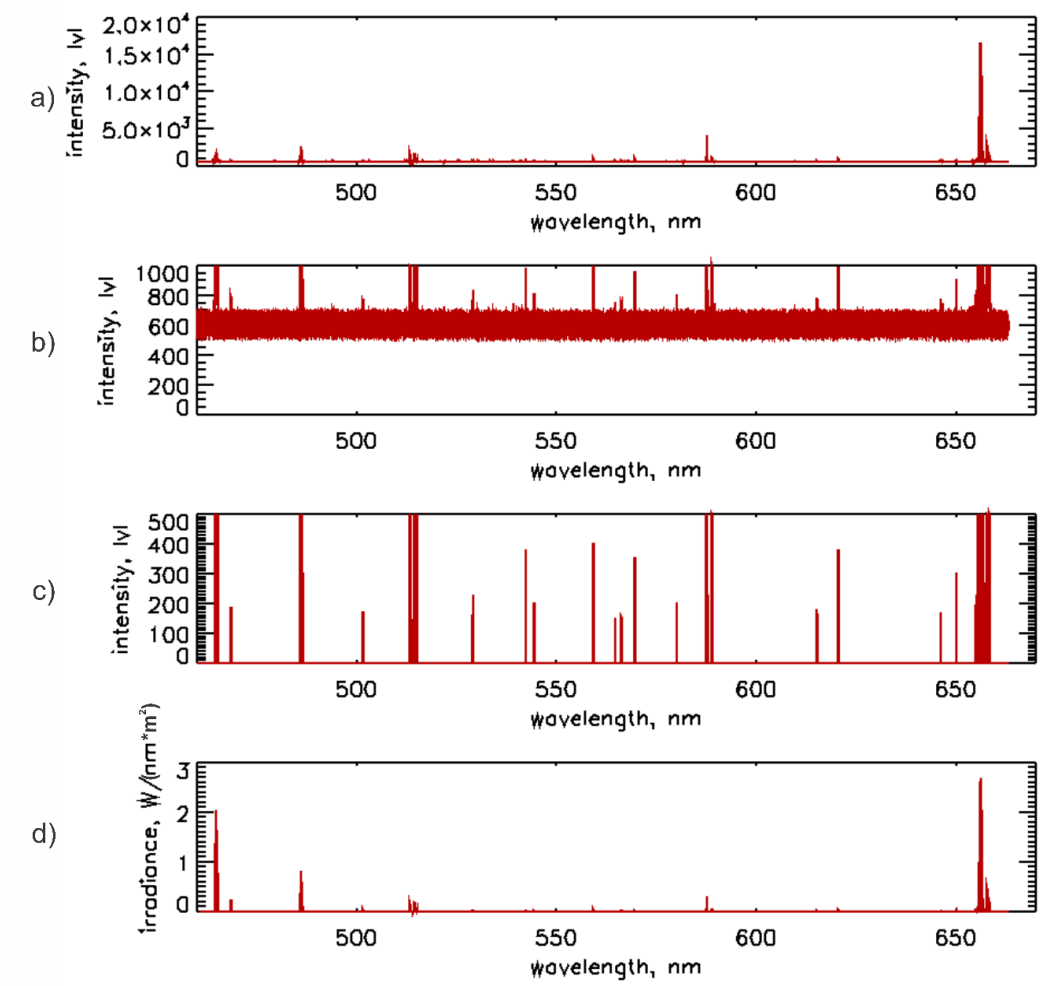

Figure 1.3.14. a) raw spectrum measured during shot # 4648 by minispectrometer in range 457.83-663.18 nm, b) zoom of the top panel to see level of background noise of the spectrum, c) spectrum with removed background, d) resulting spectral irradiance.

Spectral irradiance is a radiation per nanometer measured at a surface in space which diagnostic observes. To recalculate measured levels to spectral irradiance absolute sensitivity calibration constant should be used (figure 1.3.14d). To convert measured spectral irradiance into values of local radiance, the source parameters (plasma shape and radiation distribution) must be known, i.e. in the tokamak case it is the magnetic configuration and the position of radiation shells. In such a way, an additional source of imprecision is introduced by inclusion of both the magnetic field reconstruction (calculated by EFIT [23]) and the temperature and density profiles.

1.3.2.9. Influence of measurement geometry and plasma wall interaction to the measured signal

Since high-temperature plasma is created in tokamaks, it contains atoms and ions of working gas and impurities in different ionisation stages. Tokamak plasma has strong gradients of both electron density and temperature at the edge. This leads to a rapid change of ionisation states of impurities with minor radius in this region and appearing of series of concentric radiation shells for each ionisation state. Each shell appears, where electron temperature is approximately one third of required ionisation energy due to Maxwell distribution of electron velocities [24]. The tokamak plasma is transparent for visible and UV radiation, therefore, these shells can be observed experimentally.

Assuming the isotropic radiation source, we can use an inverse-square law to estimate a ratio of contributions of radiation shell from HFS (High field side) and LFS (Low field side) (see figure 1.3.15):

$$\frac{I^*_{LFS}}{I^*_{HFS}} = \frac{R^2_{HFS}}{R^2_{LFS}} \tag{1.3.1}$$

Where I^*_{LFS} is radiation coming to the detector from unit area of radiation shell at LFS, R_{LFS} is distance from diagnostic input to radiation shell at LFS, I^*_{HFS} is radiation of unit area of shell at HFS and R_{HFS} is distance from diagnostic input to radiation shell at HFS.

Radiation coming to detector from unit area of shell at LFS and HFS is:

$$\begin{aligned} I^*_{LFS} &= I_{LFS} / S_{LFS} \\ I^*_{HFS} &= I_{HFS} / S_{HFS} \end{aligned} \tag{1.3.2}$$

Where I_{LFS} is radiation measured by the detector from LFS part of the radiation shell through surface S_{LFS}, I_{HFS} is through surface S_{HFS}. Then we can substitute (1.3.2) to (1.3.1):

$$\frac{I_{LFS}}{I_{HFS}} = \frac{R^2_{HFS} S_{LFS}}{R^2_{LFS} S_{HFS}}$$

For the set-up without lens, the surfaces S_{LFS} and S_{HFS} are given by numerical aperture of the fibres (NA ~ 0.22). From EFIT reconstruction, we get observed surface of radiation shell for circular plasma at LFS S_{LFS}; in case without lens it is equal approximately to 34.5 cm^2 (at the distance from the system input to radiation shell equal to 14.0 cm). Observed surface of radiation shell at HFS S_{HFS} is 500 cm^2

(at the distance 52.2 cm). In the case of divertor plasma it is 25.3 cm^2 at LFS (distance 12 cm) and 383.2 cm^2 at HFS (distance 47.3 cm). In result we get a conservation of etendue law $I_{LFS} \sim I_{HFS}$ for the geometry without lens in both plasma configurations.

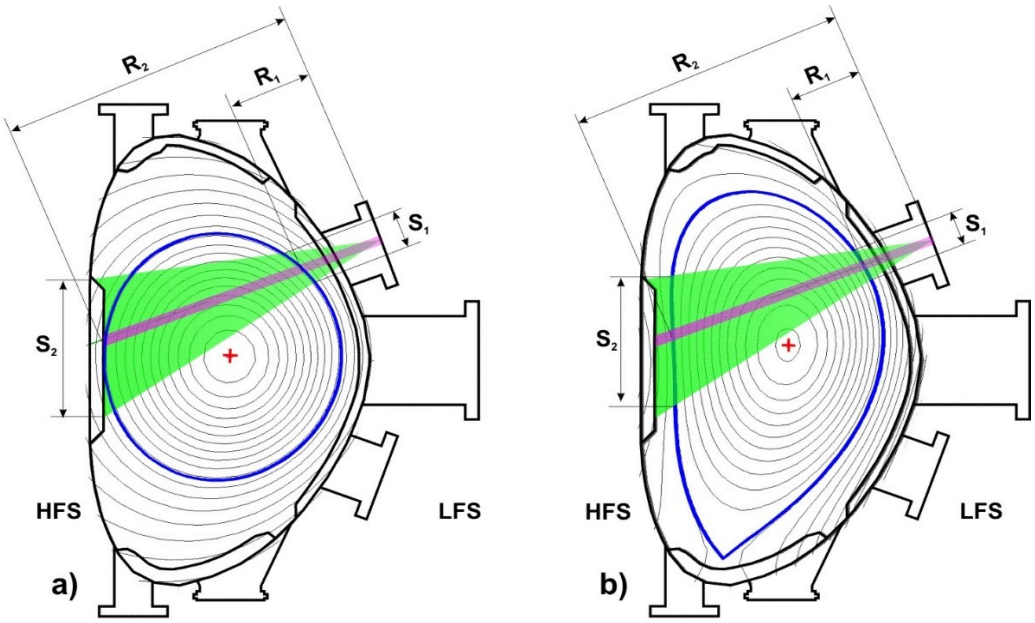

Figure 1.3.15. Poloidal cross-section of the COMPASS tokamak at the typical magnetic configurations. Left – circular plasma cross section, right – divertor configuration. The magnetic surfaces (grey lines), the last closed plasma surface (blue line) and plasma centre (red cross) are determined by the EFIT reconstruction. The observation volume of the optical diagnostics equipped with the collecting lens is shown by violet colour, the one without lens is shown by green colour.

Let's do the same calculation for the case of the collecting lens installed at the entrance of the diagnostic system. Area of lens S_{lens} is 3.79 cm^2. We use parallel ray approximation i.e. we suppose that the observed surfaces from the both parts of radiation shell are equal $S_{LFS}=S_{HFS}=S_{lens}$. The same calculation gives $I_{LFS} >> I_{HFS}$ for the case with lens in both plasma configurations.

It means that for all plasma configurations we will measure the signals with fibre and lens as:

$$I_{fibre} \sim I_{LFS} S_{LFS\_fibre} + I_{HFS} S_{HFS\_fibre}$$
$$I_{lens} \sim I_{LFS} S_{lens}$$

It allows supposing that case without lens corresponds to line integrated measurements and at the same time using of lens in our diagnostic configuration leads to local measurements of plasma radiation at LFS.

In figure 1.3.15, from the EFIT reconstruction of the plasma discharge it is possible to see that in the case of the circular configuration plasma touches the inner column covered by carbon plates. One can expect that radiation is stronger close to the touch point because of strong plasma wall interaction, i.e. carbon erosion, and consequent carbon (and also released hydrogen) emission. It means, that in reality for circular plasma the signal from HFS always dominates $I_2^* > I_1^*$.

The important parameters of semi D-shaped and circular discharge are presented in figure 1.3.16 to prove this effect.

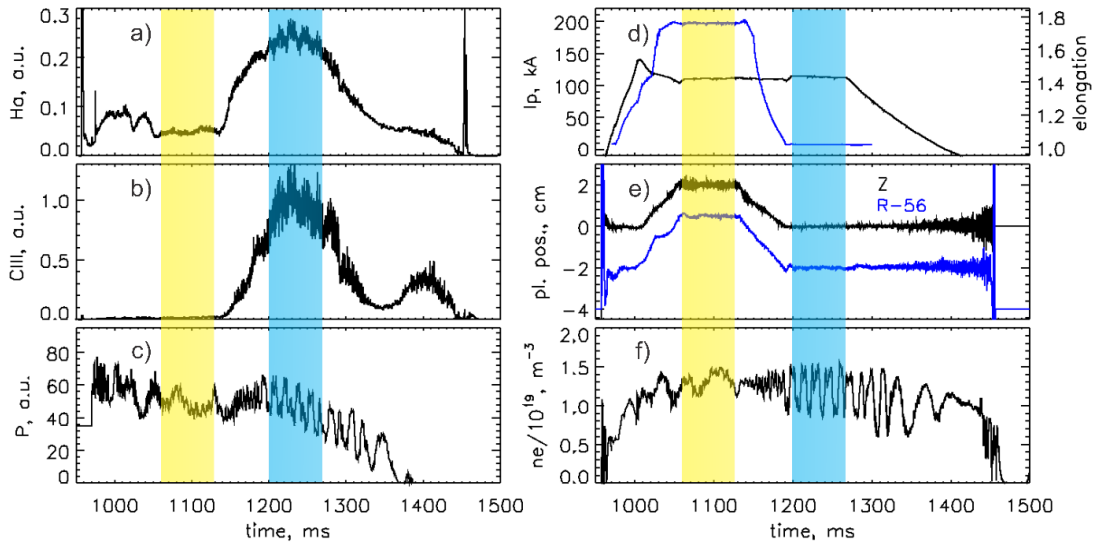

Figure 1.3.16. Temporal evolution of a) Halpha and b) CIII spectral lines, c) gas puffing, d) plasma current (black) and elongation (blue), e) vertical and horizontal plasma position and f) plasma density during semi D-shaped and circular discharge #6305.

All shown discharge parameters were corrected to actual plasma geometry and plasma position using EFIT reconstruction along diagnostics chord. In figure 1.3.16a a temporal evolution of radiation of working gas (hydrogen alpha spectral line at 656.27 nm) is shown. Figure 1.3.16b shows radiation of wall material (CIII triplet at about 465.0 nm). Now we can compare spectroscopic signals during flat-top phase of the discharge for both plasma configurations. The flat-top phase of the D-shaped discharge is approximately at 1080-1120 ms, flat-top of the circular part is at 1205-1260 ms. At the same time plasma has a stable plasma position (figure

1.3.16d). In figure 1.3.16e temporal evolution of line average plasma density is shown. Density oscillations are connected with changes of gas puffing (figure 1.3.16f) given by the feedback density control system.

The difference in spectroscopic signals between two parts of discharge with different plasma configurations is approximately 5 times for hydrogen and 50 times for carbon.

2. Data processing and results

The radiation field in a plasma can originate from three types of radiative transitions: bound-bound transitions, bound-free transitions and free-free transitions. Line radiation emitted from a bound-bound transition has a peak intensity at a frequency corresponding to the energy difference between two bound levels. Radiation emitted from bound-free transitions is recombination radiation whose radiation frequency corresponds to the sum of the kinetic energy of the recombining electron and the binding energy of the shell that the electron falls to. Recombination radiation has a discontinuity at the frequency corresponding to the binding energy and it is distributed over higher frequencies starting at the threshold frequency. Bremsstrahlung radiation is emitted from free-free transitions when a free electron loses its kinetic energy in a collision with electrons and ions. The emitted radiation frequency corresponding to the change in electron kinetic energy, is distributed continuously over all frequencies. Recombination radiation and Bremsstrahlung radiation are called continuum radiation since their intensities are distributed over a wide range of frequency unlike line radiation whose intensity is peaked at a line-centre frequency.

2.1. Spectrally resolved plasma radiation measurements

The minispectrometers described above are used for measurements of plasma radiation in our tokamak. The wavelength calibrations of the minispectrometers were done by producer. The calibration method is properly described at the Ocean Optics web page [26].

The result signals measured by four minispectrometers are presented in figure 2.1.1a. The aim of these measurements was investigation of impurities spectral lines, therefore temporal integration during discharge duration was used to collect as much light as possible. The huge difference in intensity between the spectral lines lead to saturation of the most intensive spectral lines in the spectrum belonging to HeI (587.5 nm) and Hα under such a measurements conditions. It is also possible to see different sensitivity of the spectrometers reflected in different background level. The influence of background radiation to our measurements and also precision of measurement was properly discussed above.

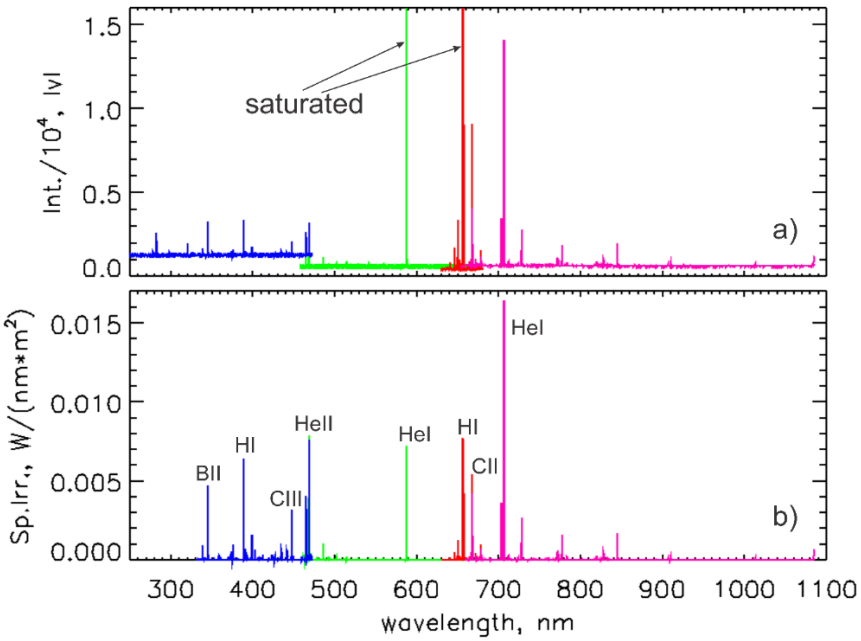

Figure 2.1.1. Spectrum of typical D-shape discharge measured at COMPASS tokamak: a) measured signal in the range 247-1084 nm, b) recalculated plasma radiation in the range 330-1084 nm with interpretation of main spectral lines using NIST database.

The recalculated plasma radiation is presented in figure 2.1.1, b. It is possible to recalculate the wavelength range above 330 nm because of the wavelength dependence of calibration source radiation which was discussed above, but the lines observed up to 330 mn are included in the list of observed lines as well.

2.1.1. Spectra interpretation methods

Mainly hydrogen\deuterium plasma in tokamaks has very different concentration of different impurities. For instance, the amount of helium, boron and carbon in our plasma is significant. Very low concentrations of other impurities relative to working gas lead to the fact that the number of observable lines of the impurities is found to decrease with decreasing concentration until only the most "persistent" or "sensitive" lines remain. The strongest persistent lines usually include one or more resonance lines, i.e., transitions to the ground level or term. Chance to measure such lines depend on the plasma parameters, the spectrometer, and other features of the experiment. Therefore, a relatively small group of lines observed over a broad range of experimental conditions can be specified for each element.

The two sources were used for interpretation of calculated plasma radiation. The NIST (National Institute of Standards and Technology) database was used for

the beginning. The FLYCHK code was used later to interpret spectrum, to model radiation shells of each impurity and to calculate spontaneous emission rate used for ion density estimation.

2.1.1.1. NIST data base

One of the widely used atomic databases is NIST atomic database [27]. Official release of first version of online NIST database was approved in year 1995. Nowadays this is the biggest spectroscopic database. All atomic spectra are available up to atomic number 110. This is database based on experimental results received by National Institute of Standards and Technology and by other authors and institutes. The wavelengths for many spectra have been taken from Reader et al. [28]. The data are updated to newer if they are available from other sources. Explanations of the notations for the different coupling schemes and of the arrangement of the data can be found in [29], [30] and online as a part of the "Help" section.

The typical example of NIST data base operation for helium in total operational range of COMPASS tokamak spectroscopic system is shown in figure 2.1.2.

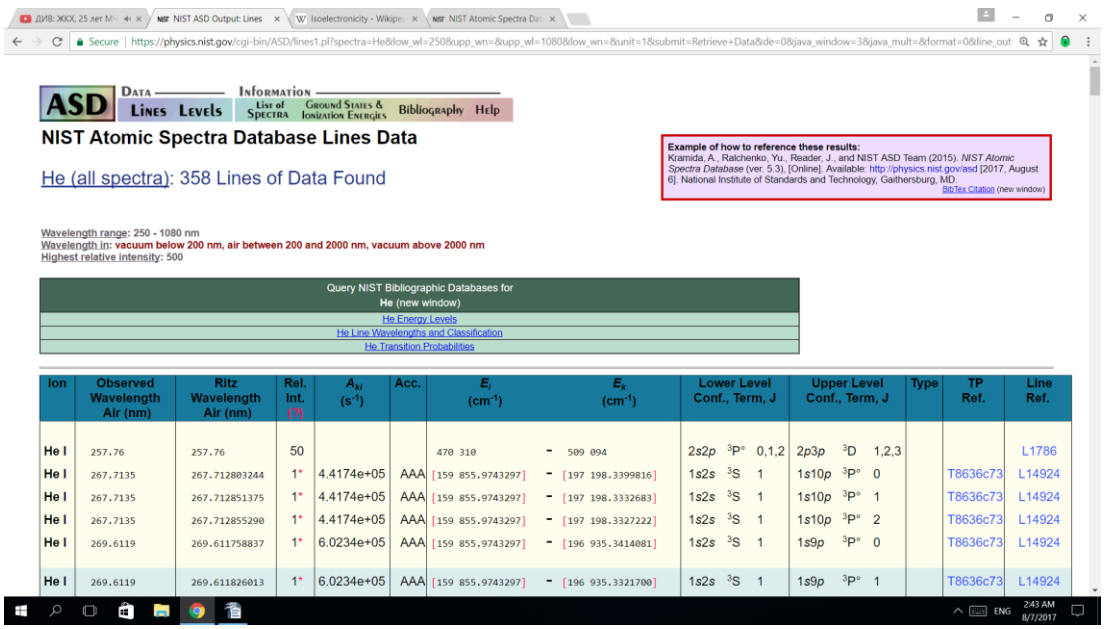

Figure 2.1.2 The print screen of a typical result of NIST database operation.

The recommended references are available just above the table. The table includes from right to left: ion state, wavelength of observed spectral line, Ritz wavelength derived from the difference in level energies, relative intensity, transition

probability A_{ki}, “Acc.” is accuracy of transition probabilities value, E_i and E_k are lower and upper energy levels. After follows configurations, terms and total electronic angular momenta of the lower and upper energy levels. “Type” means transition type and multipolarity, “TP ref” links to a popup window showing bibliographic reference for transition probability, “Line ref” links to a popup window showing bibliographic reference for spectral line.

Precision of wavelength position of spectral lines given in the database depends on resolution of the spectrometer used for the measurements. The relative intensities of the spectral lines observed for any element depend upon the light source and excitation conditions. Thus, even if the relative intensities observed in a particular experiment are adjusted taking into account the wavelength dependence and the sensitivity of the spectrometer and detector, the intensities will in general be different from relative intensities given by another observer in another experiment or tabulated in the database. The relative intensities for most spectra in NIST database are based on values from [28]. Therefore, the lines intensities and their relative values given in the NIST database will not be used in COMPASS tokamak plasma spectra interpretation.

The NIST transition-probability compilations include values with uncertainties ranging from 1% to more than 50%, with an approximate uncertainty range being indicated for each line by an assigned letter. Therefore, these values were used only for comparison with FLYCHK code results or in the case when FLYCHK did not suppose existence of the observed lines.

The second and the third column of the table in attachment 1 contains the interpretation using the NIST online database of spectrum observed in COMPASS tokamak plasma in one of discharges with typical discharge parameters and for the case of extremely strong plasma surface interaction caused by damaging of magnetic diagnostic shielding in the result of which plasma directly heats the shielding. Low resolutions of our spectrometers do not allow to interpret the most of spectral lines unequivocally. Therefore, all possible interpretations are presented. All substances composing first wall were considered as possible source of impurities spectral lines. As a result, it is possible to conclude that except helium, carbon and boron there are lines of oxygen in typical spectra corresponding to typical discharges conditions. In the case of extremely strong plasma wall interaction the spectral lines of elements

from which consist first wall material INCONEL 625 become observable (see table 3).

Ni	Cr	Fe	Mo	Nb	Co	Mn	Al	Ti	Si	C	S	P
58	20-23	5	8-10	3.15-4.15	1	0.5	0.4	0.4	0.5	0.1	0.0.15	0.0.15

Table 3. INCONEL 625 composition.

2.1.1.2. FLYCHK code

Computer code FLYCHK [31] has been successfully employed to study hot dense plasmas for decades. The first version of the code was developed on the base of FLY and HULLAC codes in year 1995. The number of the atomic elements which can be modelled by the code is only from 1 to 79. The code is able to create spectra using four approximations: thermodynamic equilibrium, local thermodynamic equilibrium, corona and collisional radiative models.

The important for us approximations and formulas were taken from the manual of FLYCHK code are given below.

The local population distribution [24] in a collisional-radiative (CR) model is determined by balancing collisional processes of local nature and radiative processes of non-local nature. In a CR model, atomic level populations are calculated by solving multi-level, atomic rate equations self-consistently with a radiation field. Rate equations for level populations are constructed with rate coefficients of collisional and radiative processes computed by atomic physics codes. The radiation field which induces stimulated radiative processes is computed from a radiation transport equation, which brings in non-local contributions to population distribution calculations. Due to such non-local effects arising from radiative processes, population distributions can have a spatial gradient even when there is no gradient in plasma parameters such as temperature and density.

Although the FLYCHK uses some transport equation for the description of radiative processes it is not the transport code in its classical meaning, because any particle fluxes are included in the code anyhow. It means the amount of particles in exact state changes only because of radiative transitions.

The CR models have been developed also for plasmas in magnetic fusion devices such as tokamaks. It allows not only modelling of real plasma spectrum and its interpretation, but also to estimate the impurity ion concentration and

corresponding radiation cooling rate through spectroscopic measurement during steady-state operation phase in tokamaks.

Let us specify basic definition used in atomic rate and radiation transport equations used for spectra generation.

The specific intensity of radiation I(**r**,**n**,ν,t) at position **r** in direction **n**, with frequency ν is defined as the amount of energy δε that is carried by radiation of frequency interval (ν, dν), across the surface element **dS** into a solid angle **dΩ** in a time interval dt:

$$\delta\varepsilon = I(r,n,\nu,t)n \cdot dSd\Omega d\nu dt$$

The mean intensity J(**r**,ν,t) is defined as the average of the specific intensity over all solid angles, written as:

$$J(r,\nu,t) = \frac{1}{4\pi}\oint I(r,n,\nu,t)d\Omega$$

The frequency-averaged mean intensity, $\bar{J}$ which is used in the calculations of bound-bound transition in the CR model, is given as:

$$\bar{J}(z,\nu,t) = \int J(z,\nu,t)\phi(\nu)d\nu$$

where J(z,ν,t) is the mean intensity and φ(ν) is the line profile.

The rate equation for atomic level i can be written as:

$$\frac{dn_i}{dt} = -n_i\sum_{j\neq i}^{N_L} W_{ij} + \sum_{j\neq i}^{N_L} n_j W_{ji} \qquad 1 \le n_i \le N_L$$

For upward transitions (i < j),

$$W_{ij} = B_{ij}\bar{J}_{ij} + n_e C_{ij} + \beta_{ij} + n_e\gamma_{ij} + \sigma_{ij} + I_{ij}$$

For downward transitions (j > i)

$$W_{ji} = A_{ji} + B_{ji}\bar{J}_{ji} + n_e D_{ji} + n_e\alpha_{ji}^{RR} + n_e\kappa_{ji}^{EC} + n_e^2\delta_{ji}$$

where n_e is an electron density and $\bar{J}$ is a frequency-averaged mean intensity which is relevant to the transition. The subscript ji refers to a transition from level j to level i.

The rate coefficients correspond to the following atomic processes:

A_{ij} spontaneous emission, B_{ij} stimulated absorption (i < j) or emission (i > j), C_{ij} collisional excitation, D_{ij} collisional deexcitation, I_{ij} beam and non-thermal electron collisions, α_{ji} radiative recombination, β_{ij} photoionization plus stimulated recombination, γ_{ij} collisional ionization, δ_{ji} collisional recombination, κ_{ji} electron capture and σ_{ij} autoionization.

The radiation transport equation is written in terms of the specific intensity I(**r**,**n**,ν,t) as:

$$\left[\frac{1}{c}\frac{\partial}{\partial t}+n\cdot\nabla\right]I(r,n,\nu,t)=\eta(r,n,\nu,t)-\chi(r,n,\nu,t)I(r,n,\nu,t)$$

where η(r,n,ν) is an emission coefficient or emissivity and χ(r,n,ν) is an absorption coefficient or opacity.

Boundary conditions for general laboratory plasmas can be specified as that there is no incoming radiation from the outmost boundary. The derivative of the specific intensity at the centre is assumed as zero for the symmetry condition around the centre.

In tokamak plasmas, the variation of radiation intensity in time is assumed to be smaller than in space and the time-dependence of the radiation field is neglected. The tokamak plasma is optically thin. It means no absorption of radiation by plasma takes place.

The emission coefficient is written in terms of the absorption cross sections, $\alpha_{ij}(\nu)$ for bound-bound transitions, $\alpha_{i\kappa}(\nu)$ for bound-free and $\alpha_{\kappa\kappa}(\nu,T)$ for free-free transitions:

$$\eta(\nu)=\frac{2h\nu^3}{c^2}\left[\sum_i\sum_{j>i}(g_i/g_j)n_j a_{ij}(\nu)+\sum_i n_i^* e^{-\frac{h\nu}{kT}}\alpha_{ij}(\nu)+\ldots+\sum_k n_e n_k \alpha_{kk}(\nu,T)e^{-\frac{h\nu}{kT}}\right]$$

where n^*_i denotes the LTE population of state i from the Saha-Boltzmann formula.

Modelling of synthetic spectrum for each impurity (with atomic number less than 71), which can present in our plasma, was done to interpret measured spectrum (shown in figure 2.1.1) in the range 247-1084 nm for the beginning using local values of electron temperature and density measured by TS and estimated averaged Zeff value (see figure 2.1.3).

The FLYCHK does not include any calculation connected with plasma wall interaction or such a process like material sublimation under influence of strong plasma radiation. Probably it can be the main reason of absence of neutral atoms or low ionized impurities ions spectral lines in modelled spectrum.

The same observed and measured spectral lines have quite different intensity. It can be connected with two facts. Measured plasma radiation spectrum is averaged in quite large volume of inhomogeneous plasma observed by the spectroscopic diagnostic with integration over all radiation shells in some space angle (limited by

numerical aperture of optical fibre). Each modelled spectrum was done just for small plasma volume 0.1 mm^3 with the same plasma parameters. Therefore, the modelled spectrum can be valid in some thin layer of real plasma with parameters used in the model. Second phenomenon which can influence the spectral lines radiation is plasma-wall interaction leading to charge exchange processes which result in increasing of low ionized ions radiation and decreasing of high ionized ions radiation.

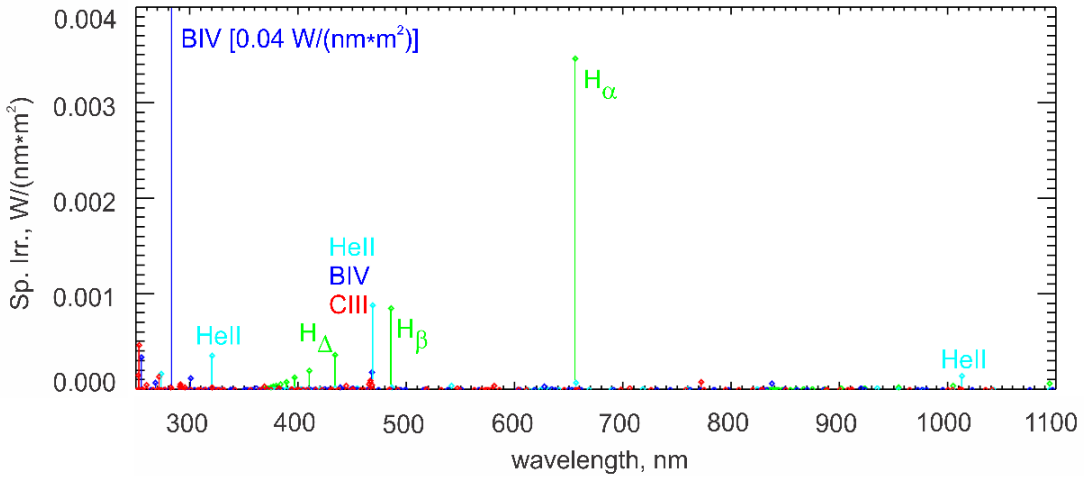

Figure 2.1.3. The sample of synthetic spectrum modelled by FLYCHK code for plasma layer with T_e=35.8 eV, n_e=2.68·10^{19} m^{-3} and Z_{eff}=1.35.

The result of FLYCHK model interpretation of measured spectral lines is presented in the table in attachment 1. The low resolutions of our spectrometers do not allow to interpret the most of spectral lines unequivocally. All possible variants are present.

Only the brightest lines in modelled spectrum are measured by our spectrometers. They belong to hydrogen, helium, carbon, boron or oxygen ions. The model predicts low radiance of the spectral lines of elements (with atomic number less than 71) belonging to wall material INCONEL 625. This low radiance can be the reason why they usually do not appear in measured spectra.

It is possible to see that part of lines are not interpreted by FLYCHK anyhow. First explanation can be that these lines just belong to elements with atomic numbers higher than 71. Second possible explanation is that these lines are result of interaction of plasma with wall which causes desorption or sublimation of wall materials. The brightest of these spectral lines are interpreted using comparison of

temporal evolution of the lines with temporal evolution of interpreted lines and NIST database. During the comparison we suppose that temporal evolution of spectral lines corresponding to different ionization stage and belonging to the same element are similar. This way we found out that the brightest of spectral lines which were not interpreted by FLYCHK, belong to HeI, CII and BII. Unfortunately, this method does not allow to interpret low intensity spectral lines for which any temporal measurements are impossible because of too low intensity of these lines. Therefore, we cannot exclude that they belong to INCONEL 625.

2.1.2 Radiation shells

During our modelling we use local values of electron density and temperature which belong to profiles of these values measured by Thomson scattering. The aim is to model plasma radiation corresponding to the mentioned local plasma parameters. It means we model plasma spectrum corresponding to each value of n_e and T_e in measured profile. Therefore, we can plot profile of all spectral lines in the modelled spectrum as a function of the same coordinates as n_e and T_e.

Let us choose the modelled spectral lines corresponding to measured ones which are interpreted by FLYCHK code and NIST database the same way. Except working gas we choose spectral lines of the impurities which are the most significant for our plasma, i.e. helium, boron and carbon. We choose one spectral line for each ionization stage. We choose spectral line on the base of FLYCHK code and NIST database only if the ion's radiation takes place out of the observation range of our diagnostic. The FLYCHK code models multiple lines as one line. Therefore, we do not use such multiple lines for our radiation profiles. The chosen spectral lines have very different intensities. Therefore, we normalize each spectral line to maximum of radiation corresponding to this line.

In figure 2.1.4 it is possible to see the profiles which belong to circular plasma. The fitted value of plasma temperature and plasma density was used for our modelling in this case. It is possible to see that according to model our plasma does not go to total ionization even at plasma centrum. The FLYCHK code does not predict existing of neutral helium, boron or carbon in our tokamak discharges. Therefore, their profiles are not at the figure.

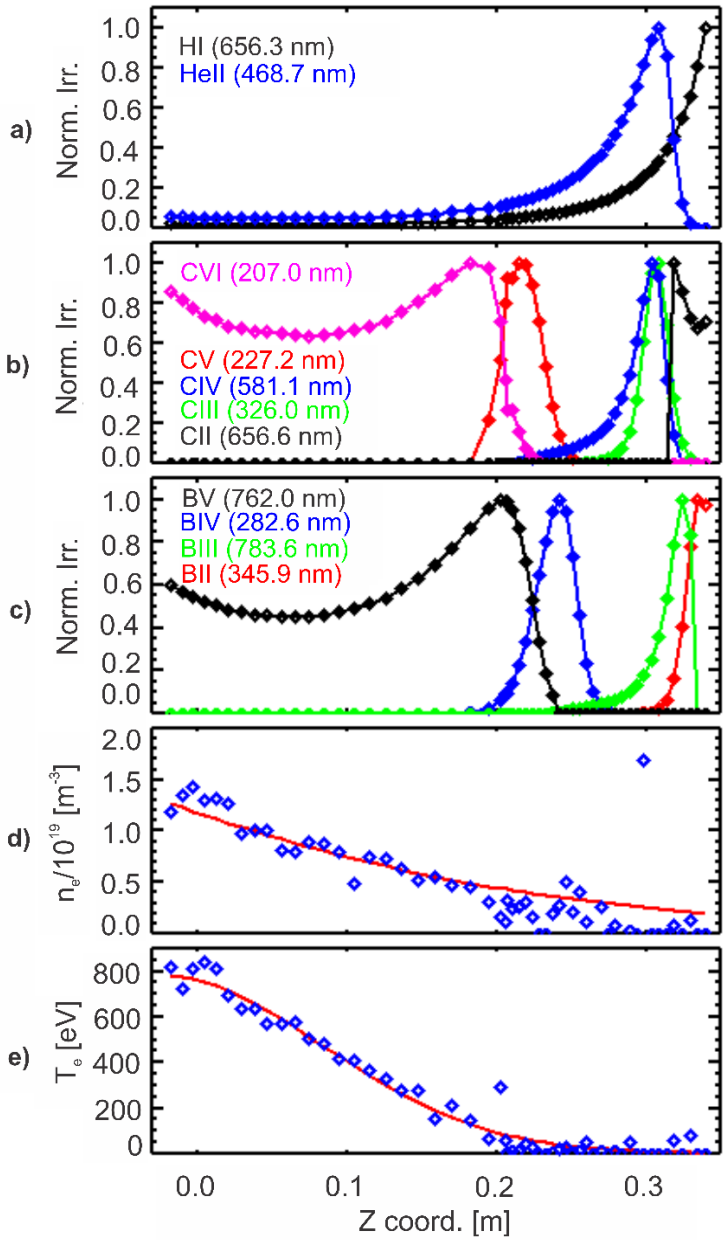

Figure 2.1.4. The case of circular plasma. The radiation shells of a) hydrogen and helium, b) carbon ions, c) boron ions, d) electron density and e) electron temperature profiles measured by Thomson scattering system.

The profiles of the same spectral lines for the case of D-shaped plasma are present in figure 2.1.5. We use measured values of electron temperature and density for modelling of spectra in this case. It is possible to see that in the case of D-shaped plasma the FLYCHK model does not predict existence not only neutral helium, carbon and boron, but also CII and BII ions. Again the plasma does not go to total ionization at the plasma centrum. The radiation shells maximums are shifted closer to the wall.

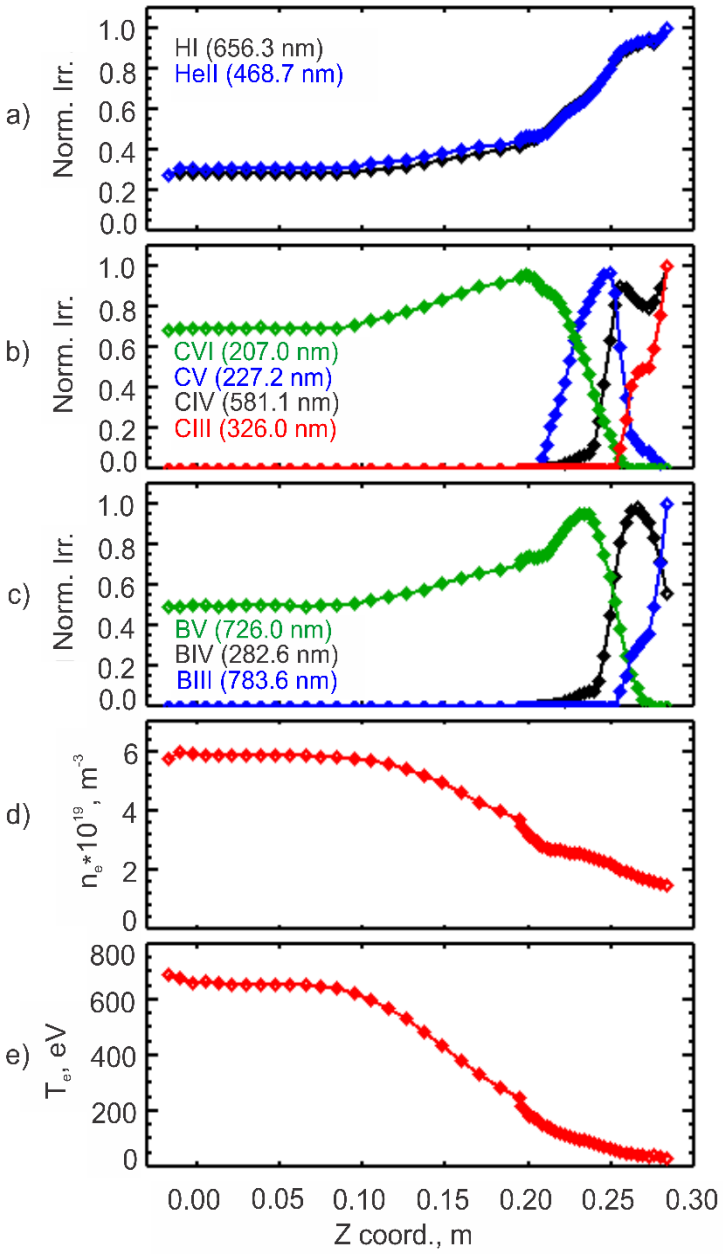

Figure 2.1.5. The case of D-shaped plasma. The radiation shells of a) hydrogen and helium, b) carbon ions, c) boron ions, d) electron density and e) electron temperature profiles measured by Thomson scattering system.

2.1.3 Ion density estimation method

The tokamak plasma is optically thin. The intensity which is integrated along the line of sight s, for a line radiation from level j to level i, can be written as:

$$I_{ji} = \frac{1}{4\pi}\int n_j A_{ji} h\nu_{ji} ds$$

where A_{ji} is an atomic transition probability of level j to i and $h\nu_{ji}$ is an energy of the emitted photon. The quantity n_j is the upper level population density. It means using

measured radiance of exact spectral line and transition probability coefficient of these lines for real plasma conditions modelled by FLYCHK we can get density of atoms in this exact state. Using the brightest lines, we can get values proportional to density of exact impurity in the plasma.

The transition probability coefficient given in NIST database is used in the case of lines which are not modelled by the FLYCHK for impurities density calculation.

The results are presented in the next chapters.

2.2. Effective ion charge estimation

The knowledge of the effective ion charge Zeff, which indicates the degree of plasma pollution, is of high interest, since the tolerable impurity concentration to achieve successful ignition of fusion plasma is limited. It is defined in theory as the averaged charge

$$Z_{eff} = \frac{\sum_i n_i Z_i^2}{\sum_i n_i Z_i}$$

of all present ions in the charge state Z_i, where n_i is the ion density of species i.

Many processes make a contribution to production of plasma radiation in tokamak plasma. Among them it is a continuum radiation arising from electron-ion interaction, as Bremsstrahlung, or as recombination radiation. Bremsstrahlung emitted from plasma usually refers to the radiation created by a free electron during its deceleration in a deflecting electric field of ions [32]. The recombination radiation has a continuous spectrum above a threshold energy corresponding to the binding energy of the captured electron [33].

For Zeff estimation, we use its diagnostic definition:

$$Z_{eff} = \frac{B_{meas}}{B_{calc}}$$

where B_{meas} is the Bremsstrahlung emitted by an impure plasma, which can be measured by appropriate diagnostics, and B_{calc} is calculated Bremsstrahlung emitted by a pure hydrogen plasma of the same electron density and electron temperature and to the same solid angle. Based on the definition given above it is possible to conclude that we received the Zeff value averaged in measured volume.

2.2.1. Measurements of bremsstrahlung radiation of real plasma

The main practical problem of continuum radiation measurements in tokamaks is to find a region of the spectrum unaffected by line radiation of impurity atoms and ions. Usually, measurements of Bremsstrahlung are carried out by recording the plasma emission in a certain wavelength range free of line radiation using interference filters and various types of detectors, but methods of measurements based on spectrometers also exist.

Measurements of the continuum radiation are widely used to determine the effective ion charge.

Let's start with choosing a wavelength range being inspired by the experience of other toroidal devices. Measurements using photomultipliers (PMT) were realized at:

- Alcator C-Mod using 3 nm bandpass interference filter, centred at 536 nm [34],
- Tore Supra using 1 nm bandpass interference filter, centred at 523.8 nm [35],
- MAST using 1 nm bandpass interference filter, centred at 521.3 nm [36],
- DIII-D (Doublet III-Divertor) using 2 nm bandpass interference filter, centred at 523.5 nm [37].

Spectroscopic measurements were used for a detection of Bremsstrahlung radiation at:

- JET and ASDEX: the continuum emission is measured in the line-free region around 523.5 nm [38],
- HT-7 (Hefei Tokamak-7): central wavelength was 578 nm; wavelength range 2 nm [39]
- LHD (Large Helical Device): next to 530 nm [40].

The spectroscopic measurements using the minispectrometer from Ocean Optics [41] with temporal integration over discharge duration were done in order to develop the measurements of Bremsstrahlung radiation in the COMPASS tokamak.

The typical temporally integrated signal during the discharge duration measured by the minispectrometer in the COMPASS tokamak is presented in figure 2.2.1 (black) as an example. No spectral lines in the range of interest were found in similar signals measured during discharges with different parameters. On the base of known value of Bremsstrahlung radiation measured in other tokamaks we can say

that the present signal is the background. In our case it is the dark current of CCD detector of the minispectrometer used for the measurements. But it still cannot be excluded some parasitic plasma radiation hidden in the background. Maximum irradiance of such a parasitic immeasurable plasma radiation hidden in it can be set as a value of the background level 0.011 mW/(nm*cm^2).

Measured spectra showed that the sensitivity of the set-up with the minispectrometer is too low to be used for the spectroscopic measurement of Bremsstrahlung radiation in our tokamak, therefore the PMT-based system was chosen for the next stage of measurements.

On the base of experience of other tokamaks and according to our data of temporally integrated spectra over discharge duration the choice of the operational range was done in the line-free region next to 523 nm. The interference filter from Andover Corporation with transmittance above 76% at the central wavelength of 523.5 nm and bandwidth around 2 nm was chosen for the measurements [42]. The used detector is PMT from HAMAMATSU company of the type R5929 powered by the high voltage power supply C9525. Data collection system ATCA [43] is used for data collection with the temporal resolution of 2 MHz (0.5 μs).

It is possible to see in Figure 2.2.1 (red) the wavelength dependence of quantum efficiency (QE) of the PMT-based system for Bremsstrahlung radiation measurements, which was calculated as a product of transmittance of each optical component belonging to the system and quantum efficiency of the PMT.

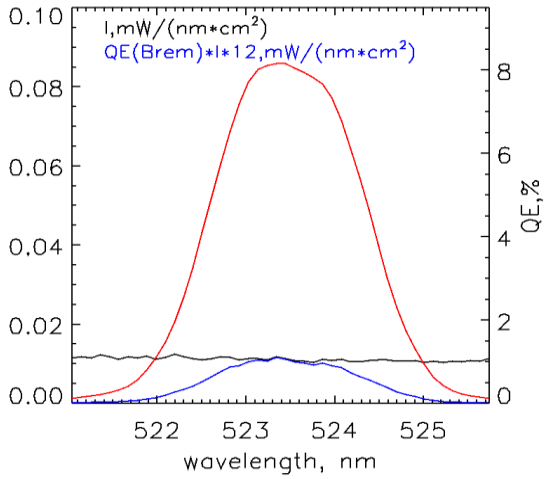

Figure 2.2.1. Wavelength dependence of quantum efficiency (QE) of PMT based system for Bremsstrahlung radiation measurements (red), temporally integrated signal during the discharge duration measured in the tokamak (black) and product of these two values (blue).

The received value represents the wavelength dependence of amount of detected radiation. It is the magnitude of designed system efficiency. It is possible to see that maximum 8% of the radiation can be registered by the system.

Wavelength dependence of the maximal influence of probable parasitic radiation to the resulting signal measured by PMT-based system can be estimated as a product of wavelength dependent PMT-based system quantum efficiency and signal measured by the minispectrometer in the range of interest. It is possible to see the values of this product in Figure 2.2.1 (blue curve). On the base of obtained curve we can conclude that maximal influence of parasitic radiation on the signals measured by PMT-based system higher than 1% can be expected in the range from 522 nm to 525 nm.

The calibration of the system was done according to procedure described in chapter 1.3. The set of calibration curves measured during the calibrations of the system is presented in Figure 1.3.3.

The calibration precision depends on the signal to noise ratio of the measured value of the calibration lamp radiation during calibration measurements. Therefore, imprecision approaches 50% for low input voltages and decreases to less than 10% in a linear part of the voltage dependence. The measurements of Bremsstrahlung were performed in the linear range, where the calibration imprecision is less than 10%.
The real Bremsstrahlung radiation of our plasma is calculated as product of measured Bremsstrahlung signal in volts at given input voltage and calibration constant corresponding to this input voltage in W/(m^2*V).

2.2.2. Calculation of Bremsstrahlung radiation of pure hydrogen plasma

The calculation is based on the formula [44]:

$$\Delta B_{calc} = -\frac{c}{\lambda^2} C_{calc} n_e^2 Z^2 \overline{G}_{ff} \left(\frac{X_H}{k_B T_e} \right)^{1/2} e^{-\frac{2\pi\hbar c}{k_B T_e \lambda}} \Delta V \Delta\lambda \Delta t \Delta\theta / L_{diag}^2 \quad (2.2.1)$$

for Bremsstrahlung radiation ΔB_{calc} radiating within the spectral range $[\lambda-\Delta\lambda/2, \lambda+\Delta\lambda/2]$ from a plasma element of the volume ΔV, at the time interval Δt, where:

$$C_{calc} = 1.06 \cdot 10^{-34}\, eV \cdot m$$
$$Z = 1$$
$$\overline{G}_{ff} = \frac{2 \cdot 3^{1/2}}{\pi} \qquad [45]$$
$$X_H = 13.595 eV$$
$$\hbar = 6.582 \cdot 10^{-16}\, eV \cdot \sec$$

$k_B T_e$ is electron temperature in eV, n_e is electron density, c light velocity, $\Delta\theta$ is spatial angle under which the volume element ΔV is observed by the diagnostic and L_{diag} is distance from the diagnostic input to the volume element.

The calculation of Bremsstrahlung radiation of pure hydrogen plasma requires knowledge of temporal evolution of electron temperature and density profile. Thomson scattering diagnostic (TS) provides necessary data for COMPASS tokamak discharges [46]. The most principal parameters of the TS system for this calculation are its spatial resolution (about 1 cm for the Central TS and about 0.5 cm for the Edge TS) and temporal resolution (about 17 ms).

TS measurements are provided for an upper half of COMPASS plasma along the vertical chord shown in Figure 2.2.2 (top half of the vessel plus 5 cm below the midplane).

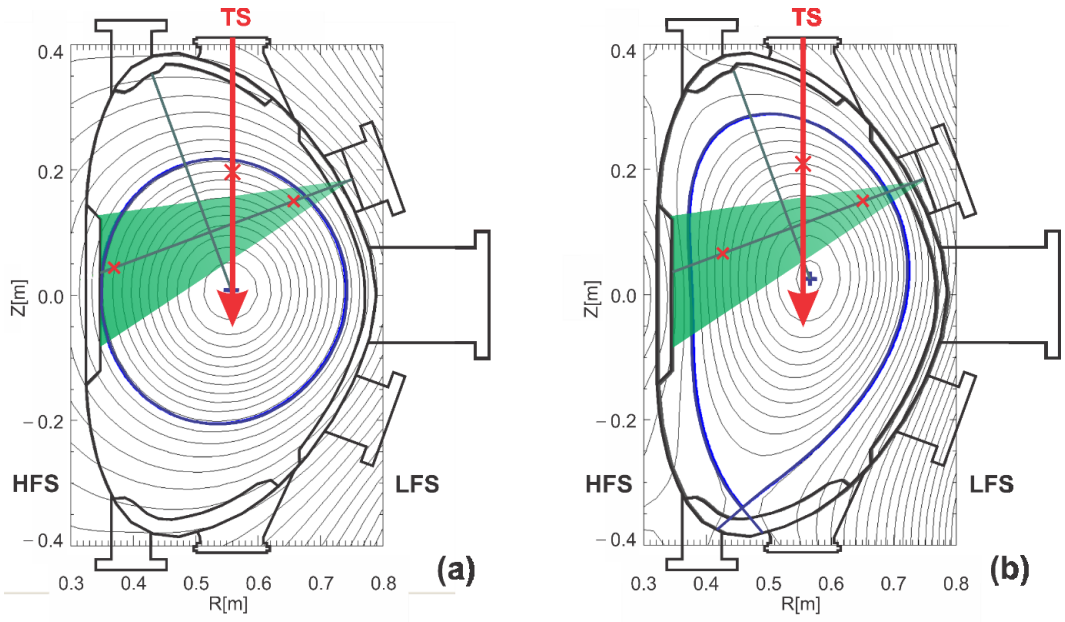

Figure 2.2.2. The EFIT reconstruction of magnetic surfaces for the circular and D-shaped plasmas of COMPASS. The Thomson scattering and PMT-based system geometry of measurements are indicated by the red arrow and the green area, respectively.

The plasma radiation is collected from a volume of the cone, whose axisymmetric cross section in the poloidal plane is shown in Figure 2.2.2 by the green colour.

The EFIT code [23] uses measurements of the magnetic diagnostic for reconstructions of the temporal evolution of magnetic surfaces during the discharge. The reconstruction result is shown in Figure 2.2.2. We use this code output in combination with our own IDL-based routine EFIT_2D_mapping for mapping of electron temperature and electron density measured by the Thomson scattering system to the point observed by the spectroscopic systems as it is shown at the figure 2.2.2 by the red crosses.

IDL, abbreviation for Interactive Data Language, is a programming language for data analysis. It is commonly used for processing of large massives of data including those related to image processing. The syntax includes many constructs from Fortran and some from C language. Since its creation in year 1977 it is widely used in many branches of physics especially in astrophysics.

EFIT is 2D code, so we need to simplify our observed volume to area shown in figure 2.2.2. After we use the obtained values for recalculation in toroidal direction.

EFIT_2D_mapping procedure is able to fit each point of array along the magnetic surface to which the point belongs. In our geometry we need to fit one value of Thomson scattering measurements to two points laying at the same magnetic surface. So to use the code we need to cut our chord to two pieces so that it will be only one fitting point corresponding to one magnetic surface.

In our device we have system of concentric magnetic surfaces with centre at plasma centre. The perpendicular line from the plasma centre to our chord will split it into two the same parts. Then the requirements for fitting using EFIT_2D_mapping will be fulfilled.

Let’s set coordinate of point from observation side as B(a3,b3), second end of the central line as A(a1,b1), top line as A’(a2,b2) and bottom one as A’’(a4,b4). The plasma centre is C(r0,z0). The perpendicular line to the line AB will cross it in the point D(x,y), the one to the A’B in D’(x’,y’) and the one to the A’’B in D’’(x’’,y’’).

Further calculation will be done for the point D(x,y). Let’s find the cross point using Pythagorean Theorem for triangle ADC and equation of line AB given by its true coordinates (see figure 2.2.3.).

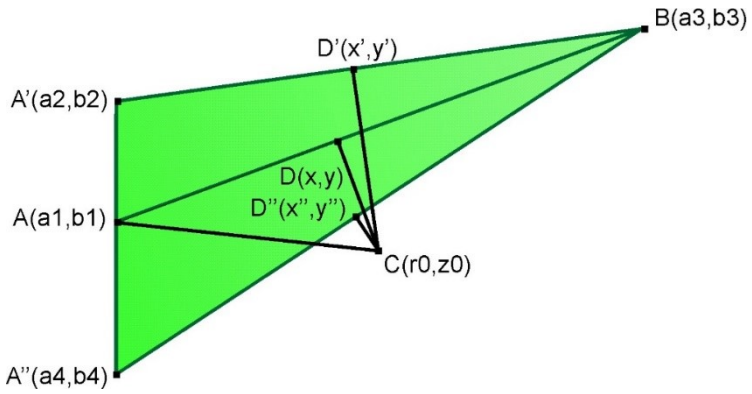

Figure 2.2.3. Geometry of chords splitting used for EFIT_2D_mapping procedure.

From line equation we get relation between coordinates:

$$x = ky - kb_1 + a_1$$

Where:

$$k = \frac{a_3 - a_1}{b_3 - b_1}$$

After inserting first formula to equation obtained from Pythagorean theorem we get for y:

$$y = \frac{-b + (b^2 - 4ac)^{1/2}}{2a}$$

Where:

$$a = k^2 + 1$$
$$b = -2k^2 b_1 + ka_1 - b_1 - r_0 k - z_0$$
$$c = z_0 b_1 - kb_1 a_1 + k^2 b_1^2 + r_0 k b_1$$

Coordinates of points D'(x',y') and D''(x'',y'') are found the same way.

The calculation allows to cut chords AB, A'B and A''B into two parts: so called LFS part (DB, D'B and D''B) and HFS part (AD, A'D' and A''D'') so that one point in input array will correspond to one point in resulting array. Let's take chord of measurements of TS diagnostic with position of measured points as input chord and arrays. Let's take in EFIT reconstruction result only that magnetic surface in which lay the points measured by TS. After fitting using the EFIT_2D_mapping procedure we get two arrays for T_e and n_e depending on the distance from diagnostic input given in [R,Z] coordinates for each of three curves discussed above. This gives to us the profiles of n_e and T_e at the chords of interest. Except the profiles along the

chords of interest the procedure will give also positions of points in all discussed magnetic surfaces with spatial resolution 1 cm.

Second stage of the estimation is calculation of Bremsstrahlung radiation of plasma element with electron temperature T_e and electron density n_e located at the distance GE from the diagnostic input (see Figure 2.2.4a).

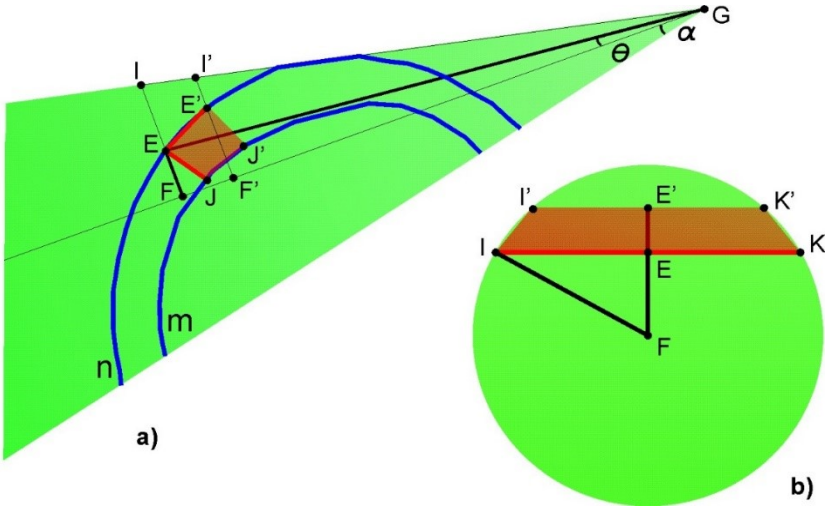

Figure 2.2.4. 3D geometry for our model: a) poloidal axisymmetric cross-section of observed volume, b) cross-section perpendicular to the one shown in Figure 4a along the segment EF.

Now we will discuss the geometry of the model in detail. The green colour in figure 2.2.4a is observed volume in poloidal and in 2.2.4b in toroidal directions. Two neighbouring magnetic surfaces are shown by blue colour. G is point of observation, 2α is observation angle. The observation angle is limited by numerical aperture of collecting optical fibre ($\sin\alpha=0.22$).

Distance EJ=E'J' is equal to TS spatial resolution for these points, distances EE' and JJ' are calculated as a distance between two neighbouring points given by coordinates with EE'≠JJ'. The distance is around 1 cm. So for central TS with resolution 1 cm the square shown in figure 2.2.3a by red colour is around 1 cm^2, for edge TS with resolution 0.5 cm, the shown square is around 0.5 cm^2.

GE is distance from the observation volume to the E point. GF is central axis of the volume from the input to the plane to which point E belongs. GI line limits the observation volume from the top.

Figure 2.2.4b shows the observation volume at the plane to which E point belongs. EF is distance from the central axis to the point E. IF is radius of observed

plane going through point E. IK is observation chord for the plane to which E point belongs. I'K' is observation chord for the plane to which E' point belongs. I'IKK' is observed plane of element volume in toroidal direction. We calculate it as an area of trapezium S with bases I'K' and IK and height EE'.

The volume of prism element is calculated as a product of area S and height EJ. This volume with electron temperature T_e and electron density n_e located in the distance GE from diagnostic input will be considered as an element of observed volume used in our formula.

Further summation of radiation of each element along the part of magnetic surface observed by our diagnostic will give value of plasma radiation of plasma layer with temperature T_e and density n_e. The distance of each such volume element from diagnostic input is known. The calculations will also give to us the value of the volume of plasma layer with T_e and n_e. It will allow making conclusion about influence of each plasma layer to measured result. Summation of plasma radiation of such layers limited by observation volume with different electron temperature and electron density will bring the value of Bremsstrahlung radiation of pure hydrogen plasma with given distribution of T_e and n_e measured from the volume of observation of our diagnostic.

The IDL code for Zeff calculation developed on the base of discussion given above is presented in the compact disc.

2.2.3. Typical result of Zeff estimation for real hydrogen plasma

The main parameters of the typical D-shaped discharge in hydrogen combined with optical diagnostic results are presented at Figure 2.2.5. The discharge has current flat top and stable plasma position.

It is possible to see from the formula 2.2.1 that the precision of the n_e measurement has a huge influence (quadratic dependence on n_e) to the precision of the Zeff calculation. Therefore, an imprecision of n_e measurements can be main source of Zeff estimation imprecision. The microwave interferometer gives a line-averaged value of electron density with a good temporal resolution of 5 μs along the same chord as TS. The TS diagnostic provides necessary local values of both electron density and temperature, which allows the values mapping in our measured volume but with a poor time resolution of 17 ms only. It is possible to see in figure 2.2.5c comparison of line-averaged values of electron density measured by

interferometer and calculated for the same chord using TS data. There is quite a good agreement (better than 85 %) between these two diagnostics during flattop but the TS gives lower values of electron density (typically 2-3 times) in circular part of discharge during ramp up and ramp down. Therefore, we expect that values of the calculated Bremsstrahlung radiation for pure hydrogen plasma presented in figure 2.2.5f can be underestimated at these discharge phases and as a result non-realistic values of Zeff will be received. The model of the calculation of Bremsstrahlung radiation for pure hydrogen plasma discussed above is well valid for quasi-steady-state conditions, which correspond to yellow area in figure 2.5.4.

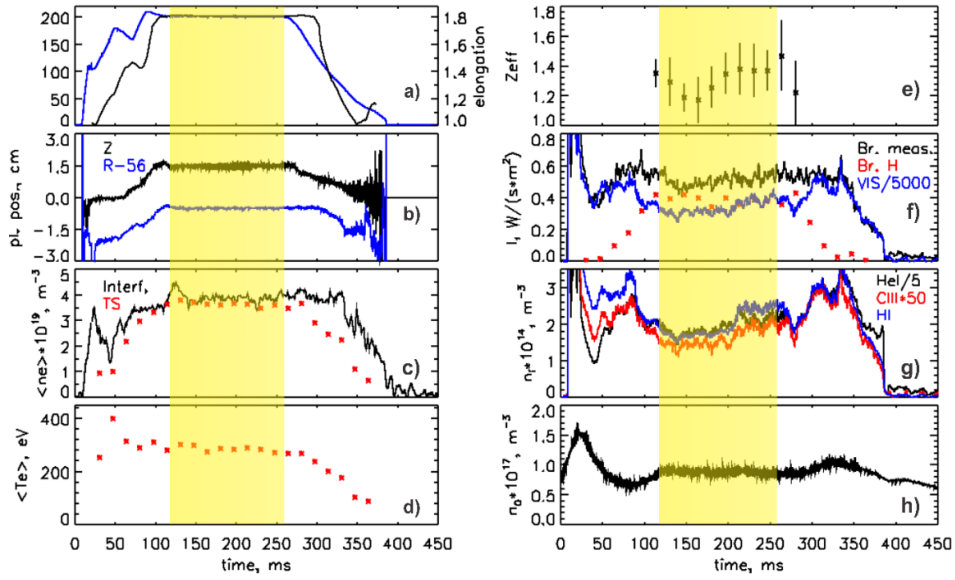

Figure 2.2.5. The main parameters of the typical D-shaped discharge #11144 combined with optical diagnostic results: a) plasma current (blue) and plasma elongation (black), b) horizontal (blue) and vertical (black) plasma position, c) electron density measured by interferometer (black) and Thomson scattering system (red), d) electron temperature measured by Thomson scattering system, e) Zeff, f) integral visible radiation (blue), Bremsstrahlung radiation measured by PMT-based system (black) and calculated for pure hydrogen plasma (red), g) CIII (red) ions, Hα (blue) and HeI (black) atoms density, h) density of gas (hydrogen) puffed to vacuum vessel during the discharge. Zero on the time axis corresponds to the breakdown of the discharge.

It is possible to see in figure 2.2.5e that Zeff grows during flat top and its behaviour repeats main plasma impurities density behaviour shown in figure 2.2.5g. The Zeff value is quite high and cannot be explained by high levels of presented impurities only.

2.2.4. Precision of Zeff estimation

It was mentioned above that the sensitivity of detector used in our minispectrometer is not enough to measure the Bremsstrahlung, but we used plasma spectra measured by the spectrometer in our tokamak plasma to choose the line-free region during the design of the PMT-based system. Therefore, we cannot guarantee, that some parasitic spectral lines with intensity comparable with or lower than the background signal of the spectrometer caused by so-called dark current of the detector do not exist. Let us discuss in details this problem and its probable influence to measured signal.

We prepared a list of spectral lines located in the spectral range of interest, i. e. [521.7:525.3] nm, which can influence our measurements, using the NIST database [25]. We considered a material of vacuum vessel (INCONEL 625), carbon plates, carborane used for boronization, atmospheric gases and helium as a working gas for glow discharges and hydrogen/deuterium as a working gas of regular discharges.

The spectral lines of the vacuum chamber material were detected in our discharges only during an extremely high plasma-wall interaction, when the covering of magnetic diagnostics was strongly deformed by magnetic field, and hence plasma directly hit it. All of these lines were more than one order weaker in irradiance in comparison with impurity lines like carbon and boron, which are regularly observed in our plasma. On the base of analysis of the spectra received in our tokamak in wavelength range 250-1100 nm [47], in such a discharges we found out that lines of Fe, Co and Ti can appear in the range of interest. The most intensive of them are lines of TiI (521.97 nm) and CoII (523.11 nm). However, the amount of these two elements in INCONEL 625 is very low (1% for Co and 0.4% for Ti). The QE of PMT based system for Bremsstrahlung radiation measurements is less than 1% at TiI wavelength but around 7.5% for CoII line.

Further analysis of our data shows that CIII spectral line around 524.47 nm must exist in our spectral range of interest in spite it has never been measured by our spectrometer, because one order more intensive (according to the NIST database) lines of the same transition $1s^2 2p(^2\mathrm{P}^\circ)3p$ to $1s^2 2p(^2\mathrm{P}^\circ)3s$ are regularly measured by our minispectrometers at wavelengths 432.57 nm and 466.59 nm. The temporal integration during discharge duration allows measuring the irradiance of these spectral lines just around 0.012 mW/cm^2, but perfectly distinguished from

background. Therefore, irradiance of CIII line around 524.47 nm can be expected as 0,001 mW/cm^2. The QE of the PMT-based system for Bremsstrahlung radiation measurements is around 4% at this wavelength. Therefore, the spectroscopic measurements at the 432.57 nm and 466.59 nm wavelengths should be done to control the influence of the line next to 524.47 nm to measured value of Bremsstrahlung radiation.

We also studied spectra discussed by other authors for other tokamaks for similar operational range like our one.

The work of A. Patel and his colleagues [48] is quite interesting for us; because the spectroscopic measurements using the device with much higher sensitivity was discussed for operational range around 517.3-524.3 nm. The spectrum given in the article shows four lines in our operational range. They are ClII (522.1 nm), CrI (522.7 nm), unknown spectral line next to 523.2 nm and CII (524.4 nm). The CrI line is the most intensive among them. We do not expect any chlorine in our tokamak, but we have around 20-23% of Cr in the vacuum vessel material and we use carbon plates as a wall protecting material. The unknown spectral line mentioned in article can be CoII (523.11 nm) line, which we expect also in our case. The QE of PMT based system for Bremsstrahlung radiation measurements is around 5.7% next to 522.7 nm, around 8% next to 523.2 nm and around 4.5% next to 524.4 nm. Therefore, possible existence of these three lines in our plasma cannot be neglected. In the work of A. Patel et al. the continuum level was measured as 2000 a.u. The impurities lines in our range of interest were less than 500 a.u. above the continuum. We can suppose similar situation in our tokamak. Therefore, the overestimation of Bremsstrahlung radiation is expected to be around 15% because of existence of CrI, CoII and CII lines in our operational range.

The work of A.V. Gorbunov and his colleagues [49] presented the spectroscopic measurements in our range of interest using detector with higher quantum sensitivity than we have. They measured few spectral lines in the range of interest. They are CrI doublet next to 521 nm and CIII line next to 524.47 nm. Presented results allow saying that in experimental conditions of tokamak T-10 the CIII line next to 524.47 nm has comparable intensity as CrI doublet next to 521 nm. Therefore, the CIII is expected to be dominant parasitic spectral line in our tokamak plasma in the operational range of PMT-based system for Bremsstrahlung radiation measurements.

A. Patel et al. [48] performed spatially resolved in poloidal direction measurements of plasma radiation. It was concluded that the highest influence of measured parasitic spectral lines to Bremsstrahlung radiation is expected for lower plasma density at SQL (scrape-off layer) and boundary plasma. Similar measurements are not possible in our tokamak because the quantum sensitivity of the spectrometers used in our tokamak is quite low. Therefore, a set of D-shaped discharges with the same parameters except plasma position, electron density and electron temperature was taken for studying of parasitic radiation influence to Zeff.

Figures 2.2.6 and 2.2.7 present dependence of main impurities amount, visible and Bremsstrahlung radiation and Zeff on electron density and temperature respectively. Each point of values presented at figures 2.2.6 and 2.2.7 is a result of averaging of the corresponding value during 150-200 ms of each from used discharge.

The toroidal current is heating the plasma through the resistance to the current caused by electron-ion collisions. Increasing of plasma density leads to decreasing of the energy received by electron between two collisions and therefore lower electron temperature will be reached.

It is possible to see in figure 2.2.6 that with increasing of electron density all chosen values, except Zeff, increase as well almost linearly. It is a result associated with decreasing of electron temperature and broadening of radiation shells of shown impurities.

All values shown in figure 2.2.7 except Zeff decrease with increasing of plasma temperature. It is known from theory that plasma with substantial amount of impurities has higher value of Zeff which increases the efficiency of ohmic heating and leads to higher temperature. This effect is possible to see in figure 2.2.7 and agreement of experiment and theory is very good in this case. On the other hand, presence of higher amount of impurities should lead to higher radiation loses. FLYCHK code expects narrowing of low ionized impurities radiation shells and their shift in direction to wall with increasing of plasma temperature. This fact can explain decrease of low ionized impurities amount and decrease of integral visible plasma radiation with increase of electron temperature.

It is also important to mention that Bremsstrahlung radiation for low density is one order lower than for high one. At the same moment CIII density differs only 5 times. This allows to suppose that influence of the parasitic CIII lines radiation to

measured Bremsstrahlung signal for low density plasma is not crucial if it takes place as was expected by A. Patel et al. [48].

One more point which can help to clarify the influence of parasitic spectral lines radiation to measured Bremsstrahlung radiation is dependence of spectral lines radiation on plasma position. It can be explained by observation of different parts of radiation shells for different plasma positions for used diagnostic configuration.

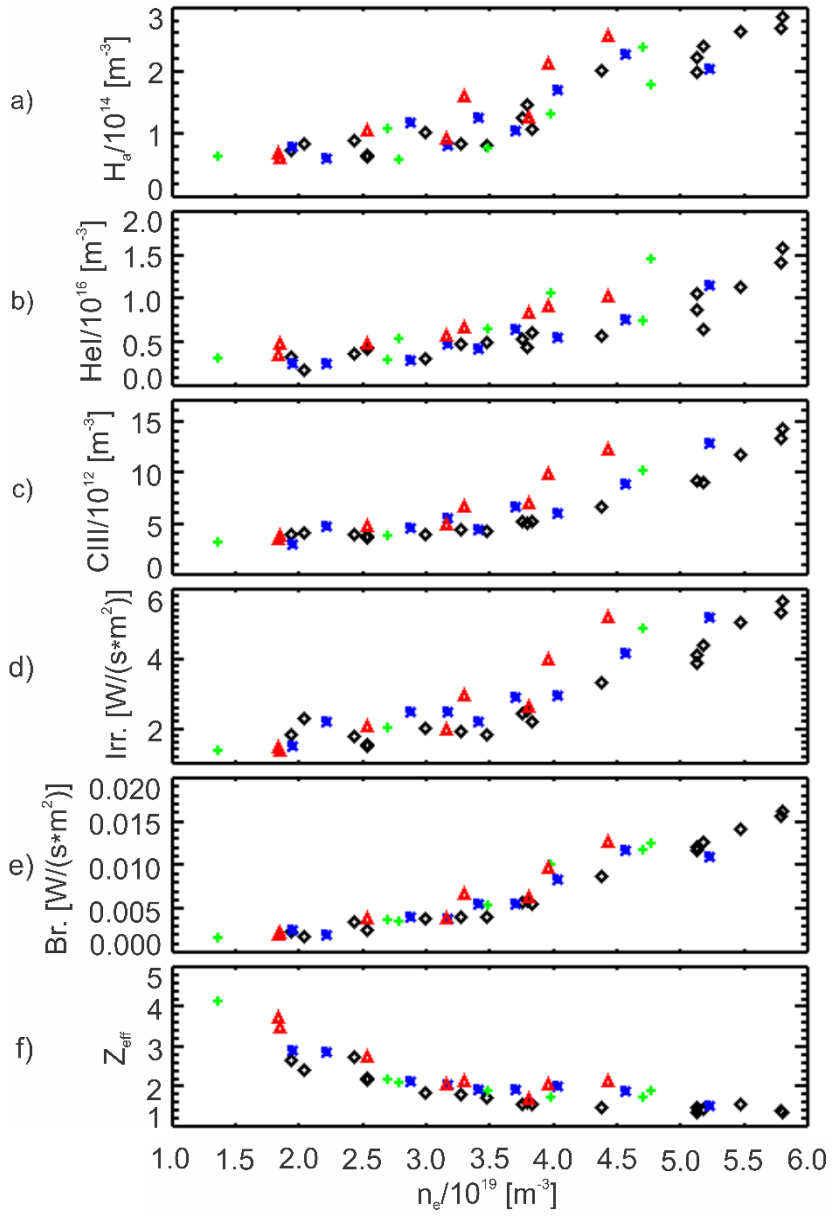

Figure 2.2.6. Dependence of a) neutral hydrogen density, b) neutral helium density, c) CIII ions density, d) integral visible plasma radiation, e) Bremsstrahlung radiation and f) Zeff on average plasma density.

Four different plasma positions are used in figures 2.2.6 and 2.2.7. Black points in both figures correspond to plasma with plasma centrum position at

0.565 mm in radial and 0.025 mm in vertical directions, green ones to 0.555 mm in radial and 0.025 mm in vertical directions, blue ones to 0.57 mm in radial and 0.01 mm in vertical directions and red ones to 0.555 mm in radial and 0.025 mm in vertical directions. Any clear dependence of shown plasma parameters on plasma position is not observed in these figures.

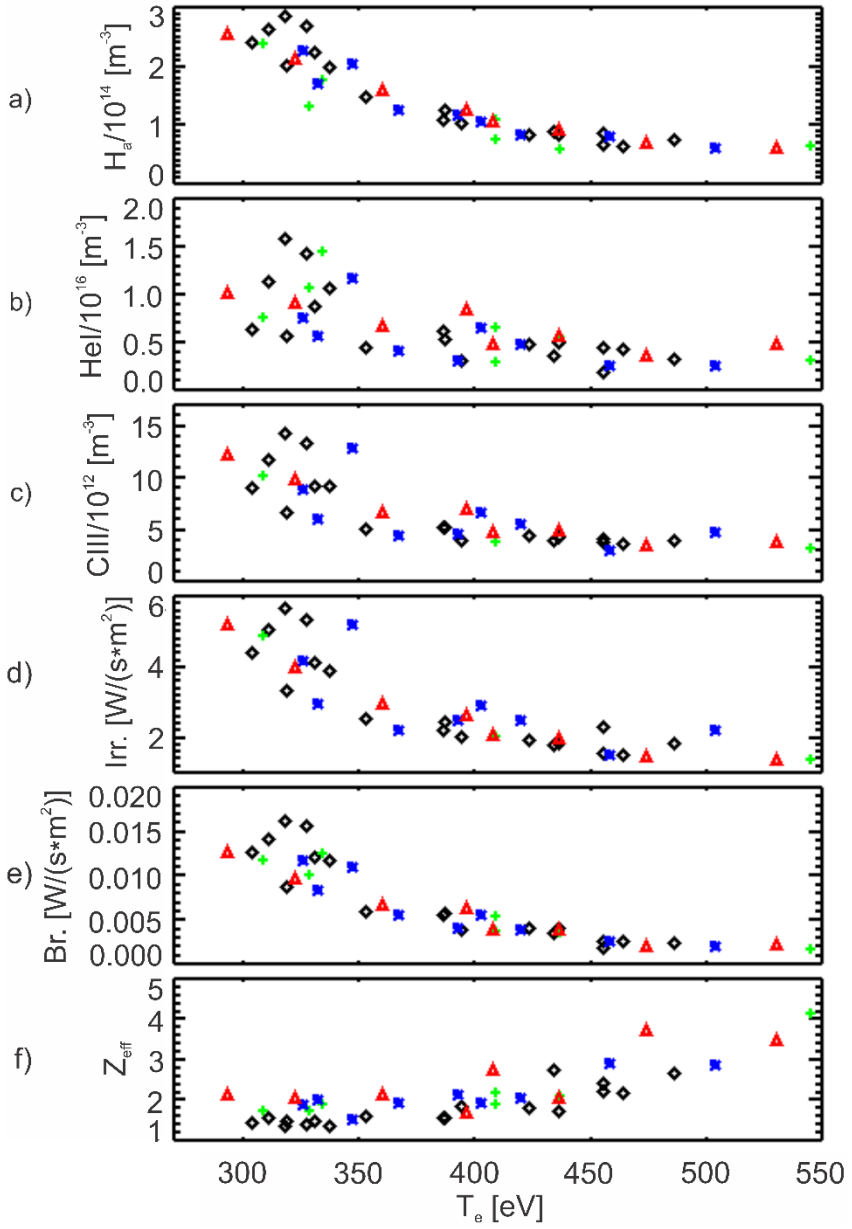

Figure 2.2.7. Dependence of a) neutral hydrogen temperature, b) neutral helium density, c) CIII ions density, d) integral visible plasma radiation, e) Bremsstrahlung radiation and f) Zeff on average plasma temperature.

Let us study the dependence of spectroscopic values on plasma position more properly. We take a set of D-shaped discharges with ohmic heating, similar plasma current, electron density and temperature and all available plasma positions. Few

discharges with different plasma positions belonging to the set mentioned above were chosen to show differences in plasma volume observed by visible diagnostic. Different plasma volume can be the main reason of differences in estimated values because of radiation shell effect discussed in part 2.1.2. Last closed magnetic surface and plasma centrum positions estimated using EFIT reconstruction at 164 ms of mentioned discharges presented in figure 2.2.8 visualize this difference. Confined volume of tokamak plasma is limited by last closed magnetic surface, therefore difference in observed confined plasma volume can get to 20%. Radiation shells of ions copy the shape of magnetic surfaces where they are located. In configuration of our diagnostic the observed part of the low ionized impurities radiation shells represents just planes of finite thickness shifted relatively to each other. Small shifts of plasma position available in our tokamak will lead to negligible changes in observed parts of radiation shells.

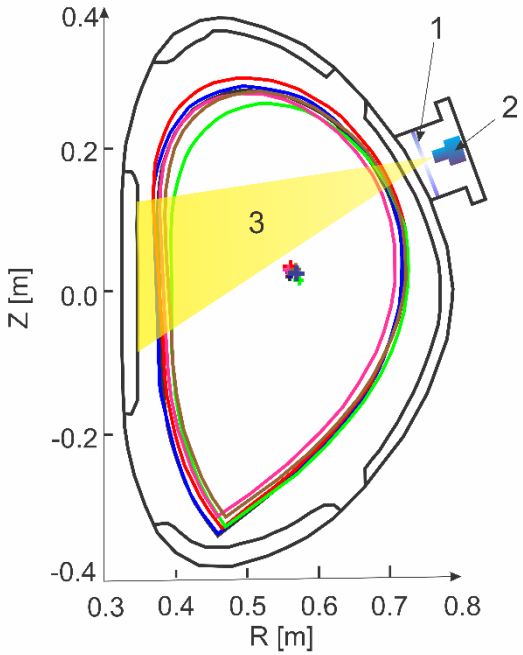

Figure 2.2.8. Demonstration of last closed magnetic surfaces and plasma centrums positions in vacuum vessel of COMPASS tokamak for discharges with predetermined different plasma positions. 1- vacuum window, 2- optical fibre entrance, 3- visible diagnostic observation volume poloidal cross section.

The results of dependence of available spectroscopic values on plasma position are present in figures 2.2.9 and 2.2.10. It is clear that there is no dependence of chosen spectroscopic values on plasma position in available range of plasma positions.

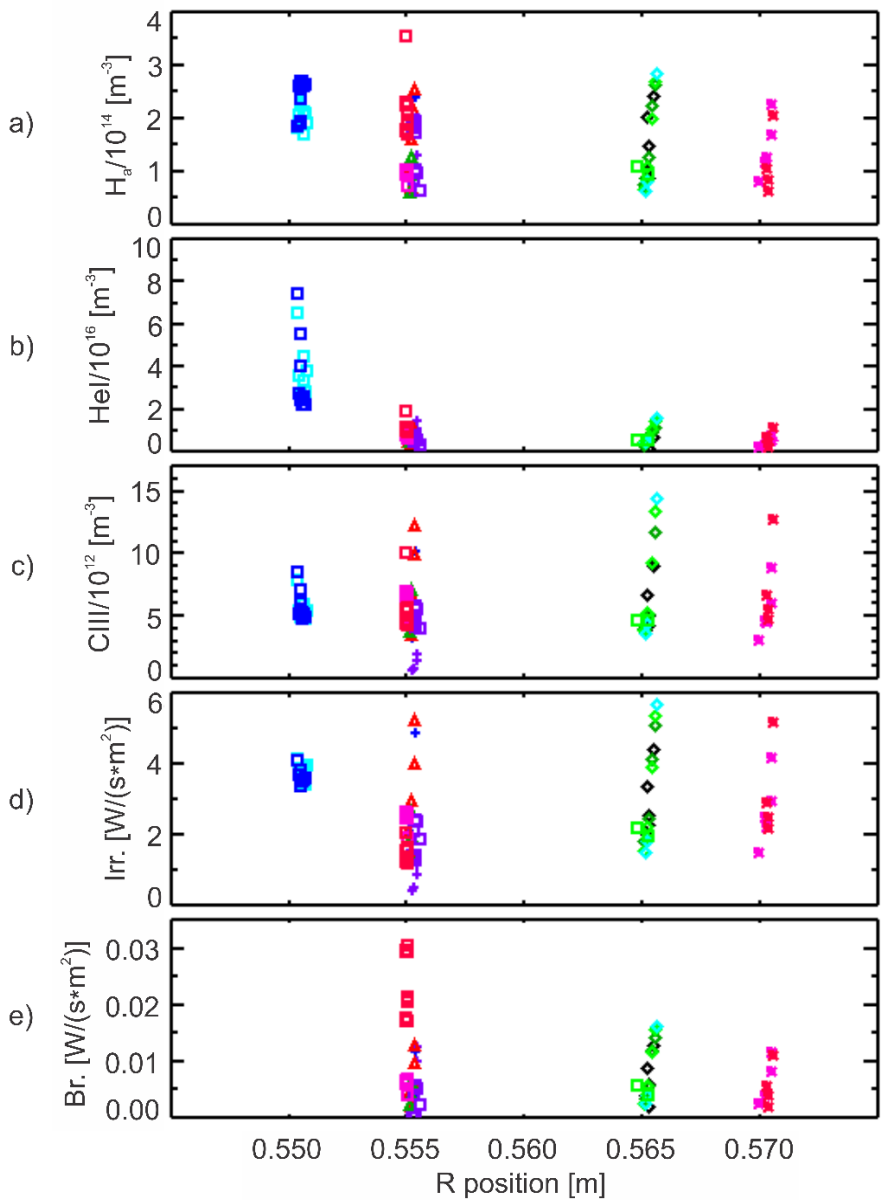

Figure 2.2.9. Dependence of a) neutral hydrogen density, b) neutral helium density, c) CIII ions density, d) integral visible plasma radiation and e) Bremsstrahlung radiation on radial plasma position. Distance is measured from main axis of tokamak.

There are unrealistically high Zeff values in figures 2.2.6 and 2.2.7 especially for low density plasma. One of possible reasons of abnormally high Zeff value in our plasma can be extremely high level of impurities for some discharge conditions. We studied evolution of plasma composition in operational regime discharges between two glow discharge procedures. D-shape discharges with plasma current around 190 kA and plasma density roughly $4 \cdot 10^{19}$ m^{-3} were taken for our investigation. The result is presented at figure 2.2.11. Each point in the graphs is an average during flat-

top duration value. Two yellow vertical lines mark moments when glow discharge procedure was done.

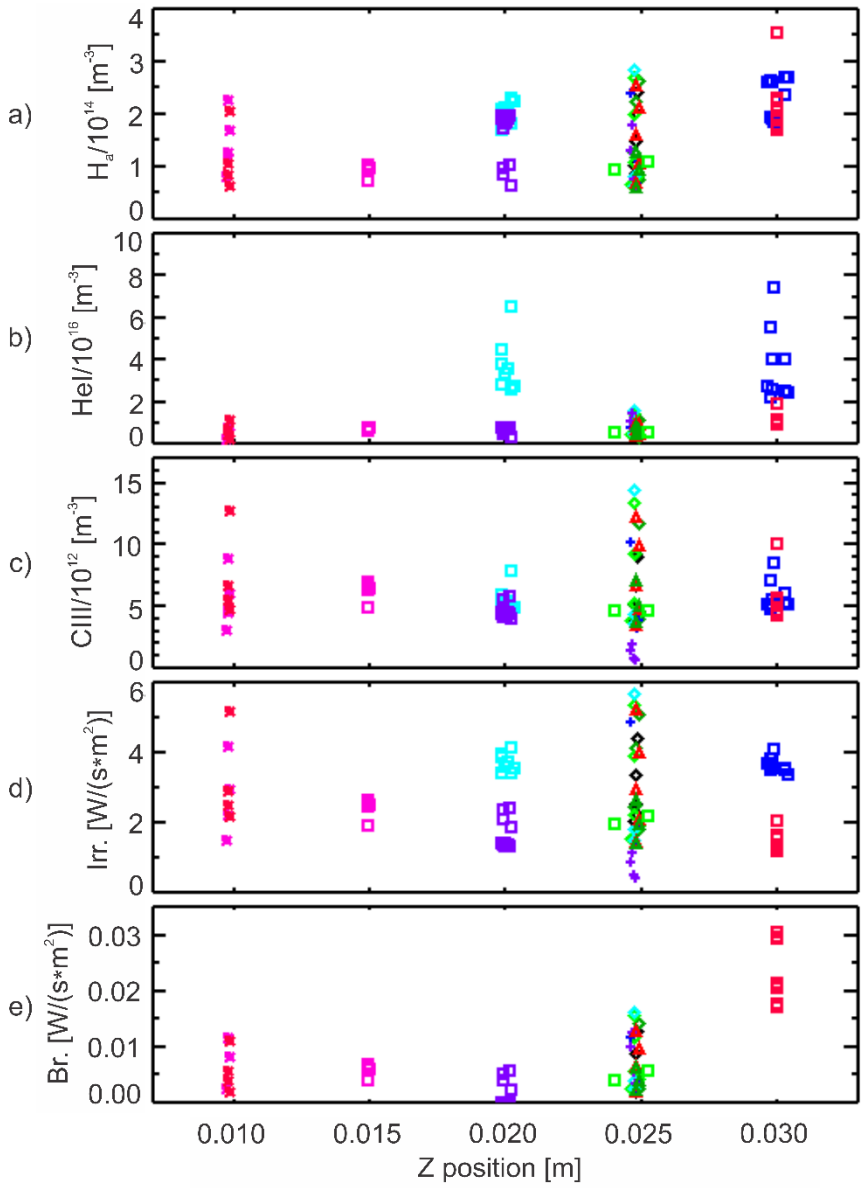

Figure 2.2.10. Dependence of a) neutral hydrogen density, b) neutral helium density, c) CIII ions density, d) integral visible plasma radiation and e) Bremsstrahlung radiation on vertical plasma position.

It is possible to see that amount of working gas which is necessary to puff into vacuum vessel to get plasma with roughly the same density continuously grows from discharge to discharge till it gets to approximately constant value in 6-7 discharges after the glow procedure. The resulting increase of gas puffing is two times. Neutral hydrogen repeats this behavior but resulting increase of neutral hydrogen radiation is only 1.7 times. Main plasma impurity in our tokamak is

helium. Its amount in plasma is maximal after the glow discharge procedure and then continuously decreases from discharge to discharge till the next glow procedure. The amount of neutral helium decreases 4 times. Other main plasma impurities (boron and carbon) have maximal value after the glow and decrease to roughly constant value in 6-7 discharges. The amount of CIII decreases two times and BII 1.25 times. Integral visible radiation has the same behavior as CIII and BII. It allows to suppose that all other impurities show similar behavior. The integral visible radiation decreases 1.2 times. Second glow discharge procedure turns back the impurities content.

The density of gas puffed to volume is $\sim 10^{17}$ m^{-3}. The neutral hydrogen is $\sim 10^{14}$ m^{-3}. It means that almost all puffed working gas is ionized.

The most intensive helium spectral lines in typical spectrum (see figure 2.1.1) in our tokamak are lines of He I (587.5 and 706.5 nm) and HeII (468.5 nm). The neutral helium influx from the wall in the first discharge after the glow discharge procedure is comparable with puffing of hydrogen to vacuum vessel. HeII spectral line has comparable transition probability as HeI one, so the amount of neutral and singly ionized helium in plasma should be comparable. It allows to suppose that first discharge after the glow is predominantly helium discharge.

CIII triplet (464.7, 465.0, and 465.1 nm) and CII doublet (457.8 and 458.3 nm) are the brightest carbon spectral lines in the whole observed spectrum. It means carbon amount should be proportional to the amount of these ions. The amount of CIII is only $\sim 10^{13}$ m^{-3}. The transition probability of CII in roughly twice lower than CIII, the lines are comparable in intensities. It means that total carbon amount is proportional to value twice higher than CIII amount. So, low amount of carbon in the discharges cannot cause unreasonably high Zeff values.

The brightest lines of boron are BIV (282.2, 282.4 and 282.6 nm), BII (345.1 nm) and BIII (783.5 and 784.1 nm). The intensities of BII and BIV lines are comparable in measured spectrum, but we know nothing about irradiance of BIV line because our calibration source has too low radiation in corresponding range and is not able to give reasonable calibration constant for BIV spectral line. However, BII and BIV lines have comparable transition probability. Therefore, we can suppose that lines of these ions have comparable irradiance. BIII lines are at least two times less intensive than BII and BIV and have twice lower transition probability. All these

facts allow to suppose similar amount of BII and BIV ions and twice lower BIII amount. The BII amount is ~10^{16} m^{-3}. It means total amount of boron in different ionization stages in the discharge can be 2.5 times higher.

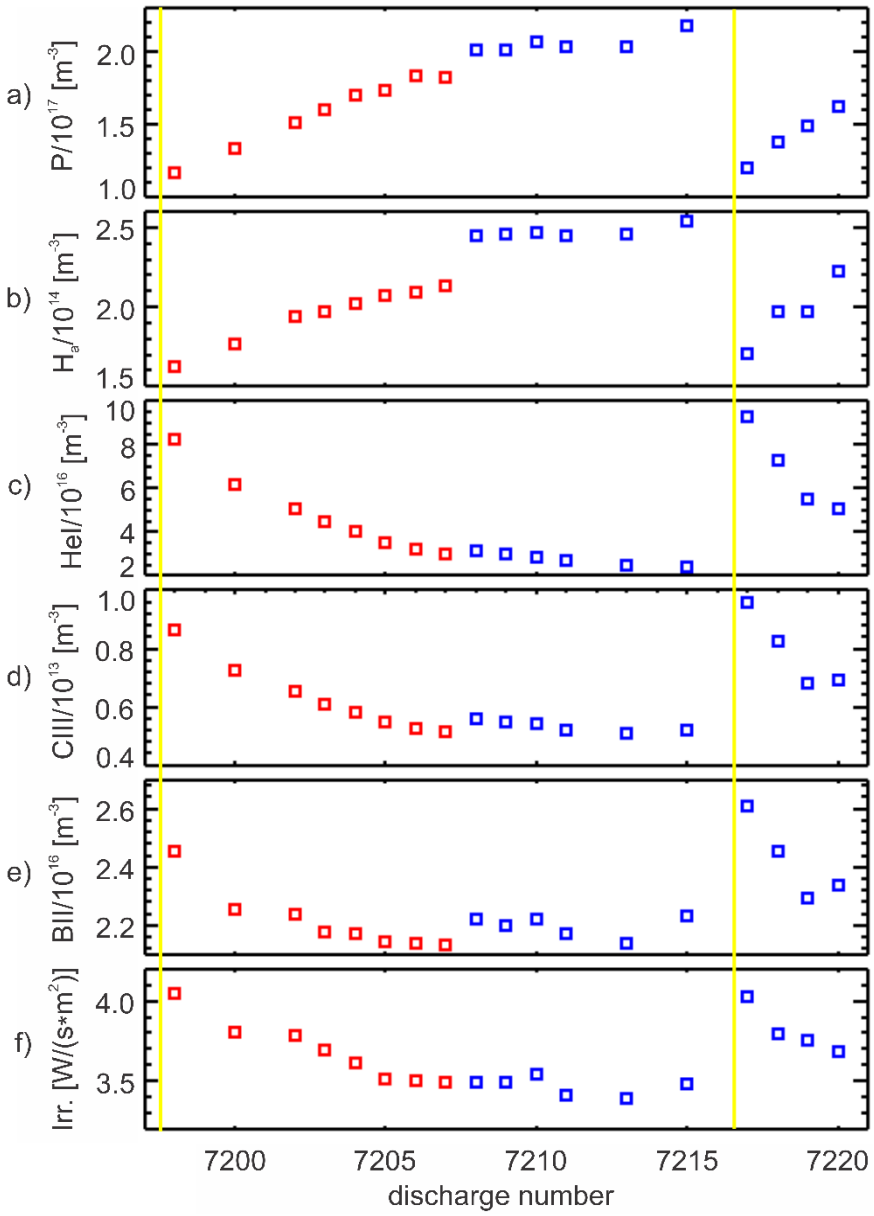

Figure 2.2.11. Evolution of a) density of gas (hydrogen) puffed to vacuum vessel during the discharge, b) Hα and c) HeI atoms density, d) CIII and e) BII ions densities, f) integral visible plasma radiation during operational regime from discharge to discharge between two helium glow discharge procedures. Red squares correspond to plasma centrum position 0.02 m in vertical direction and 0.55 m in horizontal one. Blue squares correspond to plasma centrum position 0.03 m in vertical direction and 0.55 m horizontal one.

It means that in the first discharge after the glow discharge procedure amounts of hydrogen, helium and boron in the discharge are comparable. In these

conditions the Zeff can get to value higher than 2. The helium amount decreases 4 times after 13 discharges. It leads to one order difference between amount of neutral hydrogen puffed to vacuum vessel and neutral helium desorbed from wall to it. Boron amount decreases only 1.25 times and thus boron becomes the main impurity in such discharges. It leads to more reasonable but still high value of Zeff as presented in figure 2.2.5. It is possible to see in figure 2.2.6 that the calculated value of Zeff corresponds to expected one.

More proper studying of the most intensive spectral lines of all main impurities using PMT based systems is necessary to estimate possible plasma composition of low density plasma. The influence of parasitic spectral lines to Zeff in discharges with low density is still not clear and additional spectroscopic measurements in operational range of PMT based system for Bremsstrahlung radiation measurement with spectrometer with high enough quantum sensitivity should be done to clarify this influence.

2.3. Visible spectroscopy at the Neutral Beam Injection on the COMPASS tokamak

The basic heating in tokamaks is Ohmic heating P_{OH} caused by inductively driven toroidal current I_{plasma} in resistive plasma loop R_{plasma}

$$P_{OH} = I_{plasma} * R_{plasma}.$$

However, with increasing electron temperature the plasma resistivity decrease as $R_{plasma} \sim T_e^{-3/2}$, and efficiency of the Ohmic heating decreases. Typical electron temperatures, which can be achieved in currently operational tokamaks are in the range of several kiloelectronvolts. Therefore, to get temperatures required for ignition (~100 keV), it is necessary to apply some additional heating. High power neutral beam injection is one of the methods of such additional heating [24]. The COMPASS tokamak is equipped by two Neutral Beam Injectors (NBI) for such purpose.

2.3.1. Neutral Beam Injector on the COMPASS tokamak

Scheme of NBI is shown in Figure 2.3.1.

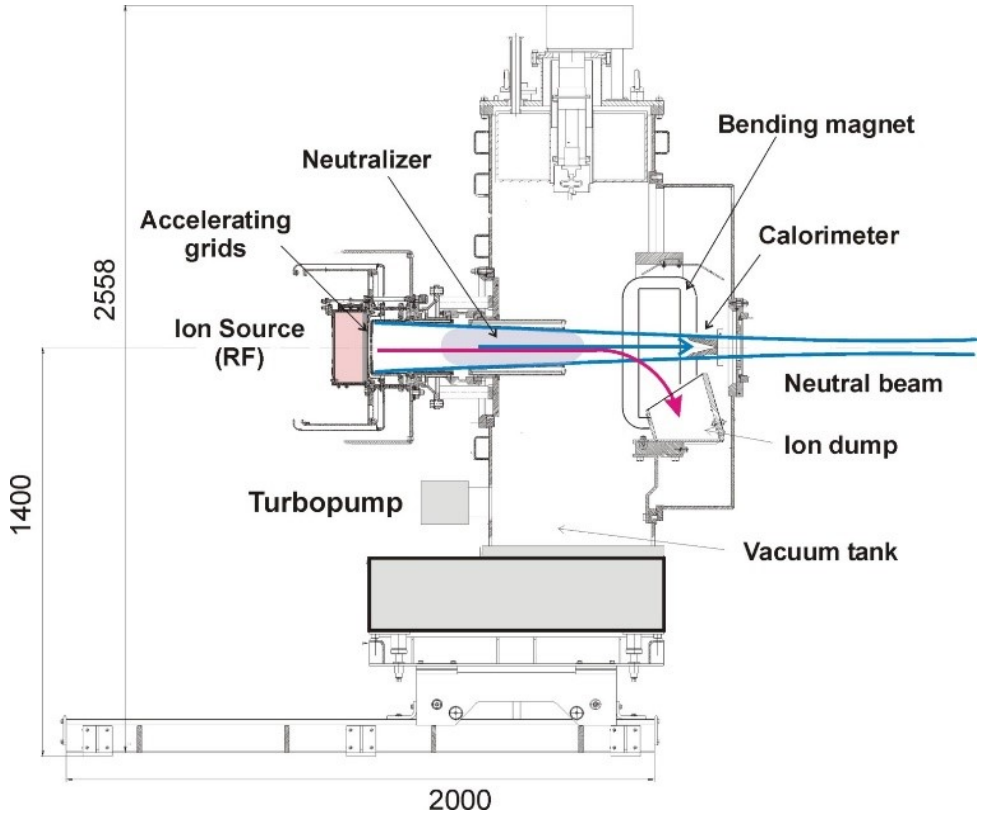

Figure 2.3.1. Engineering scheme of NBI on the COMPASS tokamak.

The neutral beam injector of COMPASS tokamak is described in detail in [50]. It consists of the radio frequency (RF) ion source where the ions are extracted from RF plasma by a system of bended grids, which accelerate ions to 40 keV and focus them into a beam. The ion current I_{NBI} is measured, being typically in the range of 6-12 Amp. Then, the ion beam is neutralized in the neutralizer filled by molecular Deuterium by charge exchange collisions. The efficiency of neutralization is 0.8 for the 40 keV deuterium ions. Consequently, the neutral beam power P_{NBI} at the output of NBI is:

$$P_{NBI}[kW] = 40 * 0.8 * I_{NBI}[A],$$

which is in the range ~190 - 400 kW for one NBI.

Consequently, the total additional power delivered to plasma by both NBIs is up to 800 kW. However, the ion current extracted from the RF ion source is not composed only from deuterons D^+, but also from molecular ions D^+_2 and D^+_3. The molecular ions are neutralized by dissociative collisions inside the neutralizer. Consequently, the resulting neutral beam contains deuterium atoms with energy:

- E = 40 keV (from D^+),

- E/2 = 20 keV (from dissociation of D^+_2),
- E/3 = 13.3 keV (from dissociation of D^+_3).

Beam composition is experimental studied in [51]. It is shown that fast neutral beam with fractional energy components delivers roughly the same power to plasma as the mono-energetic beam, because the number of fast neutrals of E/2 and E/3 components is two and three times higher. However, the power of the low energy fractions is deposited closer to the beginning of the beam trajectory, i.e. at the plasma edge.

2.3.2. Main channels of power losses at Neutral Beam Injection.

The heating beam is injected to the plasma tangentially at COMPASS as shown in Figure 2.3.2.

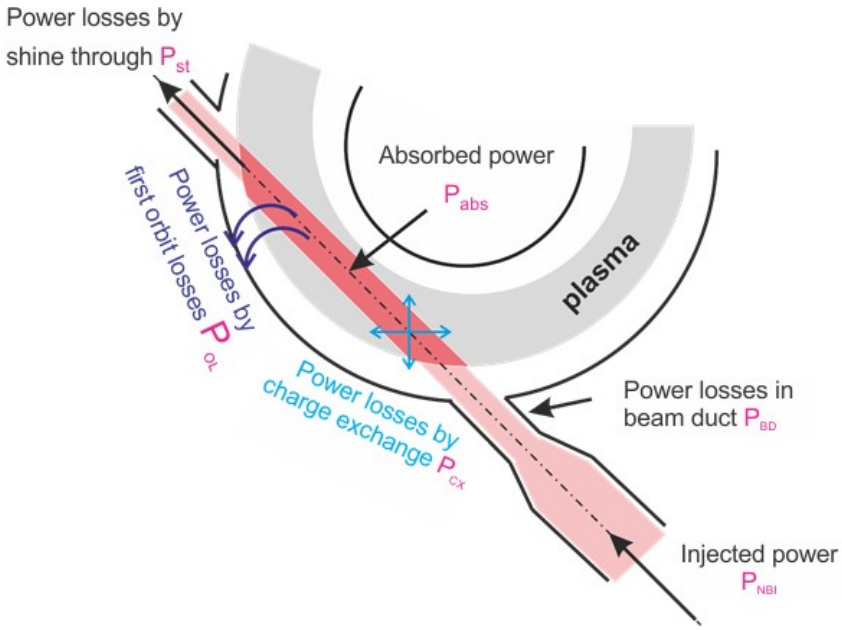

Figure 2.3.2. Schematic picture showing dominant power losses of the neutral beam injected tangentially to tokamak plasma.

Fast neutral atoms injected to the plasma become ionized by means of collisions with plasma particles by charge exchange (cross section σ_{ex}), ionization by ions (cross section σ^+_{ion}) and ionization by electrons (cross section σ^-_{ion}). Resulting fast ions collide with plasma particles and transfer their kinetic energy via Coulomb collisions, and plasma heating occurs. However, the injected NBI power P_{NBI} does not contribute fully to plasma heating since a fraction of it is lost without any impact to tokamak plasma. Individual channels of power losses are briefly described below.

2.3.2.1. Power losses in the beam duct, P_{BD}

The diameter of the neutral beam at the focus, located at the entrance port of the tokamak vessel depends on the extracted ion current. The optimum focusing of the deuterium beam is achieved for extracted currents 10-12 Amps, when the beam diameter is ~ 5 cm smaller than the entrance port of the vessel. At lower current, the diameter of the beam is comparable with the diameter of the entrance port, and a fraction of the beam power P_{BD} is lost in the beam duct and does not penetrate into plasma.

2.3.2.2. Power losses by shine through, P_{ST}

A fraction of the neutral beam remains un-ionized along its trajectory in plasma and hits the opposite wall of the vessel. This effect depends predominantly on the plasma density. The total cross section for ionization is:

$$\sigma_{tot} = \sigma_{ex} + \sigma_{ion}^{+} + \sigma_{ion}^{-},$$

Therefore, the mean free path of fast neutral atoms λ_{ion} is:

$$\lambda_{ion} = \frac{1}{\sigma_{tot} * n_e}.$$

The total ionization cross section for 40 keV deuterium beam is $\sigma_{tot} = 9*10^{-20}$ m^2. The shine through losses become negligible for plasma densities $n_e > 5\ 10^{19}$ m^{-3} (the length of the beam trajectory on COMPASS is L ~ 1 m).

2.3.2.3. Orbit losses, P_{OL}

The fast ion resulting from the ionization collision is captured on so called banana trajectory and escapes plasma across the separatrix without any energy transfer to plasma particles. These “orbit loosed” particles bombard the first wall of the tokamak vessel and may enhance flux of atoms of working gas or impurities adsorbed at the first wall elements into the plasma.

2.3.2.4. Charge exchange losses

After being ionized, the beam particle can collide a neutral atom in plasma by the charge exchange collision. Resulting fast atom may escape plasma with some probability without delivering any energy to plasma. This power loss channel takes place at the plasma edge, where the density of plasma neutrals is still sufficiently

high. Again, particles lost by this channel might increase influx of impurities to the plasma as in the previous case.

The numerical simulations have been performed to estimate the power losses on COMPASS by using ASTRA-FAFNER code [52]. The table shows result for plasma characterized by B_t = 1.2 T, I_p = 200 kA, $\langle n \rangle = 4.0*10^{19}$ m^{-3}

- Shine Through losses 7%
- Orbit losses 11%
- Charge exchange losses 5%

Moreover, numerical simulations provide an estimate of fraction of NBI power delivered to electron and ion components:

- Power to ions 56%
- Power to electrons 21%

In this part of thesis, we characterize the NBI heated plasma by absolutely calibrated spectroscopic diagnostics, which were described in details in previous parts of the thesis.

2.3.3. Behaviour of impurities at a medium density discharge with NBI heating

Figure 2.3.3 shows evolution of the discharge #11035 with the NBI heating executed at the line average density $3.5 \cdot 10^{19}$ m^{-3}. Evolutions of selected macroscopic plasma parameters are shown in the left column, while results of spectroscopic measurements are plotted in the right column.

The plasma current is kept constant at 180 kA during the quasi-stationary phase of the discharge. The NBI pulse is marked by the yellow bar. It starts at t = 140 ms and its duration is 90 ms. The extracted ion current is 12 A, which corresponds to the NBI power of 380 kW at the output of the injector. A noticeable plasma heating is observed. The total plasma energy calculated from the EFIT reconstruction increase by ~35%. The line average density remains unchanged during NBI and the average electron temperature increases just slightly. This implies that the total energy increases mainly due to the ion heating.

Two of the dominant impurities (Helium and Carbon) are commonly measured during COMPASS tokamak operation. They are demonstrated in the panel *g*) of figure 2.3.3. During the discharge, the Carbon atoms are sputtered from the graphite tiles, which cover a part of the tokamak vessel exposed to highest heat fluxes – the divertor and the central belt limiter regions. The brightest carbon lines in

the spectrum, which belongs to CIII triplet with λ ~ 465 nm, is used to estimate the carbon content. The helium is used on COMPASS as working gas for cleaning glow discharge, which is performed in between every tokamak discharge to desorb impurity molecules from first wall elements, and improve reproducibility of plasma performance. A fraction of Helium atoms is implanted into the graphite tiles during this cleaning procedure. During the tokamak discharge, helium atoms are desorbed and flow into plasma.

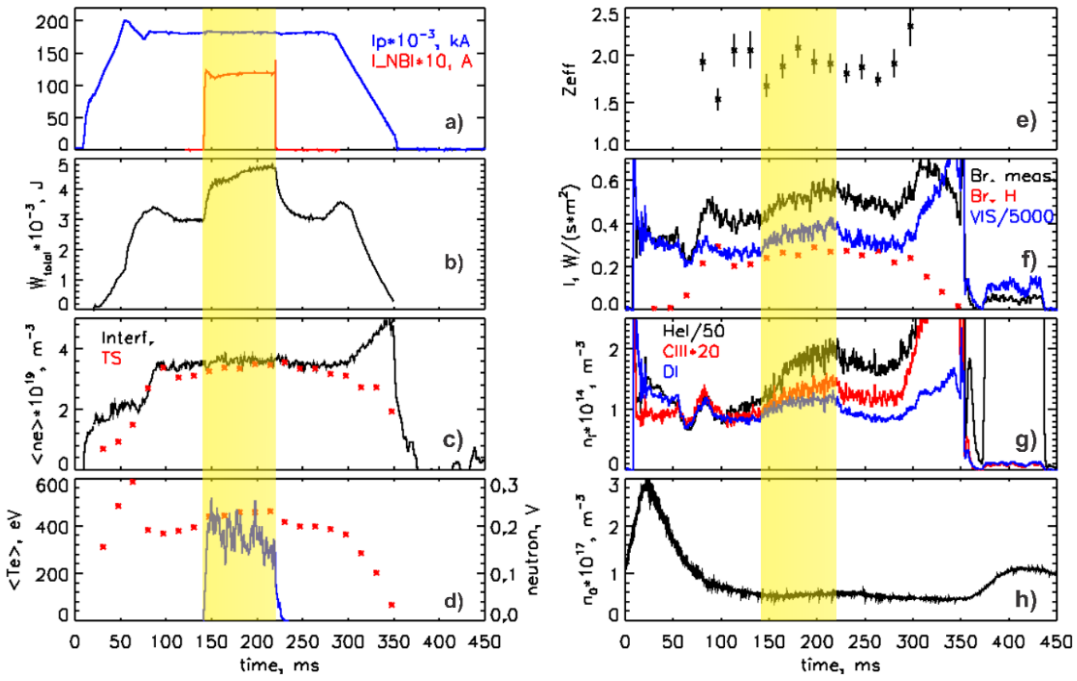

Figure 2.3.3. Temporal evolution of the discharge #11035 characterized by a medium plasma density. a) plasma current (blue), the NBI current (red), b) total plasma energy from EFIT reconstruction, c) line average electron density measured by interferometer (black) and calculated from the Thomson scattering (TS) (red), d) average electron temperature from TS (red) and the neutron flux (blue), e) effective ion charge (Z_{eff}), f) integral visible radiation (blue), measured (black) and calculated for pure deuterium plasma using TS data (red) Bremsstrahlung radiation, g) density of Helium (black) and Deuterium (blue) atoms and CIII ions (red), h) density of Deuterium gas puffed to vacuum chamber to keep plasma density at a prescribed level.

The densities of the mention main impurities (Helium and Carbon) increase during NBI as seen in the panel g) in Figure 2.3.3. The both impurities increase at the beginning of the NBI pulse and their densities saturate at 10^{16} m^{-3} for Helium and at $7.5 \cdot 10^{12}$ m^{-3} for Carbon correspondingly. After switching of the beam, the impurity

densities decay to a bit higher level than before NBI. This level is by 14% higher for CIII and 35% for HeI than before injection. A characteristic time constant ~30 ms of the decay is comparable with the particle confinement time on COMPASS.

The integral visible radiation is integration of all spectral lines in the operational range of diagnostic including different impurities lines. It shows behaviour similar with deuterium during injection. During 30 ms after injection it decreases to some constant level which is almost the same as it was before injection. It means that total increasing of all plasma impurities caused by injection is significant only during NBI.

2.3.4. Behaviour of impurities at a low density discharge with NBI heating.

Figure 2.3.4 shows the temporal evolution of discharge #11038 characterized by a low plasma density. The remaining discharge parameters are identical with those mentioned in the previous paragraph.

The average electron density increases linearly during NBI from 1.5 to $3.5 \cdot 10^{19}$ m^{-3}. The plasma energy increases by a factor of two, while the electron temperature remains roughly the same during NBI. It might imply that the increase of the plasma energy is only due to the increase of the plasma density. However, an ion heating is also observed in low density discharges [53].

The temporal evolutions of spectroscopic signals are different from those shown in the previous paragraph for medium densities. All signals (HeI, CIII, integral visible plasma radiation and Z_{eff}) increase during NBI and do not saturate. Furthermore, note an abrupt drop of those signals immediately after switching of the NBI pulse. A possible explanation is that a significant part of the neutral beam passes through the plasma at such low densities. The neutral beam interacts the opposite part of the compass vessel (the beam dump) and create a localized source of impurity atoms and molecules adsorbed on the first wall elements in this region. Therefore, experimental observations of impurities at low density discharges are consistent with "shine through" effect discussed above.

An increase of neutral deuterium signal during NBI is roughly the same as during the medium density discharge. This is probably result of fuelling of plasma by the neutral beam. The injection leads to roughly to $4 \cdot 10^{13}$ m^{-3} of fast atoms income to plasma.

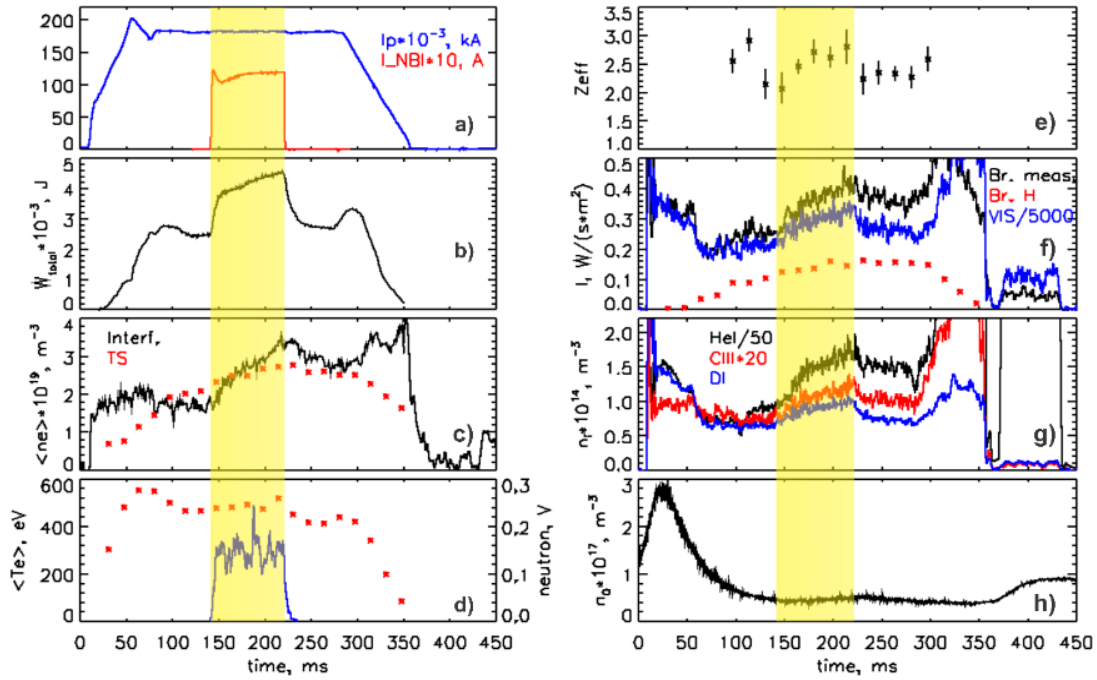

Figure 2.3.4. Temporal evolution of the discharge #11038 characterized by a low plasma density. a) plasma current (blue), the NBI current (red), b) total plasma energy from EFIT reconstruction, c) line average electron density measured by interferometer (black) and calculated from the Thomson scattering (TS) (red), d) average electron temperature from TS (red) and the neutron flux (blue), e) effective ion charge (Z_{eff}), f) integral visible radiation (blue), measured (black) and calculated for pure deuterium plasma using TS data (red) Bremsstrahlung radiation, g) density of Helium (black) and Deuterium (blue) atoms and CIII ions (red), h) density of Deuterium gas puffed to vacuum chamber to keep plasma density at a prescribed level.

2.3.5. Impact of the plasma position on impurity content.

To assess impact of the position of the centre of the plasma column on the NBI efficiency and on the impurity content, several discharges with the same plasma current (180 kA) and the same NBI power (I_{NBI} = 10 A), but differing in coordinates of the position of the centre of the plasma column with respect to the centre of the tokamak vessel are selected as shown in the following table.

#	Vertical displacement [m]	Horizontal displacement [m]
11030	0.025	0.565
11066	0.025	0.555
11085	0.01	0.570

Table 4. Position of the centre of the plasma column for chosen discharges.

Comparison of discharges #11030 and #11066 differing in horizontal displacement by is plotted in figure 2.3.5.

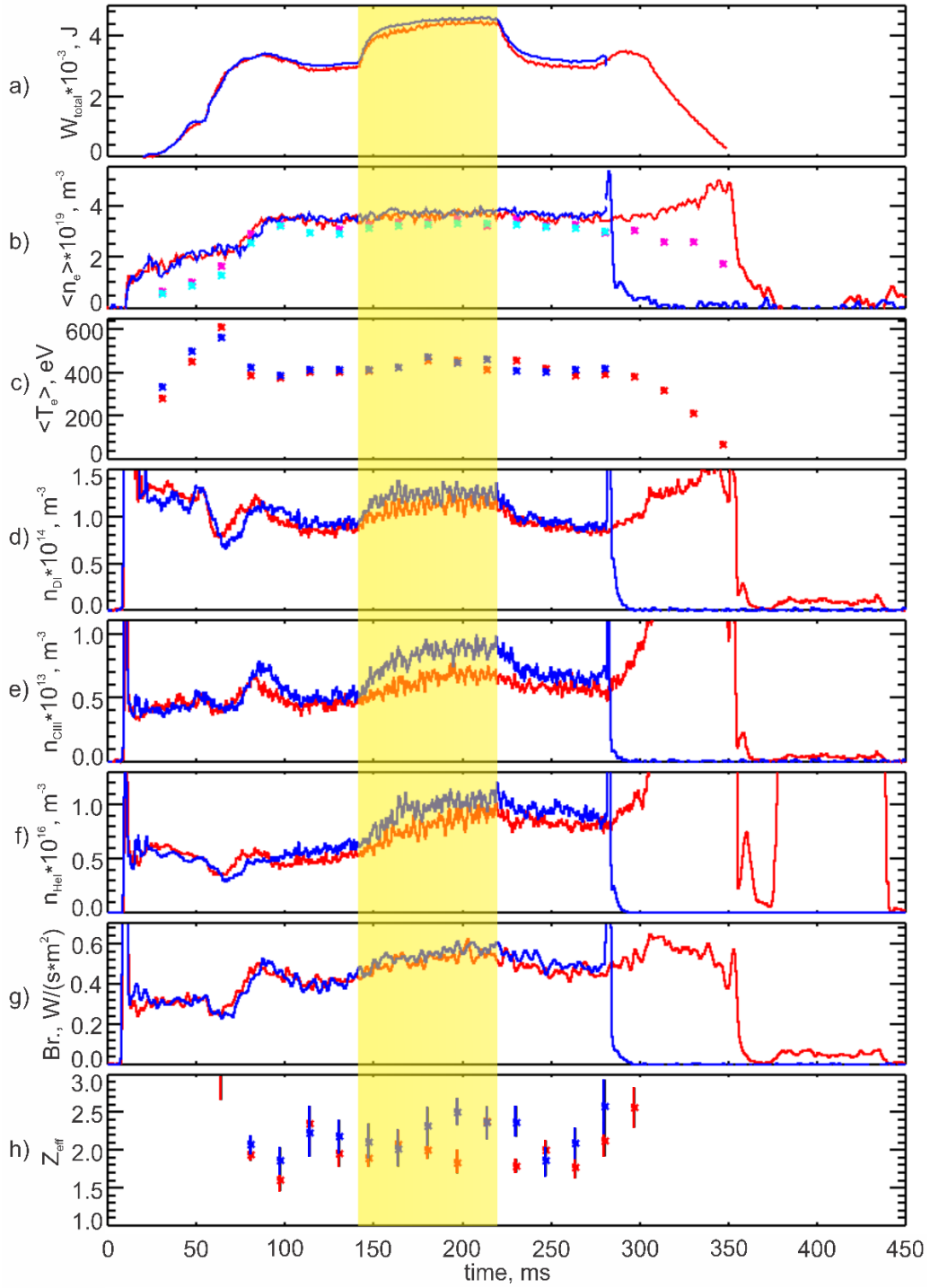

Figure 2.3.5. Temporal evolution of discharges #11030 – red/pink traces (plasma position 1) and #11066 –blue/azure traces (plasma position 2) a) total plasma energy from EFIT reconstruction, b) line average electron density measured by interferometer (solid lines) and calculated from the Thomson scattering (symbols), c) average electron temperature from TS; density of d) Deuterium atoms, e) CIII ions, f) Helium atoms, g) measured Bremsstrahlung radiation, h) effective ion charge.

It is evident that the main macroscopic plasma parameters, such as the total plasma energy, the line average density and the average electron temperature remain unchanged, when the centre of the plasma is displaced by 10 mm toward the high field side of the torus. The observed difference is seen only in spectroscopy data. The density of CIII increases from $6 \cdot 10^{12}$ m^{-3} to $9 \cdot 10^{12}$ m^{-3} during NBI when plasma is shifted inwards. A slight increase of Helium density is observed as well. The effective ion charge Zeff increases noticeably during NBI for shifted plasma. But, surprisingly the Bremsstrahlung emission remains the same for both plasma positions. The reason for this behaviour remains still unclear, and has to be analysed later in more detail.

The discharge #11066 ends with disruption, which might be result of a stronger interaction of plasma with the central column of the tokamak vessel. Note also a strong emission at HeI spectral line after termination of the discharge #11030 after $t > 370$ ms. This phenomenon is frequently observed on COMPASS and interpreted as an "afterglow plasma" confined in the toroidal magnetic field at almost negligible plasma current, which has an opposite orientation than during the regular discharge. This plasma burns in Helium working gas desorbed from first wall elements.

Figure 2.3.6 shows the temporal evolution of the discharge # 11085 characterized by a downward shift of the plasma column by 15 mm. It is possible to see that all parameters of this discharge before NBI are roughly the same as in previous cases. The significant difference appears at 15 ms after the start of NBI, when the transition to the mode with improved plasma (H mode) occurs [54]. At this moment, the transport barrier is formed as a narrow region at the plasma edge in proximity of the separatrix. The transition is manifested by a sudden drop of all spectral lines (DI, CIII, and HeI), which is signature of reduced plasma wall interaction. This drop is accompanied by a significant increase of the plasma density, which is consequence of improved particle confinement. An increase of the average electron temperature is observed as well after the transition to the H Mode (a signature of an improvement of the energy confinement). The peaks visible on spectral lines results from the instabilities called Edge Localized Mode (ELM). ELMs result from quasi-periodic collapses of the transport barrier at the plasma edge, which are followed by an enhanced plasma flow toward the tokamak vessel across the magnetic field lines. Consequently, the desorption of deuterium molecules and

impurity atoms (mainly Carbon and Helium) grows, and their flux contaminates plasma.

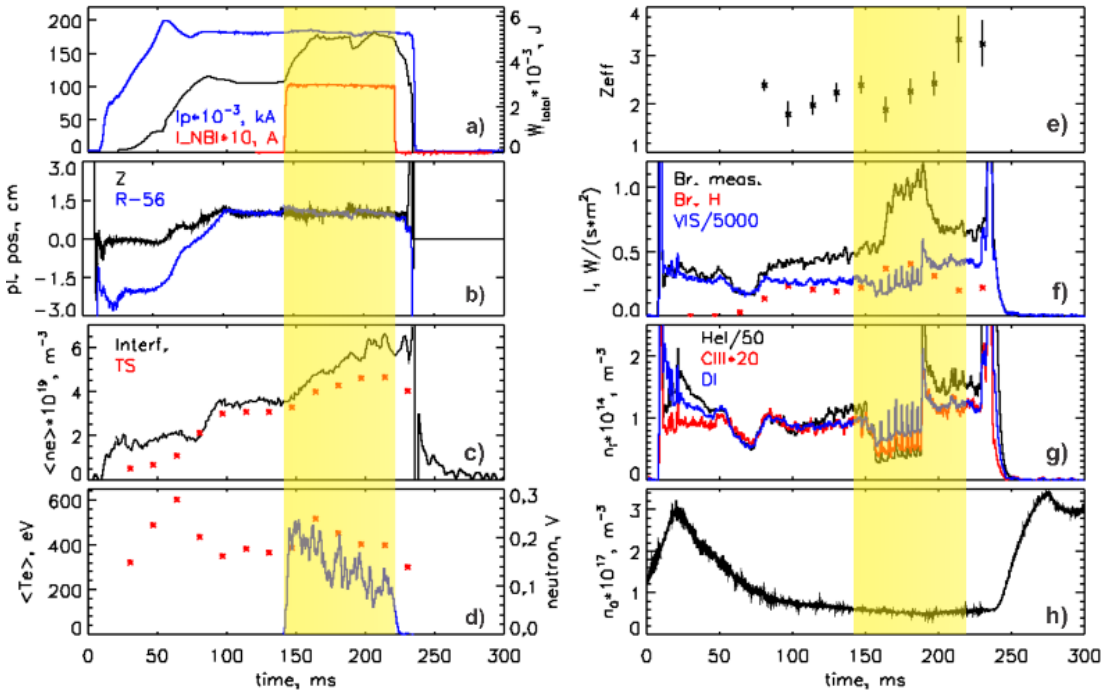

Figure 2.3.6. Plasma position 3, # 11085. a) plasma current (blue), NBI current (red) and total plasma thermal energy (black), b) vertical (black) and horizontal (blue) plasma position, c) average electron density measured by interferometer (black) and calculated from Thomson scattering (TS) system(red), d) average electron temperature calculated from TS electron temperature profiles (red) and neutron flux (blue), e) effective ion charge (Z_{eff}), f) integral visible radiation (blue), measured (black) and calculated for pure deuterium plasma using TS data (red) Bremsstrahlung radiation, g) density of Helium (black) and Deuterium (blue) atoms and CIII ions (red), h) density of Deuterium gas puffed to vacuum chamber to keep plasma density at a prescribed level.

The ELMs phase is terminated by a huge ELM (at t ~ 190 ms), which returns plasma performance to the low confinement regime (L mode).

Conclusion

The main aim of this doctoral thesis was to contribute to tokamak plasma parameter estimation using spectroscopic methods. To achieve it and in the frame of the COMPASS tokamak reinstallation program, new optical systems for measurements of plasma radiation in the tokamak in the visible range were developed [1], [3-7]. We investigated the following systems:

• set of slow (temporal resolution from 5 ms to the total discharge duration) spectroscopic systems with high spectral resolution (0.15 nm, 0.17 nm, 0.04 nm and 0.23 nm) for plasma radiation measurements in the rage of 247-1084 nm,

• set of optical systems for fast (temporal resolution 0.5 μs) spectrally resolved measurements of the most intensive spectral lines,

• visible part of the multichannel optical system for fast (1 μs) plasma radiation measurements with a high spatial resolution (~1 cm),

• high resolved (0.004 nm) spectroscopic system with the temporal resolution of ~10 ms for plasma rotation measurements. The system allows the temperature estimation of impurities observed by the system.

Two of them (PMT-based systems and the set of spectrometers) and the results obtained by their usage are in details discussed in the thesis.

The set of mini-spectrometers from Ocean Optics allows spectrally resolved measurements of a plasma radiation in the range of 250-1080 nm with a low temporal resolution [10]. A low spectral resolution of wide range spectrometers does not allow to estimate the temperature of ions and atoms using measured spectra [3]. Moreover, a low quantum efficiency of the spectrometer detector yields to measure only the most intensive spectral lines.

The system based on photomultipliers has a high quantum efficiency but a very low spectral resolution limited by the interference filter [41]. A set of such PMT-based systems is enable to measure Hα, HeI, CIII, BII lines, integral visible and Bremsstrahlung radiation. A limitation in the available optical connection does not allow to connect all these systems simultaneously.

The final aim of the constructed spectroscopic system is calculating of different discharge parameters, for example the ion density, Zeff, etc. using plasma irradiance.

Absolute calibration of all developed systems was done after recalculation of signals measured in levels or Volts to units of irradiance [11]. All sources of calibration imprecisions were estimated for each system separately [11], [12], [47]. A poor spectral resolution of PMT based systems causes additional imprecision connected with discharge parameters. It is represented by parasitic spectral line radiation. Slow spectroscopic measurements with the high spectral resolution should be done to control influence of these parasitic spectral lines to the resulting signal measured by the PMT based system. The further source of imprecisions connected with the tokamak operation is a temporal evolution of first window transmittance caused by boron redeposition during the boronization procedure and following operational regime discharges. Shutter installed in front of first window significantly decreases this effect, but anyway cleaning of first window from redeposited material should be periodically done.

In the frame of the COMPASS operational program, the plasma irradiance in the spectral range of 250-1080 nm was measured in a set of discharges [3], [4], [12], [41]. Two ways of its interpretation were used: first one based on the NIST atomic data base composed from tabulated experimental results, and second one based on the FLYCHK code using collisional-radiative approximation. A limited quantum sensitivity of used spectrometers was taken into account for the spectrum interpretation. Quite low spectral resolution does not allow interpretation of all spectral lines unequivocally. Therefore, each possible interpretation was considered. On the base of received results it is possible to conclude that only hydrogen, helium, carbon and boron spectral lines are present in a typical spectrum measured in the COMPASS plasma. In some cases, the most intensive lines of oxygen were identified. The spectral lines of elements belonging to the vacuum vessel material appear only in the case of extremely high plasma wall interaction.

The FLYCHK code allows us to create synthetic spectrum on the base of measured electron temperature, electron density, and Zeff [31]. The profiles of all main impurities were plotted for the D-shape and circular plasma. The profiles do not suppose existence of neutral atoms of plasma impurities. Their presence in real spectrum can be explained by interaction of the plasma with wall and with charge-exchange recombination of ions in higher ionized state or by desorption/sublimation of wall impurities.

The effective ion charge is one of the important plasma parameters in tokamaks. The code yields to estimate of Zeff using the measured value of Bremsstrahlung radiation and temperature and density profiles was developed in the frame of this thesis. The values in the range from 1.18 to roughly 4 were received after multiple calculations for different plasma densities and temperatures. There are two possible explanations of so high value of Zeff in our tokamak. First one is that parasitic spectral lines exist in the operational range of the PMT based system for Bremsstrahlung radiation measurements. The influence of these parasitic spectral lines to measured Bremsstrahlung radiation becomes finite for low density plasma. Second possible explanation of unrealistically high Zeff is based on observations of first few discharges after the glow discharge procedure in which extremely high levels of helium (till 50%) and boron (till 10%) were detected. Unfortunately, at this moment, available optical systems at the COMPASS tokamak are not able to give the exact answer which of processes and in which experimental conditions are dominant. Additional studying of this problem using a new spectrometer with the higher resolution and quantum sensitivity than available one in the operational range of PMT based system for Bremsstrahlung radiation measurements is necessary to provide.

The total upgrade of the COMPASS tokamak will be performed till 2021. Upgraded version, so called COMPASS-U, will be a high magnetic field device with the ITER relevant plasma geometry. The purpose of the project is to enlarge the COMPASS operational space, to improve its performance and to address some of the key gaps in the Plasma Exhaust Physics (PEX). The optical equipment discussed in the thesis (three HR2000+ spectrometers and PMT based systems) will be directly transferred from COMPASS to COMPASS- U, except the diagnostic port plugs, which will be newly manufactured. Moreover, the multichannel system for integral visible radiation measurements was developed in frame of but it was not discussed in this thesis. This system will be strongly updated for resolved Bremsstrahlung radiation measurements allowing spatially resolved Zeff estimation and finally, it will be reinstalled to COMPASS-U.

Bibliography

[1] V. Weinzettl, M. Imrisek, J. Havlicek, J. Mlynar, D. Naydenkova, P. Hacek, M. Hron, F. Janky, D. Sarychev, M. Berta, A. Bencze, and T. Szabolics. On Use of Semiconductor Detector Arrays on COMPASS Tokamak. *World Academy of Science, Engineering and Technology*, **71**, 844-850, 2012.

[2] K. Kamiya, M. Bakhtiari, S. Kasai, H. Kawashima, Y. Kusama, Y. Miura, H. Ogawa, N. Oyama, M. Sato, K. Shinohara, K. Tsuzuki, K. Uehara and JFT-2M Group. High recycling steady H-mode regime in the JFT-2M tokamak. *Plasma Phys. Control Fusion*, **46**, A157–A163, 2004.

[3] D. Naydenkova, J. Stöckel, V. Weinzettl, D. Šesták, J. Havlíček, First Spectroscopic Measurements on the COMPASS Tokamak. *WDS'09 Proceeding of Contributed Papers: Part II – Physics of Plasmas and Ionized Media (eds. J. Safrankova and J. Pavlu)*, Prague, Matfyzpress, pp. 158–162, 2009.

[4] D. I. Naydenkova, F. Janky, V. Weinzettl, J. Stockel, D. Sestak, T. Odstrcil, J. Ghosh, R. Gomes, T. Pereira. Measurements of Ion Temperature in the Edge Plasma of the COMPASS Tokamak. *WDS'11 Proceeding of Contributed Papers: Part II – Physics of Plasmas and Ionized Media (eds. J. Safrankova and J. Pavlu)*, Prague, Matfyzpress, pp. 233–236, 2011.

[5] D. Naydenkova, V. Weinzettl, J. Stöckel, D. Šesták, F. Janky. The Complex of the Optical System for Visible Plasma Radiation Measurements in the COMPASS Tokamak. *Acta Technica*, Supplement to Topical Issue, 56 (2011), T93-T100, ISSN 0001-7043.

[6] D. I. Naydenkova, V. Weinzettl, J. Stöckel, D. Šesták, M. Aftanas, Design of New Optical System for Visible Plasma Radiation Measurements at COMPASS Tokamak. *WDS'08 Proceeding of Contributed Papers: Part II – Physics of Plasmas and Ionized Media (eds. J. Safrankova and J. Pavlu)*, Prague, Matfyzpress, pp. 100-104, 2008.

[7] D. I. Naydenkova, V. Weinzettl, J. Stockel, D. Sestak, F. Janky, L. Sedlak, Progress in Multichannel Optical System for Visible Plasma Radiation Measurement at COMPASS Tokamak. *WDS'09 Proceeding of Contributed Papers: Part II – Physics of Plasmas and Ionized Media (eds. J. Safrankova and J. Pavlu)*, Prague, Matfyzpress, pp. 18–21, 2010.

[8] S. Campbell, O. Blomster, M. Pålsson. Comparison of Small Fibre Connectors for High-Power Transmission. SPIE Photonics West conference in San Francisco, *Optoskand AB,* 7578-61, January 2010.

[9] B. Gonçalves, J. Sousa, A. Batista, R. Pereira, M. Correia, A. Neto, B. Carvalho, H. Fernandes, C.A.F. Varandas. ATCA Advanced Control and Data acquisition systems for fusion experiments. *Transactions on Nuclear Science*, **57**(4), 2147-2154, August 2010.

[10] http://oceanoptics.com/product/hr2000-custom/

[11] D. I. Naydenkova, V. Weinzettl, J. Stockel, P. Háček, M. Imríšek. Absolute Sensitivity Calibration of Visible Spectroscopic Diagnostic and Temporal Evolution of First Window Transmittance at the COMPASS Tokamak. *WDS'13 Proceeding of Contributed Papers: Part II – Physics of Plasmas and Ionized Media (eds. J. Safrankova and J. Pavlu)*, Prague, Matfyzpress, pp. 97–103, 2013.

[12] D. Naydenkova, J. Stöckel, V. Weinzettl. The Absolute Sensitivity Measurements of Spectra in Near IR Range at the COMPASS Tokamak. *WDS'14 Proceeding of Contributed Papers: Part II – Physics of Plasmas and Ionized Media (eds. J. Safrankova and J. Pavlu)*, Prague, Matfyzpress, pp. 215-220, 2014, ISBN 978-80-7378-276-4.

[13] K. D. Lawson, I. H. Coffey, J. Zacks, M. F. Stamp and JET-EFDA contributors. An absolute sensitivity calibration of the JET VUV SPRED spectrometer. *Journal of Instruments, **4**, April 2009,* doi:10.1088/1748-0221/4/04/P04013.

[14] http://www.newport.com/Calibrated-Sources-and-Services/378236/1033/info.aspx

[15] https://oceanoptics.com/wp-content/uploads/SONY-ILX511A.pdf

[16] Robert E. Parks. Alignment of Optical Systems. *International Optical Design Conference*, Vancouver, Canada, June 4, 2006, ISBN: 1-55752-811-X.

[17] Bahaa E. A. Saleh, Malvin Carl Teich. Fundamental of Photonics. Wiley-Interscience, A. John Wiley & Sons, Inc. Publication. 2007. ISBNs: 0-471-83965-5.

[18] Wang Zhi-wen, Yan Dong-hai, and Wang En-yao. A Study on Helium Glow Discharge Cleaning in the HL-1M Tokamak. *Plasma Science and Technology*, **4**(6), 1565-1572, 2002.

[19] F.L. Tabarés, E. de la Cal, D. Tafalla, R. Balbín, T. Estrada, I. García-Cortés, M.A. Ochando, M.A. Pedrosa, B. Zurro. Boronization of the TJ-I

tokamak by trimethylboron and decaborane. *Journal of Nuclear Materials*, 220-222, 688-692, 1995.

[20] Tommi Kaplas, Lasse Karvonen, John Rönn, Muhammad Rizwan Saleem, Sami Kujala, Seppo Honkanen, and Yuri Svirko. Nonlinear refraction in semitransparent pyrolytic carbon films. *Optical Materials Express*, **2**(13), 165-184, 2012, DOI:10.1364/OME.2.001822.

[21] Carlton, R. A., Lyman, C. E. and Roberts, J. E. Accuracy and precision of quantitative energy-dispersive x-ray spectrometry in the environmental scanning electron microscope. *Scanning*, **26**, pp. 167–174, 2004, doi:10.1002/sca.4950260404.

[22] A. Nagashima, T. Nishitani, T. Fujisawa, T. Sugie, S. Kasai. Development of vacuum seals for diagnostic windows of the International Thermonuclear Experimental Reactor. *REV SCI INS*, **70**(1), 460-463, 1999.

[23**]** J. Havlicek and J. Urban. A Magnetic Equilibrium Reconstruction in Tokamak. *WDS'07 Proceeding of Contributed Papers: Part II – Physics of Plasmas and Ionized Media (eds. J. Safrankova and J. Pavlu)*, Prague, Matfyzpress, pp. 234-239, 2007.

[24] John Wesson. Tokamaks. Third edition. Clarendon press, Oxford, 2004, ISBN 0198509227.

[25] K. Brau, S. Suckewer and S.K. Wong. Vertical poloidal asymmetries of low-Z element radiation in the PDX tokamak. *Nucl. Fusion,* **23** 1657, 1983.

[26] https://oceanoptics.com/measurementtechnique/irradiance/

[27] A. Kramida, Yu. Ralchenko, J. Reader and NIST ASD Team. NIST Atomic Spectra Database (version 5.4). National Institute of Standards and Technology, Gaithersburg, MD, 20l6, http://physics.nist.gov/asd.

[28] J. Reader and C.H. Corliss, Line Spectra of the Elements, CRC Handbook of Chemistry and Physics, 77th Edition, D.R. Lide, Ed., CRC Press, Boca Raton, FL, 1997.

[29] W.C. Martin, R. Zalubas, and L. Hagan, Atomic Energy Levels - The Rare-Earth Elements, Nat. Stand. Ref. Data Series, Nat. Bur. Stand (U.S.) **60**, 1978.

[30] G.W.F. Drake (Ed.), Springer Handbook of Atomic, Molecular and Optical Physics, 2nd edition, Springer Science+ Business Media Inc., New York, USA, 2006, ISBN: 978-0-387-20802-2.

[31] H.-K. Chung, M.H. Chen, W.L. Morgan, Yu. Ralchenko and R.W. Lee. FLYCHK: Generalized population kinetics and spectral model for rapid spectroscopic analysis for all elements. High Energy Density Physics, **1**(3), 2005.

[32] L. D. Landau and E. M. Lifshitz: The Theory of Fields (Volume 2 of A Course of Theoretical Physics). Science, Moskou, 1974.

[33] V. B. Berestetskii, E. M. Lifshitz and L. P. Pitaevskii: Quantum Electrodinamics (Volume 4 of A Course of Theoretical Phisics). Science, Moskou, 1979.

[34] N. P. Basse, A. Dominguez, E. M. Edlund, C. L. Fiore, R. S. Granetz, A. E. Hubbard, J. W. Hughes, I. H. Hutchinson, J. H. Irby, B. LaBombard, L. Lin, Y. Lin, B. Lipschultz, J. E. Liptac, E. S. Marmar, D. A. Mossessian, R. R. Parker, M. Porkolab, J. E. Rice, J. A. Snipes, V. Tang, J. L. Terry, S. M. Wolfe, S. J. Wukitch, K. Zhurovich, R. V. Bravenec, P. E. Phillips, W. L. Rowan, G. J. Kramer, G. Schilling, S. D. Scott, S. J. Zweben. Diagnostic Systems on Alcator C-Mod. *Fusion Science and Technology*, **51**(3), 476-507, April 2007.

[35] B. Schunke, C. DeMichelis, R. Guirlet, P. Monier-Garbet, M. Mattioli, E. Chareyre, O. Meyer. Consistency check of Z_{eff} measurements in ergodic divertor plasmas on Tore Supra. 14th Int. Conf. on Plasma-Surface Interactions in Controlled Fusion Devices. *Journal of Nuclear Materials*, **290–293,** 715–719, March 2001.

[36] A. Patel, P. G. Carolan, N. J. Conway and R. J. Akers. Zeff profile measurements from bremsstrahlung imaging in the MAST spherical tokamak. *Rev. Sci. Instrum.* **75**, 4944, 2004, http://dx.doi.org/10.1063/1.1808915.

[37] M. A. Van Zeeland, J. H. Yu, N. H. Brooks, W. W. Heidbrink, K. H. Burrell, R. J. Groebner, A. W. Hyatt, T. C. Luce, N. Pablant, W. M. Solomon, M. R. Wade. Active and passive spectroscopic imaging in the DIII-D tokamak. *Plasma Phys. Control. Fusion* **52,** 045006, 2010, doi:10.1088/0741-3335/52/4/045006.

[38] H. Meister, R. Fischer, L. D. Horton, C. F. Maggi, D. Nishijima, ASDEX Upgrade Team, C. Giroud, K.-D. Zastrow, JET-EFDA Contributors and B. Zaniol. Zeff from spectroscopic bremsstrahlung measurements at ASDEX Upgrade and JET. *Rev. Sci. Instrum.* **75**, 4097, 2004.

[39] Z.W. Wu, J. Li, B.N. Wan, X.D. Zhang, X. Gao, J. Zhao. Reduced effective ionic charge and enhanced plasma performance in the HT-7 tokamak. *Journal of Nuclear Materials* **363–365**, 1380–1385, 2007.

[40] Hangyu Zhou, Shigeru Morita, Motoshi Goto, Kazumichi Narihara and Ichihiro Yamada. Application of Zeff Profile Analysis Based on Visible Bremsstrahlung

Measurement to Different Density Profiles in the LHD. *Plasma and Fusion Research*, **5**, 01/2010, DOI: 10.1585/pfr.5.S1021.

[41] D. Naydenkova**,** J. Stöckel, V. Weinzettl, D. Šesták, J. Havlicek, Spectroscopic Measurements on the COMPASS Tokamak. *WDS'12 Proceedings of Contributed Papers Part II – Physics of Plasmas and Ionized Media (eds. J. Safrankova and J. Pavlu)*, (Matfyzpress, 2012), pp. 222–227.

[42] https://www.andovercorp.com/products/bandpass-filters/semi-custom-bandpass-filters/

[43] D.F. Valcárcel, A. Neto, J. Sousa, B.B. Carvalho, H. Fernandes, J.C. Fortunato, A.S. Gouveia, A.J.N. Batista, A.G. Fernandes, M. Correia, T. Pereira, I.S. Carvalho, A.S. Duarte, C.A.F. Varandas, M. Hron, F. Janky, J. Písačka. An ATCA Embedded Data Acquisition and Control System for the Compass tokamak. Proceeding of the 25th Symposium on Fusion Technology (SOFT-25). *Fusion Engineering and Design***, 84**, 7–11, 1901–1904, June 2009, doi:10.1016/j.fusengdes.2008.12.011.

[44] G.V. Marr. Plasma Spectroscopy. Elsevier Publishing Company, England, 1968.

[45] A. Burgess and H. P. Summers. Radiative Gaunt factors. *Monthly Notices of the Royal Astronomical Society*, **226**, pp. 257-272, May 15, 1987, ISSN 0035-8711.

[46] M. Aftanas, P. Bohm, P. Bilkova, V. Weinzettl, J. Zajac, F. Zacek, J. Stockel, M. Hron, R. Panek, R. Scannell and M. J. Walsh. High-resolution Thomson scattering system on the COMPASS tokamak: Evaluation of plasma parameters and error analysis. *Rev. Sci. Instrum.* **83**, 10E350, 2012, http://dx.doi.org/10.1063/1.4743956.

[47] D. I. Naydenkova, V. Weinzettl, J. Stockel, and J. Matějíček. On the precision of absolute sensitivity calibration and specifics of spectroscopic quantities interpretation in tokamaks. *Appl. Opt.* **53**, 8123-8130, 2014, DOI: 10.1364/AO.53.008123.

[48] A. Patel, P. G. Carolan, N. J. Conway and R. J. Akers. Zeff profile measurements from bremsstrahlung imaging in the MAST spherical tokamak. *Rev. Sci. Instrum.* **75**, 4944, 2004, http://dx.doi.org/10.1063/1.1808915.

[49] A.V. Gorbunov, L.A. Klyuchnikov, K.V. Korobov. Visible range spectrum of the T-10 tokamak plasma. PAST, Series: Fusion, **38**(2), pp. 62-67, 2015.

[50] P. Deichuli, V. Davydenko, V. Belov, A. Gorbovsky and A. Dranichnikov. Commissioning of heating neutral beams for COMPASS-D tokamak. *Rev.Sci.Instrum.* **83**, 02B114-1–02B114-3, 2012, DOI: 10 10.1063/1.3672108.

[51] Klara Mitosinkova, Jan Stöckel, Jozef Varju, Vladimir Weinzettl, Energy composition of high-energy neutral beams on the COMPASS tokamak. *Nukleonika*, **61**(4), 419-423, 2016, doi: 10.1515/nuka-2016-0069.

[52] Jakub Urban, Michal Stránský, Vladimír Fuchs, Irina Voitsekhovitch and Martin Valovič, Self-consistent transport simulations of COMPASS operation with optimized NBI. *Plasma Phys. Control. Fusion*, **52**, 045008, 2010.

[53] K. Mitosinkova, J. Stockel, private comunication.

[54] R. Pánek, J. Adámek, M. Aftanas, P. Bílková, P. Böhm, F. Brochard, P. Cahyna, J. Cavalier, R. Dejarnac, M. Dimitrova, O. Grover, J. Harrison, P. Háček, J. Havlíček, A. Havránek, J. Horáček, M. Hron, M. Imríšek, F. Janky, A. Kirk, M. Komm, K. Kovařík, J. Krbec, L. Kripner, T. Markovič, K. Mitošinková, J. Mlynář, D. Naydenkova, M. Peterka, J. Seidl, J. Stöckel, E. Štefániková, M. Tomeš, J. Urban, P. Vondráček, M. Varavin, J. Varju, V. Weinzettl, J. Zajac and the COMPASS team. Status of the COMPASS tokamak and characterization of the first H-mode. *Plasma Phys. Control. Fusion*, **58**, 014015, 2016.

List of Tables

List of Abbreviations

UKAEA	United Kingdom Atomic Energy Authority
IPP AV CR v.v.i.	Institute of Plasma Physics of the Czech Academy of Sciences
NIST	National Institute of Standards and Technology
TOPTEC	Turnov OPToElectronic Centre
JET	Joint European Torus
ITER	International Thermonuclear Experimental Reactor
COMPASS	COMPact ASSembly
ASDEX-U	Axially Symmetric Divertor EXperiment- Upgrade
MAST	Mega Ampere Spherical Tokamak
CASTOR	Czech Academy of Science TORus
DIII-D	Doublet III-Divertor
HT-7	Hefei Tokamak-7
LHD	Large Helical Device
TS	Thomson Scattering
EDS	Energy-Dispersive Spectrometry
NBI	Neutral Beam Injectors
PS	Power Supply
DAQ	Data Acquisition System
HR2000+	High Resolution minispectrometer from Ocean Optics
PMT	PhotoMulTiplier
CCD	Charge-Coupled Device
UV-VIS high OH	UltraViolet\VISible optical fibre with high OH content
VIS/NIR low OH	VISible\ Near Infrared optical fibre with low OH content
SMA	SubMiniature version A
BK7	borosilicate glass Schott
NA	Numerical Aperture
QE	Quantum Efficiency
FWHM	Full Width at Half Maximum
HFS	High Field Side
LFS	Low Field Side
SNT	Single Null divertor with higher Triangularity
SOL	Scrape-Off Layer

H mode	High (improved) energy confinement mode
L mode	Low energy confinement mode
ELM	Edge-Localized Mode
NUV	Near UltraViolet
NIR	Near InfraRed
HXR	Hard X-Rays
RF	Radio frequency
EFIT code	Equilibrium FITting code
FLYCHK	Extended FLY model included kinetics models for all ion stages
CR model	Collisional-Radiative model

Attachment 1. Table of spectral lines in wavelength range 247-1083 nm for D-shape discharge at COMPASS tokamak

The full list of spectral lines observed at COMPASS tokamak D-shape discharges is presented in this attachment. The measurements with temporal integration during discharge duration were used. Unexplained spectral lines are marked by violet colour. Spectral lines in the column with FLYCHK result marked by black colour mean the lines which are expected to radiate from scrap-off layer or boundary plasma. Lines marked by red colour correspond to radiation expected from the plasma centrum.

Measured spectral lines (nm)	NIST interpritation (typical discharge) (nm)	NIST interpritation (brocken shields) (nm)	FLYCHK interpritation (nm)
277.9-278.6	OV (278.10)		OIV (277.2), OIV (277.1), OIII (277.9), OIII (277.2), OIII (277.3), BV (277.7), CIII (276.6), CIII (276.7), CIII (276.8)
278.6-279.3	OV (278.699), OV (278.985)	CaIII (279.16)	CII (279.1), OVII (279.6)
280.-281.5		TiII (280.047), CaIII (281.39)	BIII (280.5), CIV (281.9), OV (281.4), OIII (281.3), OVIII (281.5)
282.1-282.9	BIV (282.16), BIV (282.45), BIV (282.58)		BIV (282.6), CV (282.8)
283.7-284.2		CrII (283.56)	CVI (284.7), OII (283.2), BV (283.5), CIII (283.4)
298.3-298.7	OIII (298.378)		BV (298.2), OV (298.5), OV (298.2), OV (297.5), OV (298.6), BIV (300.2), OVIII (297.4), OVII (298.1)

304.6-304.95	OIII (304.713)		OV (304.5), OV (304.4), OV (304.3), OIII (305.3), BIII (303.9), CII (303.8), OVIII (304.2), OVII (305.1)
306.3-306.7			CVI (306.1), CV (307.6)
320.2-320.7		TiII (320.25)	CIV (320.0), HeII (320.4), BIV (318.9), CV (321.1), CVI (318.9), CVI (320.2), OVIII (320.1)
326.1-327.0	OIII (326.098), OIII (326.546)		BIII (326.9), CIII (326.0), BV (326.0), CV (325.7), CVI (327.2), OVIII (326.4)
332.2-332.8		MoVI (332.37)	CV (331.1)
337.2-337.4		TiII (337.28), CaIII (337.26)	BIII (337.1), BIII (337.4), BIII (337.5), CVI (337.3)
338.0-338.9		OIV (338.12), OIV (338.55), TiII (338.37), TiII (338.78)	BIV (339.4), CIII (338.8), OV (339.2), OV (338.0), BV (339.2)
344.2-346.2	HeI (344.76), HeI (344.93), BII (345.35)	CoI (345.35)	BV (343.4), BV (346.3), CVI (343.3), CVI (343.7), OVI (343.1), OVII (343.7)
347.8-348.6		MoVI (347.66)	BV (348.6), CVI (349.3), OVIII (348.6), OVIII (348.4), OVII (349.0)
350.69-350.91			BIV (350.5), OIII (351.0), BIV (352.5), BV (350.2), CVI (349.9)
370.2-370.8	HI (370.38),	MoVI (370.52)	BV (370.2),

	HeI (370.5), HeI (370.51)		CIII (371.1), CIII (371.3), HI (370.9), HI (370.1), CIV (368.7), HI (369.4), OVIII (369.4)
372.4-373.3		OIV (372.593), OIV 372.903)	HI (373.1), HI (371.9), OVIII (372.4)
373.6-374.03		MoVI (373.53), OIV (373.68)	HeII (374.1), OIV (373.2), OIV (373.4), OIV (373.3)
374.9-375.3	DI (374.91), HI (371.01)	FeI (374.94)	CV (374.6), HeII (374.9), HI (374.7)
375.2-376.3	OIII (375.467), OIII (375.987)	FeI (376.00), TiII (376.13), CaIII (376.16)	BV (375.4), HeII (375.9), HI (376.7)
377.2-377.7		CuIII(377.697)	HeII (377.0), OIII (377.0), HeII (378.2), OVII (377.2)
379.1-379.6	OIII (379.12)		HeII (379.7), HeII (381.4), HI (379.5), BIV (381.2), BV (380.6), CV (381.3), CVI (379.6)
384.6-385			BIV (384.2), HeII (385.9), HI (383.2), OVII (384.7)
387.6-388.0		CII (387.62), CII (387.64), CII (387.666)	CVI (386.9), CVI (387.5)
388.8-389.25	DI (388.8), HeI (388.86), HI (388.9)		HeII (388.8), HI (388.6), OVIII (389.8)
391.07-391.6		TiI (391.43)	OV (390.8)
391.7-392.4		TiI (392.14)	HeII (392.4), BIV (392.9)
394.4-394.8		TiI (394.77)	CIII (393.8), BV (393.6), CVI (393.6)
395.2-395.9			
396.15-396.65	OIII (396.59)	TiI (396.28), TiI (396.42)	HeII (396.9)

396.7-397.8	DI (396.89), HI (397.0), HeI (397.2)		HI (396.6), OIV (397.2), CVI (396.9), CV (398.5)
402.5-403.0	HeI (402.61)		BIII (403.5), HeII (402.6), OVII (401.7)
406.6-408.3		CII (407.452), CII (407.585), CaIII (408.177)	BIV (407.8), CVI (408.2), OVIII (406.2), OVIII (408.3)
409.5-410.7	DI (410.05), HI (410.17)		BIV (411.2), HeII (410.1), HI (409.8), BV (410.2), CV (408.9), OVII (410.7), OVII (410.8)
412.15-412.7		OV (412.399)	CII (413.9)
426.6-427.33			OIII (426.3)
427.5-427.33	Deexcitation peak		BIV (427.5)
432.45-433.3	CIII (432.556)		CIII (430.9), BV (431.9)
433.6-434.7	DI (433.92), HI (434.04)		HeII (433.9), HI (433.6), BV (433.9), OVIII (433.8), OVII (434.6)
434.75-435.6		CuII (435.28)	OIV (436.3), OIV (436.5), CV (436.3), OVII (435.4)
441.5-442.0			BIII (442.2), BV (441.0)
444.5-444.8			CIV (444.2), CII (444.8), OIV (444.0), OIV (443.7)
445.1-445.8		TiI (445.089), TiI (445.37)	CII (445.0)
446.3-447.7	HeI (447.15)		BII (447.9), HeI (446.4), OIV (447.7)
448.6-449.1			BIII (448.7), OIV (449.3), BV (449.4)
449.7-450.2		CaIII (449.99)	BIII (450.5), BIII (449.8), CIII (449.6), CIII (449.8),

			OVI (449.6), OIII (449.8), OII (450.5), CVI (449.8), OVI (449.6), OVIII (449.9)
451.5-452.0			BIV (451.0), BV (452.1), OVIII (452.0)
453.63-453.83			BIV (454.2), HeII (454.2)
458.7-460.2			CIII (460.2), CV (457.3), BV (459.4), BV (461.3), CVI (460.5), OVII (459.4)
464.3-465.4	CIII (464.74), CIII (465.025), CIII (465.15)		BIV (465.0), CIII (465.5), OIII (463.8), OIV (465.0), BIII (463.5), OVIII (465.5)
465.5-466.2	CIII (466.586)	CIV (465.83)	CIV (465.4), CIII (465.5), CIII (465.7), CIV (466.5), CIV (466.7), OIV (466.4), OIV (466.2), OIV (466.0)
467.1-468.2			BIV (468.1), CIV (468.2)
468.2-469.1	HeII (468.54- 468.59)		OIII (468.5), OIII (468.3), CIII (468.7), HeII (468.7), CVI (468.4), OVIII (468.6), OVIII (468.3)
485.4-486.6	DI (485.99), HI (486.13)		CIII (484.4), BIV (485.4), HeII (486.0), HI (485.6), OIV (485.2), BV (486.0), CVI (485.8)
491.55-492.6	HeI (492.06), HeI (492.19)		BIV (492.3), BIII (492.1), CV (491.8),

			CVI (491.8), OVII (490.7)
493.5-494.8			OIV (493.5), OIV (493.3), BV (494.6), BV (495.2)
501.2-502.0	HeI (501.57)		BV (503.2), CVI (500.6), OVIII (500.2), OVIII (501.9), OVIII (502.6)
512.8-513.6	CII (513.294), CII (513.328)	CoII (512.92)	OV (512.5), OIII (513.1), OIII (512.9)
513.6-514.1			
514.1-514.8	CII (514.349), CII (514.516)		OV (514.8)
514.8-515.0	CII (515.109)		BIV (515.2), OIV (515.2)
516.25-516.85			BIV (516.2), BIII (516.2), BIII (517.0), BIII (517.1), OV (515.5), OIV (515.5), CV (518.1), CVI (516.6)
528.1-529.6		CoII (528.062)	OVI (528.7), BV (527.2), CVI (527.2), CVI (528.9), OVII (530.2)
540.95-541.35			HeII (541.3), CVI (541.0)
558.8-559.5	OIII (559.237)		BV (558.3), OIV (559.9)
564.65-564.95	CII (564.807)		OIV (564.5)
565.65-566.6	CII (566.247)		BIV (566.4)
566.6-567.2			OV (566.8), BV (567.0)
569.15-569.9	CIII (569.592)		BIII (569.0), CV (569.1), CVI (569.3), OVIII (569.1)
578.5-578.75			CV (578.2), OVIII (579.0)
579.8-580.5	CIV (580.133)		OIII (580.1), OIII (579.6), CVI (580.5)
581.0-581.7	CIV (581.198)		CIV (581.1)

581.7-582.7			OIII (582.8)
586.95-588.15	HeI (587.44-587.597)		BV (588.0), CVI (586.1)
588.6-589.4			
619.7-620.3			CVI (619.7), CVI (619.9)
620.3-620.9			
645.7-647.2			CV (645.5), BV (648.0), CV (648.1), OVII (644.4)
649.6-650.55			BIV (649.4)
654.0-657.3	HeII (655.97-656.02), DI (656.09), HI (656.27)		BIII (655.4), CIII (656.3), HeII (656.1), HeII (652.9), HI (655.4), BV (656.1), CVI (655.8), CVI (657.0), OVIII (653.5), OVIII (655.6)
657.3-658.7	CII (657.805), CII (658.288)		CV (658.1), BIV (659.8)
663.9-664.2	OII (664.1)		BV (663.4)
666.0-669.0	HeI (667.81), FeI (667.8)		HeII (668.4)
671.5-673.4	OII (672.14), OI (672.63), OI (672.65), CII (672.456), CII (672.7), CII (672.73), CIII (672.75), CIII (673.1), BII (671.76)		OVII (670.7)
674.2-674.8	CIII (674.4)		BV (674.8)
677.0-679.6	CII (678.39), BII (678.61)		CV (676.1)
679.6-680.4	CII (680.1)		BV (682.0)
689.4-689.8			HeII (689.2)
690.5-691.1			BIV (691.3)
702.0-703.8	BII (703.027), BII (703.2), BII (703.23)		BV (703.9)
705.5-707.1	HeI (706.5)		CIV (705.7), OVIII (705.8), OVIII (705.7), OVII (705.1), OVIII (707.5)

710.7-712.5	CII (711.56), CII (711.99)		CV (711.5)
722.3-724.5	CII (723.7), CII (723.13), CII (723.6), BII (722.85)		BV (721.2), CV (725.5), CVI (722.5)
727.4-728.6	HeI (728.13)		
745.3- 745.9	OIII (745.54)		BV (744.2)
751.5-752.0	OIII (751.6)		CVI (751.7)
758.5-760.0			HeII (759.4), BV (758.7)
760.9-762.2	BV (761.88)		BV (762.0)
763.5-764.1	BII (763.86)		OVIII (764.8)
771.2-772.0	OIII (771.095), OIV (771.45)		CIII (770.5), OVI (771.3), OIII (771.4), CVI (771.5), OVII (770.3), OVI (771.3)
772.1-773.2	CIV (772.67)		CIV (772.0), OVIII (772.2), OVIII (773.1)
776.6-778.0	OI (777.19), OI (777.42), OI (777.54)		
783.2-784.5	BIII (783.52), BIII (784.14)		BIV (784.3), BIII (783.6), BIII (783.4)
791.9-792.9			
817.0-817.5			
819.3-820.4	CIII (819.65)		BV (820.1), CV (819.6), CV (821.0), OVIII (819.8)
823.3-824.0			HeII (823.8), OIV (824.8)
825.8-826.3	HI (826.09)		CIII (826.5), OIII (825.9), OVIII (825.2)
827.7-828.5	HI (828.11)		BIII (827.4), CV (827.7), CIII (828.1), CIII (828.7), OIII (828.1), OIII (828.7), BIII (829.5), BIII (829.7), CVI (828.0)
832.5-833.8	CI (833.515), BII (833.0)		BIII (832.3), HI (833.3),

	BII (833.8)		HI (832.3), HI (834.5), CVI (832.8), CVI (833.4), OVII (831.9), OVII (833.8)
844.3-845.1	OI (844.625), OI (844.636), OI (844.676), CV (844.8)		HI (843.7), OIII (844.5), OIII (843.4), BV (844.3)
882.0-882.5	OI (882.043)		
887.5-887.8			CIII (887.4), CIII (888.1) OIV (886.8), HeII (886.2)
906.0-906.6	CI (906.14), CI (906.25)		BV (905.2), OVIII (906.3)
907.7-908.3	CI (907.83)		CV (907.5)
908.7-909.35	CI (908.85)		
909.35-910.15	CI (909.49)		CIII (910.2), OVII (910.2)
911.0-911.7	CI (911.18)		CIII (911.6), HeII (911.1), OIII (912.2), OVII (911.3)
922.5-923.6	DI (922.65), HeI (922.78), HI (922.9), BII (922.6)		BIV (923.1), HeII (922.8), HI (922.8), OV (924.5)
926.2-927.1	CII (926.73)		CV (925.3)
934.3-935.2	BII (934.71), BII (935.02), OIV (934.17)		HeII (934.7), CVI (934.2)
940.6-941.3	CI (940.57)		
965.3-965.9	CI (965.844), BII (965.12)		CV (964.2), OVIII (966.1)
990.8-991.2	OI (990.9)		CVI (990.6)
1012.8-1013.8	CI (1012.39)		CIV (1011.6), CIII (1012.9), CII (1013.7), HeII (1012.6), CVI (1012.1), OVIII (1011.7)
1084.5-1085.0	HeI (1082.9), HeI (1083.02), HeI (1083.03)		CVI (1085.0)

Attachment 2. Research projects

2008-2011	Modern trends in plasma physics Co-investigator Provider: Czech Science Foundation; Project ID: GD202/08/H057
2009-2012	Multi-range tomographic system for transport studies in tokamak plasmas Co-investigator Provider: Czech Science Foundation; Project ID: GA202/09/1467
2012-2015	Investigation of turbulent plasma boundary of tokamak COMPASS using two deeply-reciprocating probes, interpreted by numerical models Co-investigator Provider: Czech Science Foundation; Project ID: GAP205/12/2327
2014-2016	Interaction of hydrogen isotopes with candidate fusion materials Co-investigator Provider: Czech Science Foundation; Project ID: GA14-12837S

Attachment 3. Publications

3.1. Publications in scientific journals

1. V. Voitsenya, **D. Naydenkova**, S. Masuzaki, Y. Kubota, A. Sagara, and K. Yamazaki. The Discharge in Hydrogen-Noble Gas Mixture as the Method to Increase Efficiency of Conditioning of the In-vessel Components of Large-scale Fusion Devices. Journal of Plasma and Fusion Research, 7 (2006), 114-117.

2. V. S. Voitsenya, A. J. H. Donné, A. F. Bardamid, A. I. Belyaeva, V. L. Berezhnyj, A. A. Galuza, Ch. Gil, V. G. Konovalov, M. Lipa, A. Malaquais, **D. I. Naidenkova**, V. I. Ryzhkov, B. Schunke, S. I. Solodovchenko and A. N. Topkov. Simulation of environment effects on retroreflectors in ITER. Review of Scientific Instruments, 76 (2005) 083502.

3. A. F. Bardamid, A. I. Belyaeva, V. N. Bondarenko, A. A. Galuza, O. G. Kolesnyk, V. G. Konovalov, **D. I. Naidenkova**, I. V. Ryzhkov, A. N. Shapoval, C. H. Skinner, A. F. Shtan, S. I. Solodovchenko, V. S. Voitsenya and K. I. Yakimov. Behaviour of mirrors fabricated from amorphous alloy under impact of deuterium plasma ions. Physica Scripta, 73 (2006), 1-5.

4. A. F. Bardamid, K. Yu. Vukolov, V. G. Konovalov, **D. I. Naidenkova**, A. V. Rogov, I. V. Ryzhkov, A. N. Shapoval, A. F. Shtan, S. I. Solodovchenko, V. S. Voitsenya and K. I. Yakimov. The test of film Mo mirrors under bombardment with ions of deuterium plasma. Plasma Devices and Operations, 14 (June 2006), 159-170.

5. D. Šesták, V. Weinzettl, P. Bílková, P. Böhm, M. Aftanas, **D. I. Naydenkova**, J. Stöckel, I. Ďuran, M. J. Walsh. Design and engineering of optical diagnostics for COMPASS. Fusion Engineering and Design, 84 (2009), 1755-1758.

6. V. Weinzettl, **D. I. Naydenkova**, D. Sestak, J. Vlcek, J. Mlynar, R. Melich, D. Jares, J. Malot, D. Sarych, V. Igochine. Design of multi-range tomographic system for transport studies in tokamak plasmas. Nuclear Instruments and Methods in Physics Research A, 623 (2010), 806–808.

7. V. Weinzettl, R. Panek, M. Hron, J. Stockel, F. Zacek, J. Havlicek, P. Bilkova, **D.I. Naydenkova**, P. Hacek, J. Zajac, R. Dejarnac, J. Horacek, J. Adamek, J. Mlynar, F. Janky, M. Aftanas, P. Bohm, J. Brotankova, D. Sestak,

I. Duran, R. Melich, D. Jares, J. Ghosh, G. Anda, G. Veres, A. Szappanos, S. Zoletnik, M. Berta, V. F. Shevchenko, R. Scannell, M. Walsh, H. W. Müller, V. Igochine, A. Silva, M. Manso, R. Gomes, Tsv. Popov, D. Sarychev, V. K. Kiselov, S. Nanobashvili. Overview of the COMPASS diagnostic. Fusion Engineering and Design, 86, 6-8 (2011), 1227-1231.

8. R. Pánek, M. Aftanas, P. Bílková, P. Böhm, J. Havlíček, J. Horáček, M. Hron, F. Janky, **D. Naydenkova**, J. Stöckel, J. Urban, V. Weinzettl, J. Zajac, F. Žáček. First results of the COMPASS tokamak. Acta Technica CSAV, 56, (2011), T31-T42.

9. V. Weinzettl, M. Imrisek, J. Havlicek, J. Mlynar, **D. Naydenkova**, P. Hacek, M. Hron, F. Janky, D. Sarychev, M. Berta, A. Bencze, and T. Szabolics. On Use of Semiconductor Detector Arrays on COMPASS Tokamak. Engineering and Technology, International Journal of Mathematical, Computational, Physical, Electrical and Computer Engineering, **6** (11), (2012), 1503-1509.

10. **D. I. Naydenkova**, V. Weinzettl, J. Stockel, J. Matějíček. On the precision of absolute sensitivity calibration and specifics of spectroscopic quantities interpretation in tokamaks. Applied Optics, 53, 34 (2014), 8123-8130.

11. R. Pánek, J. Adámek, M. Aftanas, P. Bílková, P. Böhm, F. Brochard, P. Cahyna, J. Cavalier, R. Dejarnac, M. Dimitrova, O. Grover, J. Harrison, P. Háček, J. Havlíček, A. Havránek, J. Horáček, M. Hron, M. Imríšek, F. Janky, A. Kirk, M. Komm, K. Kovařík, J. Krbec, L. Kripner, T. Markovič, K. Mitošinková, J. Mlynář, **D. Naydenkova**, M. Peterka, J. Seidl, J. Stöckel, E. Štefániková, M. Tomeš, J. Urban, P. Vondráček, M. Varavin, J. Varju, V. Weinzettl, J. Zajac and the COMPASS team. Status of the COMPASS tokamak and characterization of the first H-mode. Plasma Physics and Controlled Fusion, 58, 1 (2015), 014015-014015.

12. V. Weinzettl, G. Shukla, J. Ghosh, R. Melich, R. Panek, M. Tomes, M. Imrisek, **D. Naydenkova**, J. Varju, T. Pereira, R. Gomes, I. Abramovic, R. Jaspers, M. Pisarik, T. Odstrcil, G. Van Oost. High-resolution spectroscopy diagnostics for measuring impurity ion temperature and velocity on the COMPASS tokamak. Engineering and Design, (October 2015), 1006-1011.

13. M. Komm, P. Bílková, M. Aftanas, M. Berta, P. Böhm, O. Bogár, L. Frassinetti, O. Grover, P. Háček, J. Havlíček, M. Hron, M. Imríšek, J. Krbec, K. Mitošinková, **D. Naydenkova**, R. Pánek, M. Peterka, P. B. Snyder, E. Stefanikova, J. Stöckel, M. Šos, J. Urban, J. Varju, P. Vondráček, V. Weinzettl:

Contribution to the multi-machine pedestal scaling from COMPASS tokamak. Nuclear Fusion, **57** (5), (2017), 056041.

3.2. Publications in conference proceedings

1. В. В. Власов, **Д. И. Найденкова**, Н. А. Скорик. "Волноводный ферритовый поляризатор 3-см диапазона." Сб. материалов 12-ой Международной конференции «СВЧ – техника и телекоммуникационные технологии» , 2002, Севастополь, pp. 556 – 557. (During my stay in the University.)
2. **D. Naydenkova**, O. Bilyk, J. Stockel. Magnetic Diagnostic Application for COMPASS Tokamak. WDS 2007 - Proceedings of Contributed Papers, Part II – Physics of Plasmas and Ionized Media (eds. J. Safrankova and J. Pavlu), Prague, Matfyzpress, pp. 229–233, 2007, ISBN 978-80-7378-024-1.
3. **D. I. Naydenkova**, V. Weinzettl, J. Stöckel, D. Šesták, M. Aftanas. Design of New Optical System for Visible Plasma Radiation Measurements at COMPASS Tokamak. WDS 2008 - Proceedings of Contributed Papers, Part II– Physics of Plasmas and Ionized Media (eds. J. Safrankova and J. Pavlu), Prague, Matfyzpress, pp. 100-104, 2008, ISBN 978-80-7378-066-1.
4. **D. Naydenkova**, J. Stöckel, V. Weinzettl, D. Šesták, J. Havlíček. First Spectroscopic Measurements on the COMPASS Tokamak. WDS 2009 - Proceedings of Contributed Papers, Part II– Physics of Plasmas and Ionized Media (eds. J. Safrankova and J. Pavlu), Prague, Matfyzpress, pp. 158–162, 2009, ISBN 978-80-7378-066-1.
5. J. Havlicek, J. Horacek, V. Weinzettl, O. Hronova, **D. Naydenkova**, J. Zajac. Magnetic Diagnostics for Start-up Phase of COMPASS. WDS 2009 - Proceedings of Contributed Papers, Part II– Physics of Plasmas and Ionized Media (eds. J. Safrankova and J. Pavlu), Prague, Matfyzpress, pp. 158–162, 2009, ISBN 978-80-7378-066-1.
6. **D. I. Naydenkova**, V. Weinzettl, J. Stockel, D. Sestak, F. Janky, L. Sedlak. Progress in Multichannel Optical System for Visible Plasma Radiation Measurement at COMPASS Tokamak. WDS 2010 - Proceedings of Contributed Papers, Part II– Physics of Plasmas and Ionized Media (eds. J. Safrankova and J. Pavlu), Prague, Matfyzpress, pp. 18–21, 2010, ISBN 978-80-7378-140-8.

7. **D. Naydenkova**, V. Weinzettl, J. Stöckel, D. Šesták, F. Janky. The Complex of the Optical System for Visible Plasma Radiation Measurements in the COMPASS Tokamak. Acta Technica, Supplement to Topical Issue, 56 (2011), pp. T93-T100, ISSN 0001-7043.

8. **D. I. Naydenkova**, F. Janky, V. Weinzettl, J. Stockel, D. Sestak, T. Odstrcil, J. Ghosh, R. Gomes, T. Pereira. Measurements of Ion Temperature in the Edge Plasma of the COMPASS Tokamak. WDS 2011 - Proceedings of Contributed Papers, Part II– Physics of Plasmas and Ionized Media (eds. J. Safrankova and J. Pavlu), Prague, Matfyzpress, pp. 233–236, 2011, ISBN 978-80-7378-185-9.

9. **D. Naydenkova**, J. Stöckel, V. Weinzettl, D. Šesták, J. Havlicek. Spectroscopic Measurements on the COMPASS Tokamak, WDS 2012 - Proceedings of Contributed Papers, Part II– Physics of Plasmas and Ionized Media (eds. J. Safrankova and J. Pavlu), Prague, Matfyzpress, pp. 222–227, 2012, ISBN 978-80-7378-225-2.

10. **D. I. Naydenkova**, V. Weinzettl, J. Stockel, P. Háček, M. Imríšek. Absolute Sensitivity Calibration of Visible Spectroscopic Diagnostic and Temporal Evolution of First Window Transmittance at the COMPASS Tokamak. WDS 2013 - Proceedings of Contributed Papers, Part II– Physics of Plasmas and Ionized Media (eds. J. Safrankova and J. Pavlu), Prague, Matfyzpress, pp. 97-103, ISBN 978-80-7378-251-1.

11. **D. Naydenkova**, J. Stöckel, V. Weinzettl. The Absolute Sensitivity Measurements of Spectra in Near IR Range at the COMPASS Tokamak. WDS 2014 - Proceedings of Contributed Papers, Part II– Physics of Plasmas and Ionized Media (eds. J. Safrankova and J. Pavlu), Prague, Matfyzpress, pp. 215-220, 2014, ISBN 978-80-7378-276-4.

12. T. Markovič, A. Melnikov, J. Seidl, L. Eliseev, J. Havlicek, A. Havránek, M. Hron, M. Imríšek, K. Kovařík, S. Medvedev, K. Mitošinková, J. Mlynar, **D. Naydenkova**, R. Pánek, J. Stockel, J. Varju, V. Weinzettl. Observations of ALfvénic-character oscillations in ohmic plasmas on the COMPASS tokamak. Proceedings of 43rd European Physical Society Conference on Plasma Physics, 40A (2016), P5.005, ISBN 2-914771-99-1.

Attachment 4. Summer schools and conferences contributions

1. IPP-International Summer University for Plasma Physics, 16-20 September, 2002, Greifswald, Germany. (During my stay in the University.)

2. 4th International Workshop and School "Towards Fusion Energy – Plasma Physics, Diagnostics, Applications." 7-13 June, 2004, Kudowa Zdroj, Poland.

   Presentation: "The discharge in hydrogen-noble gas mixture as the method to increase efficiency of conditioning of the in-vessel components of large-scale fusion devices." V.S. Voitsenya, V.N. Bondarenko, V.G. Konovalov, D.I. Naidenkova, I.V. Ryzhkov, S.I. Solodovchenko.

3. 10th International Conference and School on Plasma Physics and Controlled Fusion. 13-18 September, 2004, Alushta (Crimea), Ukraine.

   Posters:

   - "The test of film Mo mirrors under bombardment with ions of deuterium plasma." A.F. Bardamid, V.G. Konovalov, D.I. Naidenkova, A.V. Rogov, I.V. Ryzhkov, A.F. Shtan', S.I. Solodovchenko, V.S. Voitsenya, K.Yu. Vukolov, K.I. Yakimov.
   - "Investigation of the effects of sputtering and deposition on optical properties of mirrors for plasma diagnostics in a fusion reactor." A.I. Belyaeva, M. Balden, A.F. Bardamid, V.N. Bondarenko, V.G. Konovalov, D.I. Naidenkova, I.V. Ryzhkov, A.N. Shapoval, A.F. Shtan', A.A. Galuza, S.I. Solodovchenko, V.S. Voitsenya, K.I. Yakimov.
   - "Computer and experimental studies of C film deposition effect on optical properties of in-vessel metallic mirrors in fusion devices." V.N. Bondarenko, A.F. Bardamid, A.I. Belyayeva, A.A. Galuza, V.G. Konovalov, D.I. Naidenkova, A.N. Shapoval, A.F. Shtan', S.I. Solodovchenko, V.S. Voitsenya, K.I. Yakimov.
   - "Simulation of environment effects on retro-reflectors in ITER". M.V. Vinnichenko, A.F. Bardamid, A.I. Belyaeva, V.L. Berezhnyj, A.J.H. Donné, Ch. Gil, V.G. Konovalov, M. Lipa, D.I. Naidenkova, V.I. Ryzhkov, B. Schunke, S.I. Solodovchenko, A.N. Topkov, V.S. Voitsenya.

4. 5th International Workshop and Summer School " Towards Fusion Energy – Plasma Physics, Diagnostics, Spin-offs." 6-10 June, 2005, Kudowa Zdroj, Poland.

Presentation: "Behavior of mirrors fabricated from amorphous alloy under impact of deuterium plasma ions." D.I. Naidenkova, A.F. Bardamid, A.I. Belyaeva, A.A. Galuza, V.N. Bondarenko, V.G. Konovalov, I.V. Ryzhkov, A.N. Shapoval, A.F. Shtan', S.I. Solodovchenko, V.S. Voitsenya, K.I. Yakimov.

5. 7th Carolus Magnus Summer School on Plasma and Fusion Energy Physics. September 5-16, 2005, Mechelen, The Netherlands.

Poster: "On the prospect of amorphous alloys for fabrication of in-vessel mirrors for optical methods of plasma diagnostics in ITER." A.F. Bardamid, A.I. Belyaeva, V.N.Bondarenko, A.A.Galuza, O.G.Kolesnyk, V.G.Konovalov, D.I.Naidenkova, I.V.Ryzhkov, A.N.Shapoval, A.F.Shtan', S.I.Solodovchenko, V.S.Voitsenya, K.I.Yakimov.

6. 16th Annual Student Conference „Week of Doctoral Student 2007", June 5-8 2007, Prague, Czech Republic.

Presentation: "Magnetic Diagnostic Exploitation for COMPASS tokamak.", Diana Naydenkova, Olena Bilyk, Jan Stockel.

7. 23th Symposium on Plasma Physics and Technology, June 16-19 2008, Prague, Czech Republic.

Poster: "Design of New Optical System for Visible Plasma Radiation Measurements at COMPASS Tokamak", D. I. Naydenkova, V. Weinzettl, J. Stockel

8. 17th Annual Student Conference „Week of Doctoral Student 2008", June 3-6, 2008, Prague, Czech Republic.

Poster: "Design of New Optical System for Visible Plasma Radiation Measurements at COMPASS Tokamak", D. I. Naydenkova, V. Weinzettl, J. Stockel, D. Šesták, M. Aftanas.

9. 7th Kudowa Summer School Towards Fusion Energy, June 20 – 24, 2008, Kudowa-Zdrój, Poland.

Presentation: "Design of New Optical System for Visible Plasma Radiation Measurements at COMPASS Tokamak", D.I. Naydenkova, V. Weinzettl, J. Stöckel, D. Šesták, M.Aftanas

10. 18th Annual Student Conference „Week of Doctoral Student 2009", June 5-8 2007, Prague, Czech Republic.

Poster: „First Spectroscopic Measurements on the COMPASS Tokamak", D. Naydenkova, J. Stöckel, V. Weinzettl, D. Šesták, J. Havlíček

11. 8th Kudowa Summer School “Towards Fusion Energy”, September 21-25, 2009, Kudowa Zdroj, Poland.

Presentation: “Spectroscopic measurements during the first phase of the COMPASS tokamak operation”, Diana Naydenkova, Jan Stöckel, Vladimír Weinzettl, Olivier Van Hoey, Josef Havlícek, David Šesták, Filip Janky.

12. 19th Annual Student Conference „Week of Doctoral Students 2010“, June 1–4, 2010, Prague, Czech Republic.

Poster: „Progress in Multichannel Optical System for Visible Plasma Radiation Measurements at COMPASS Tokamak”, D.I. Naydenkova, V. Weinzettl, J. Stockel, D. Sestak, F. Janky, L. Sedlak.

13. 24th Symposium on Plasma Physics and Technology, June 14-17, 2010, Prague, Czech Republic.

Presentation: „Complex of the Optical Systems for Visible Plasma Radiation Measurements in the COMPASS Tokamak”, D.I. Naydenkova, V. Weinzettl, J. Stockel, D. Sestak, F. Janky, D. Jares, R. Melich, J. Vlcek.

14. 20th Annual Student Conference „Week of Doctoral Students 2011“, May 31 –June 3, 2011, Prague, Czech Republic.

Poster: “Measurements of Ion Temperature in the Edge Plasma of the COMPASS Tokamak.” D.I. Naydenkova, F. Janky, V. Weinzettl, J. Stöckel, D. Šesták, T. Odstrcil, J. Ghosh, R. Gomes, T. Pereira.

15. 21th Annual Student Conference „Week of Doctoral Students 2012“, May 29 -June 1, 2012, Prague, Czech Republic.

Poster: „Spectroscopic Measurements on the COMPASS Tokamak.“ D. Naydenkova, J. Stöckel, V. Weinzettl, D. Šesták, J. Havlicek.

16. ADAS Workshop 2012, September 23-25, 2012, Cadarache, France.

Presentation: „Review of spectroscopic diagnostic at COMPASS tokamak.“ D. Naydenkova.

17. 22th Annual Student Conference „Week of Doctoral Students 2013“, June 4-7, 2013, Prague, Czech Republic.

Poster: „Absolute Sensitivity Calibration of Visible Spectroscopic Diagnostic and Temporal Evolution of First Window Transmittance at the COMPASS Tokamak“ D. I. Naydenkova, V. Weinzettl, J. Stockel, P. Háček, M. Imríšek.

18. 23th Annual Student Conference „Week of Doctoral Students 2014“, June 4-7, 2014, Prague, Czech Republic.

Presentation: “The Absolute Sensitivity Measurements of Spectra in Near IR Range at the COMPASS Tokamak.”, D. Naydenkova, J. Stöckel, V. Weinzettl.